



**AFRL-RY-WP-TR-2023-0013**

# **WAVE-OPTICS MODELING OF HIGH-FREQUENCY (HF) PROPAGATION THROUGH THE STRUCTURED IONOSPHERE**

**Charles S. Carrano and Charles L. Rino  
Boston College**

**JUNE 2023  
Final Report**

**DISTRIBUTION STATEMENT A. Approved for public release; distribution is unlimited.**

*See additional restrictions described on inside pages*

**STINFO COPY**

**AIR FORCE RESEARCH LABORATORY  
SENSORS DIRECTORATE  
WRIGHT-PATTERSON AIR FORCE BASE, OH 45433-7320  
AIR FORCE MATERIEL COMMAND  
UNITED STATES AIR FORCE**

## NOTICE AND SIGNATURE PAGE

Using Government drawings, specifications, or other data included in this document for any purpose other than Government procurement does not in any way obligate the U.S. Government. The fact that the Government formulated or supplied the drawings, specifications, or other data does not license the holder or any other person or corporation; or convey any rights or permission to manufacture, use, or sell any patented invention that may relate to them.

This report is the result of contracted fundamental research deemed exempt from public affairs security and policy review in accordance with The Under Secretary of Defense memorandum dated 24 May 2010 and AFRL/DSO policy clarification email dated 13 January 2020. This report is available to the general public, including foreign nationals.

Copies may be obtained from the Defense Technical Information Center (DTIC)  
(<http://www.dtic.mil>).

AFRL-RY-WP-TR-2023-0013 HAS BEEN REVIEWED AND IS APPROVED FOR  
PUBLICATION IN ACCORDANCE WITH ASSIGNED DISTRIBUTION STATEMENT.

//Signature//

---

SABA MUDALIAR, Program Manager  
Multiband Multifunction RF Sensing Branch  
Multispectral Sensing & Detection Division

//Signature//

---

LAMAR A. WESTBROOK, Chief  
Multiband Multifunction RF Sensing Branch  
Multispectral Sensing & Detection Division

//Signature//

---

LEROY S. WILLEMSSEN, Chief  
Multispectral Sensing & Detection Division  
Sensors Directorate

This report is published in the interest of scientific and technical information exchange, and its publication does not constitute the Government's approval or disapproval of its ideas or findings.

\*Disseminated copies will show “//Signature//” stamped or typed above the signature blocks.

## REPORT DOCUMENTATION PAGE

PLEASE DO NOT RETURN YOUR FORM TO THE ABOVE ORGANIZATION.

<b>1. REPORT DATE</b> June 2023		<b>2. REPORT TYPE</b> Final		<b>3. DATES COVERED</b>	
				<b>START DATE</b> 15 November 2019	<b>END DATE</b> 1 December 2022
<b>4. TITLE AND SUBTITLE</b> WAVE-OPTICS MODELING OF HIGH-FREQUENCY (HF) PROPAGATION THROUGH THE STRUCTURED IONOSPHERE					
<b>5a. CONTRACT NUMBER</b> FA8650-20-C-1950		<b>5b. GRANT NUMBER</b> N/A		<b>5c. PROGRAM ELEMENT NUMBER</b> 62212F	
<b>5d. PROJECT NUMBER</b> 2030		<b>5e. TASK NUMBER</b> N/A		<b>5f. WORK UNIT NUMBER</b> Y211	
<b>6. AUTHOR(S)</b> Charles S. Carrano and Charles L. Rino					
<b>7. PERFORMING ORGANIZATION NAME(S) AND ADDRESS(ES)</b> Boston College 140 Commonwealth Ave. Chestnut Hill, MA 02467				<b>8. PERFORMING ORGANIZATION REPORT NUMBER</b>	
<b>9. SPONSORING/MONITORING AGENCY NAME(S) AND ADDRESS(ES)</b> Air Force Research Laboratory, Sensors Directorate Wright-Patterson Air Force Base, OH 45433-7320 Air Force Materiel Command, United States Air Forces			<b>10. SPONSOR/MONITOR'S ACRONYM(S)</b> AFRL/RYMF		<b>11. SPONSOR/MONITOR'S REPORT NUMBER(S)</b> AFRL-RY-WP-TR-2023-0013
<b>12. DISTRIBUTION/AVAILABILITY STATEMENT</b> DISTRIBUTION STATEMENT A. Approved for public release; distribution is unlimited.					
<b>13. SUPPLEMENTARY NOTES</b> This report is the result of contracted fundamental research deemed exempt from public affairs security and policy review in accordance with The Under Secretary of Defense memorandum dated 24 May 2010 and AFRL/DSO policy clarification email dated 13 January 2020. This report is available to the general public, including foreign nationals. Report contains color.					
<b>14. ABSTRACT</b> HF systems used for over-the-horizon-radar (OTHR), communication, signal geolocation, and space-based surveillance must contend with ionospheric structuring, which significantly alters HF propagation and can adversely affect the primary mission of these sensors. Ionospheric structuring results from a wide variety of geophysical mechanisms which manifest as sporadic-E, traveling ionospheric disturbances (TIDs), mid-latitude spread-F, equatorial plasma bubbles, auroral arcs, and polar cap patches. While the traditional approach for modeling HF sky-wave propagation is by tracing rays, ionospheric structuring causes diffraction and interference effects that are neglected in the geometric optics approximation. Diffraction and interference cause rapid fading of the HF signals which can significantly degrade system performance. In this work, we explore <i>wave-optics</i> methods in which the wave nature of radiation is properly accounted for in the modeling. In addition, wave-optics methods provide vastly improved wide-area diagnostics (enhanced situational awareness), compared with traditional ray-trace methods. For trans-ionospheric propagation at VHF and higher frequencies there is a well-developed <i>scalar</i> theory of propagation in random media. Here we develop wave-optics methods for the propagation of <i>vector</i> waves at HF wavelengths in randomly structured ionospheric media.					
<b>15. SUBJECT TERMS</b> HF propagation modeling, ionospheric impacts on HF propagation, wave-optics method, split-step Fourier method					
<b>16. SECURITY CLASSIFICATION OF:</b>			<b>17. LIMITATION OF ABSTRACT</b> SAR		<b>18. NUMBER OF PAGES</b> 74
<b>a. REPORT</b> Unclassified	<b>b. ABSTRACT</b> Unclassified	<b>c. THIS PAGE</b> Unclassified			
<b>19a. NAME OF RESPONSIBLE PERSON</b> Saba Mudaliar				<b>19b. PHONE NUMBER (Include area code)</b> N/A	

# Table of Contents

Section	Page
LIST OF FIGURES .....	ii
1.0 SUMMARY .....	1
2.0 INTRODUCTION .....	2
2.1 Propagation in Inhomogeneous Media .....	3
2.2 Induced-Source Methods .....	4
2.3 Advantages of FPE Simulation for OTHR Propagation Modeling .....	6
3.0 METHODS, ASSUMPTIONS AND PROCEDURES.....	9
3.1 Scalar Propagation Modeling with the FPE.....	9
3.2 Power-flow Trajectories.....	11
3.3 Vector Propagation modeling – Brent’s Method .....	13
3.4 Vector Propagation Modeling – the VFPE .....	17
3.5 Comparing Brent’s Algorithm with the VFPE .....	22
3.6 Boundary Conditions for the Earth Surface.....	23
4.0 RESULTS AND DISCUSSION .....	27
4.1 Propagation of Vector Waves through Traveling Ionospheric Disturbances .....	27
4.2 Propagation of Vector Waves through Developing Spread-F .....	35
4.3 VFPE and Ray Theory .....	40
4.4 Locally Homogeneous Wavefield Extrapolation.....	46
4.5 Corrected FPE vs Locally Homogeneous Wavefield Extrapolation.....	52
5.0 CONCLUSIONS.....	55
6.0 REFERENCES .....	64
APPENDIX A – Publications and Presentations .....	66
LIST OF SYMBOLS, ABBREVIATIONS AND ACRONYMS .....	67

# LIST OF FIGURES

Figure	Page
Figure 1. Plasma frequency (left), HF power (dB) (middle) and arrival angle (right) from wave-optics simulation of a 20 MHz wave propagating through a developing ionospheric disturbance	7
Figure 2. Wave-optics simulation of a 20 MHz wave propagating through a quasi-parabolic ionosphere; the left plot shows HF power (dB), right plot shows arrival angle spectrum	10
Figure 3. Same as Figure 2 but using the method staircase method to impose reflection at the earth surface	10
Figure 4. Magnitude of the time-averaged Poynting flux (colors) and power-flow trajectories (white curves)	12
Figure 5. HF power (dB) (left) and arrival angle spectrum (right) for wave-optics simulation of a 20 MHz wave propagating through a quasi-parabolic ionosphere including magnetic field effects	14
Figure 6. Azimuthal (left) and cross-range (right) components of the electric field for the same simulation as in Figure 5	14
Figure 7. Rays for the ordinary (O) and extraordinary (X) modes using the magneto-ionic ray tracer PHaRLAP (left), arrival angle for the O and X rays determined via ray-tracing	15
Figure 8. Simulation of longitudinal propagation for a linearly polarized wave (along z) using the Brent et al. algorithm	16
Figure 9. Faraday rotation rate for the simulation shown in Figure 4 (black line), analytic rotation rate for the Brent et al. algorithm (green dashed line), and exact result for longitudinal propagation	17
Figure 10. Propagation of a 20 MHz signal propagating through a quasi-parabolic ionosphere simulated using Brent's method (left) and the vector FPE (right)	23
Figure 11. VFPE simulation of multi-hop propagation over a flat perfectly conducting surface	24
Figure 12. Reflection of a thin beam from a perfectly conducting planar boundary	25
Figure 13. Reflection of a thin beam from a perfectly conducting curved boundary	25
Figure 14. Vector FPE simulation with no ground and no magnetic field	29
Figure 15. Vector FPE simulation with ground but no magnetic field	30
Figure 16. Vector FPE simulation with ground but no magnetic field	30
Figure 17. Vector FPE simulation with ground and magnetic field	31
Figure 18. TID simulation at t=0 sec	32
Figure 19. TID simulation at t=300 sec (1/6 cycle)	32
Figure 20. TID simulation at t=600 sec (2/6 cycle)	33
Figure 21. TID simulation at t=900 sec (3/6 cycle)	33
Figure 22. TID simulation at t=1200 sec (4/6 cycle)	34
Figure 23. TID simulation at t=1500 sec (5/6 cycle)	34
Figure 24. Electron density field containing EPBs generated by Yokoyama (2017)	36
Figure 25. Plasma frequency used in our vector FPE simulations	37
Figure 26. Total HF intensity from the vector FPE simulation	38
Figure 27. Left-hand circularly polarized power from the vector FPE simulation	38
Figure 28. Right-hand circularly polarized power from the vector FPE simulation	39
Figure 29. Close-up of the region where HF waves interact with the equatorial plasma bubbles	39

Figure 30. Upper frame shows the dB intensity of the elliptically polarized beam response identified as the O mode, lower frame is the corresponding spectral intensity normalized to the wave vector magnitude in dB units..... 41

Figure 31. Upper frame is the dB intensity opposite elliptically polarized beam response identified as the X mode, lower frame is the corresponding spectral intensity normalized to the wave vector magnitude in dB units..... 42

Figure 32. Upper frame shows the O mode (red) and X mode (blue) peaks, lower frame shows the corresponding spectral-domain peaks plotted against propagation direction ..... 42

Figure 33. Upper frame compares the O-mode trace shown in the upper frame of Figure 32 (red) with the O-mode trace predicted by the PHaRLAP code (blue), lower frame shows the same comparison for the X-mode trace and the PHaRLAP code prediction..... 43

Figure 34. Recalculation of VFPE result shown in Figure 33 with VFPE correction..... 43

Figure 35. Relative error in the structure interaction approximation as a function of  $\kappa/k$ ..... 45

Figure 36. Plasma frequency for a Chapman ionosphere (peak = 9 MHz) and geometric optics (ray-trace) solution for an HF beam (15 MHz) reflecting from the ionosphere ..... 48

Figure 37. Plasma frequency for a Chapman ionosphere (peak = 9 MHz) and geometric optics (ray-trace) solution for an HF beam (15 MHz) reflecting from the ionosphere ..... 50

Figure 38. Adequately sampled FPE solution (colors) and geometric optics (white) ..... 50

Figure 39. Coarsely sampled FPE solution (colors) and geometric optics (white) ..... 51

Figure 40. Coarsely sampled solution using Fishman’s algorithm and geometric optics (white) 51

Figure 41. Propagation of a narrow beam at 12 MHz predicted by the uncorrected FPE method 52

Figure 42. Propagation of a narrow beam at 12 MHz predicted by the corrected FPE method ... 53

Figure 43. Propagation of a narrow beam at 12 MHz predicted by the locally homogeneous wavefield extrapolation method..... 54

## 1.0 SUMMARY

This is the final report for the project entitled Wave-Optics Modeling of High-Frequency Propagation through the Structured Ionosphere (contract FA8650-20-C-1950) during which Boston College (BC) developed full-wave algorithms to model the propagation of HF waves in a structured ionosphere.

HF systems used for over-the-horizon-radar (OTHR), communication, signal geolocation, and space-based surveillance must contend with ionospheric structuring, which significantly alters HF propagation and can adversely affect the primary mission of these sensors. Ionospheric structuring results from a wide variety of geophysical mechanisms at low-, mid-, and high-latitudes which manifest as sporadic-E, traveling ionospheric disturbances (TIDs), mid-latitude spread-F, equatorial plasma bubbles, auroral arcs, and polar cap patches.

The traditional approach for modeling HF sky-wave propagation is by tracing rays through the ionosphere in the geometric optics approximation. While ray-tracing provides an accurate description of propagation conditions when the ionosphere is smooth (quiescent conditions), ray-tracing is inadequate when ionospheric structure is present because diffraction and interference effects are neglected in the geometric optics approximation. Diffraction and interference cause rapid fading of the HF signals, which can play an important role in many radio propagation scenarios. To remedy this shortcoming, we explore *wave-optics* methods in which the wave nature of radiation is properly accounted for in the modeling. In addition to including diffraction and interference effects, wave-optics methods provide vastly improved wide-area diagnostics for the propagation environment (enhanced situational awareness), compared with traditional ray-trace methods. For trans-ionospheric propagation at VHF and higher frequencies there is a well-developed scalar theory of propagation in random media. Our objective was to develop a wave-optics method for the propagation of vector waves (which is necessary for modern polarization-aware systems) at HF wavelengths in randomly structured media.

In the process of validating the wave-optics approach we discovered a disparity between wave-optics beam propagation and ray-optics prediction of the peak intensity trajectory. Considerable effort was expended to understand the error. We uncovered a previously unknown fundamental limitation in the wave-optics approach when applied to HF propagation problems. In the final stages of the project, we explored wide-angle algorithms which offer the promise of obtaining highly accurate and efficient propagation modeling results including polarization effects when random ionospheric structure is present. Some of this later work was left only partially completed, unfortunately, because the project was not fully funded.

## 2.0 INTRODUCTION

HF systems used for communication, signal geolocation, over-the-horizon-radar (OTHR), and space-based surveillance must contend with ionospheric structuring. This structuring alters HF propagation conditions and may adversely affect their primary mission. Ionospheric structuring results from a wide variety of geophysical mechanisms and plasma instabilities operating at low-, mid-, and high-latitudes which manifest as sporadic-E, traveling ionospheric disturbances (TIDs), mid-latitude spread-F, equatorial plasma bubbles, auroral arcs, and polar cap patches. Current techniques for modeling HF propagation in the presence of ionospheric structure are deficient in several respects, as discussed by Carrano et al. (2020).

The traditional approach for modeling HF sky-wave propagation is by tracing rays. Ray-trace methods are derived from the WKB solution (geometric optics) for propagation through weakly inhomogeneous media. The WKB solution neglects diffraction effects and therefore ray-trace results degrade when the refractive index changes on scales comparable to the radius of the 1st Fresnel zone or smaller. Diffraction causes fluctuations in HF power, delay, Doppler, and arrival angle, which are crucial to include in system impact analyses but are not assessible using ray-trace methods. To remedy this shortcoming, we explore *wave-optics* methods in which the wave nature of radiation is properly accounted for in the modeling. Wave-optics deals with the study of physical phenomena including polarization, diffraction, and interference that lie outside the ray approximation of geometric optics. The term full-wave refers to methods which solve the complete set of Maxwell's equations with minimal simplifying assumptions. In this report, we will use the terms 'wave-optics' and 'full-wave' interchangeably.

While a full treatment of Maxwell's equations is possible via the finite-difference time domain (FDTD) method, at least in principle, the computational requirements for solving large-scale HF propagation problems this way remain prohibitively expensive. One-wave forward-marching methods, such as parabolic wave equation (PWE) methods, can provide full-wave solutions much more efficiently for large-scale problems. PWE models have been widely used to address small-scale refractive index structure along tropospheric radio propagation paths (Dockery, 1998), but so far there have been relatively few applications of PWE methods to HF propagation in the ionosphere (Wagen and Yeh, 1989; Hocke and Igarashi, 2003). The main reason for this is that modeling ionospheric birefringence requires the solution of a vector problem. The theory of full-wave methods for vector problems is more complex and less well-understood than for scalar problems. Accommodating birefringence is necessary for modeling propagation effects on modern polarization-aware HF systems. In this project, we develop a vector forward propagation equation (VFPE) method for addressing the vector propagation problem. Another, albeit less significant, reason that full-wave methods have not been widely used for ionospheric problems is that they provide intensity, phase, and arrival angle diagnostics but do not directly provide path-integrated quantities which HF operators require such as delay and Doppler. Chaudhury and Chaturvedi (2006) explain how power-flow trajectories may be traced through full-wave solutions to general electromagnetic problems. We leverage this idea to compute path integrated quantities through full wave-solutions for HF propagation in the ionosphere.

There are many theoretical approaches to characterizing propagation in transparent media with reflecting boundaries. EM fields depend on space, time, and frequency. However, for the class of

problems of interest it is convenient to use the time-harmonic form of Maxwell's equations, effectively eliminating the explicit time dependence, while constraining the type of media considered. The interaction of EM waves with the earth's ionosphere is characterized by a frequency-dependent tensor, which reduces to a diagonal form when the background magnetic field dependence is negligible, which is generally the case at frequencies much higher than HF.

From Maxwell's equations a vector or scalar wave equation is constructed, which is linear but inhomogeneous, except for the case of an idealized uniform background (e. g. free space). There are two-approaches to constructing solutions. In random media, small local perturbations act as induced sources. However, unlike discrete scatterers, the effect of locally small interactions is a phase perturbation. While it is recognized that this approach is limited to weak local interactions, the multiple phase screen theory suggests that large phase perturbations can be accommodated. While this is true, we found that phase gradients that are accommodated in geometrical optics, are not properly accommodated in wave-optics. The second approach incorporates the structure in the wave equation as position-dependent differential operators. The standard parabolic wave equation (PWE) is the most familiar manifestation of this approach. However, in its simplest form it is restricted to small refractive propagation angles. In general, scattering angles at HF are significantly larger than the standard parabolic wave equation method can support.

Constructing a full-wave diffraction theory that characterizes propagation in a highly refracting structured background is exceptionally demanding, while accurate and efficient ray-tracing algorithms have been available for decades. Two widely used diffraction algorithms incorporate computationally efficient split-step alternation between spatial Fourier domain propagation and a spatial-domain phase correction. The standard parabolic wave equation uses the narrow-angle form of the propagation operator (Levy, 2000, Eq. (3.30)). The forward propagation equation (FPE) as defined in our first publication related to this project (Rino and Carrano, 2021a, Eq. (40)) uses an unrestricted propagation operator. This plus a companion paper (Rino and Carrano, 2021b), developed and demonstrated an FPE for vector fields. However, a disparity was observed when FPE calculations of HF refraction by a Chapman layer were compared with ray-trace calculations (See Figures 6 and 7 in (Rino and Carrano, 2021b)). We will discuss the disparity, its ramifications, and several approaches to remedy the problem, throughout this report.

In retrospect, the disparity might have been expected. The standard PWE is constrained intrinsically to a narrow range of propagation angles. A hierarchy of parabolic differential equation implementations, notationally (PDEs), have been constructed to accommodate the larger range of propagation angles needed to support refraction. Although the unrestricted FPE propagation operator accommodates a full range of propagation angles, the extended range of propagation angles is not supported by the FPE.

## 2.1 Propagation in Inhomogeneous Media

The essential elements of the theory of propagation in transparent inhomogeneous media are captured by the two-dimensional scalar wave equation

$$\nabla^2\psi(x, y) + k^2n^2(x, y)\psi(x, y) = 0 \quad (1.1)$$

where  $\psi(x;y)$  is the complex field and

$$n^2(x, y) = 1 - X(x, y). \quad (1.2)$$

For the earth's ionosphere,  $X = (\omega_p/\omega)^2$ . The plasma frequency,  $\omega_p$ , is proportional to the electron density. Angular frequency is  $\omega = 2\pi f$  and free-space wavenumber is  $k = 2\pi f/c$ , where  $f$  is frequency and  $c$  is the vacuum velocity of light.

The  $x$  axis is identified as the propagation reference direction (positive forward, negative backward). The  $y$  spatial Fourier decomposition of the field is defined as

$$\psi(x, y) = \int \hat{\psi}(x; \kappa) \exp(i\kappa y) \frac{d\kappa}{2\pi} \quad (1.3)$$

Evaluation of the Fourier transformation of (1.1) for constant  $n$  shows that

$$(n^2 - (\kappa/k)^2) \hat{\psi}(x; \kappa) = 0, \quad (1.4)$$

which establishes a relation between the transverse spatial wavenumber,  $\kappa$ , and the horizontal wavenumber

$$k_x(\kappa) = k \sqrt{n^2 - (\kappa/k)^2}. \quad (1.5)$$

The Fourier domain operation

$$\theta_{\Delta x} \psi(x, y) = \int \hat{\psi}(x; \kappa) \exp[ik_x(\kappa)\Delta x] \exp(i\kappa y) \frac{d\kappa}{2\pi}, \quad (1.6)$$

advances the field from  $x$  to  $x + \Delta x$ . Forward marching algorithms are effectively generalizations of the propagation operation,  $\theta_{\Delta x} \psi(x, y)$ .

## 2.2 Induced-Source Methods

The development of the theory of propagation in random media generally proceeds via rearrangement of (1.1) and (1.2) so that the refractive index perturbation,  $X$ , appears as an induced source:

$$\begin{aligned} \nabla^2 \psi + k^2(1 - X)\psi &= 0 \\ \nabla^2 \psi + k^2\psi &= k^2 X\psi \end{aligned} \quad (1.7)$$

In two spatial dimensions, the solution to the second equation may be expressed in integral form

$$\psi(x, y) = \psi_0(x, y) + k^2 \iint \psi(x', y') X(x', y') \left[ iH_0^1(k\sqrt{(x-x')^2 + (y-y')^2}) / 4 \right] dx' dy', \quad (1.8)$$

using the free-space Green's function appearing in the brackets above. The field  $\psi_0(x, y)$  is a solution to the free-space wave equation. Referring to the  $\psi(x', y') X(x', y')$  terms in (1.8) as induced sources comes from boundary-integral equation theory which identifies induced sources on discontinuous boundaries explicitly. The development in (Rino and Carrano, 2021a) was an attempt to use continuous boundary integrals to construct a forward marching solution. The development starts with the  $y$  Fourier transformation of (1.8).

$$\hat{\psi}(\kappa; x) = \hat{\psi}_0(\kappa; x) - i \frac{k}{2} \int_0^\infty S(\kappa; x') \frac{\exp[ikg(\kappa) |x - x'|]}{g(\kappa)} dx', \quad (1.9)$$

where  $S(\kappa; x)$  is the  $y$  Fourier transform of the product  $\psi(x, y) X(x, y)$  and  $g(\kappa)$  is given by

$$g(\kappa) = k\sqrt{1 - (\kappa/k)^2}. \quad (1.10)$$

Forward and backward propagating waves are identified by the location of their induced sources relative to the point of observation. It follows that

$$\hat{\psi}^+(\kappa; x) = \hat{\psi}_0(\kappa; x) - i \frac{k}{2} \int_0^x S(\kappa; x') \frac{\exp[ikg(\kappa) |x - x'|]}{g(\kappa)} dx' \quad (1.11)$$

$$\hat{\psi}^-(\kappa; x) = -i \frac{k}{2} \int_x^\infty S(\kappa; x') \frac{\exp[ikg(\kappa) |x - x'|]}{g(\kappa)} dx', \quad (1.12)$$

where

$$\hat{\psi}(\kappa; x) = \hat{\psi}^+(\kappa; x) + \hat{\psi}^-(\kappa; x). \quad (1.13)$$

In the subsequent development it was *assumed* that an additive separation of free-propagation and media-interaction contributions could be maintained and that the known field at  $x$  could be identified as an initiating source. With these assumptions the spatial Fourier domain relation

$$\hat{\psi}(\kappa; x + \Delta x) = \hat{\psi}(\kappa; x) \exp[ikg(\kappa)\Delta x] - \frac{ik}{2g(\kappa)} \int_x^{x+\Delta x} S(\kappa; x') dx'. \quad (1.14)$$

would advance the field a small increment forward. Transforming the equation back to the spatial domain and using the approximation

$$\int \frac{ik}{2g(\kappa)} \int_0^{\Delta x} S(\kappa; x') dx' \exp(iky) \frac{dk}{2\pi} \approx i \frac{k}{2} \psi(x, y) X(x, y) \Delta x, \quad (1.15)$$

produces the forward propagation equation (FPE), which forms the basis for our propagation modeling work:

$$\frac{d\psi(x, y)}{dx} = \theta_{\Delta x}\psi(x, y) + i\frac{k}{2}\Delta X(x, y)\psi(x, y). \quad (1.16)$$

We solve (1.16) numerically using the split-step method, which gives

$$\psi(x + \Delta x, y) = \theta_{\Delta x}\psi(x, y) \exp\left\{i\frac{k}{2}X(x, y)\Delta x\right\}. \quad (1.17)$$

The critical difference between the standard parabolic equation (PWE) and the FPE is the replacement of the narrow-angle propagation operator with an unrestricted propagation operator. Although the development suggests a generalization of the PWE, a consistent development of the theory will show that wave equation supports separate propagation and media interaction contributions only under narrow-angle scatter conditions. Moreover, generating a discrete sampling of (1.16) and following the same procedure that was used in (Rino and Carrano, 2021b) to calculate induced sources that support surface reflections leads to the same narrow-angle-scatter constraint. Ultimately, we learned that a consistent solution to the inhomogeneous wave equation cannot separate propagation and media interaction as additive contributions.

### 2.3 Advantages of FPE Simulation for OTHR Propagation Modeling

Forward propagation equation (FPE) modeling is a full-wave technique that marches the solution forward in space from one plane to the next. At each stage of the calculation, the electric field along each plane is expressed in terms of the angular spectrum of plane waves intersecting that plane. From the angular spectrum, it is straightforward to determine the amplitude and direction of all radio propagation modes anywhere in the computational domain. A windowing function is applied to the field surrounding a region of interest to improve localization in space and to suppress side-lobes. From this result, we can produce angle-of-arrival “maps,” which depict the spectrum of angle-of-arrival (AOA) at all locations on the ground (or in the air). These AOA maps identify all radio propagation modes reaching the target along with their individual amplitudes. These maps represent an advantage of full-wave simulation over ray-tracing in that there is no need to specifically ‘home’ rays to identify the propagation modes connecting the transmitter and target.

Figure 1, adapted from (Carrano et al., 2020) demonstrates the advantages of FPE full-wave modeling vs traditional ray-tracing for HF propagation problems. The plots in the top and bottom rows correspond to a different times (UT) in the development of traveling ionospheric disturbances (TID), an ionospheric phenomenon known to limit the performance of OTHR systems. The first plot in each row shows color contours of electron density from a physics-based ionosphere model (see Carrano et al., 2020 for full details), depicted in terms of plasma frequency. The second plot in each row shows color contours of HF signal intensity, obtained from the full-wave calculation. Superimposed on the intensity plots are white rays that have been explicitly traced from the transmitter using the ray-trace method of Coleman (1998). The third plot in each row shows color contours of the arrival angle spectrum. These angle of arrival ‘maps’ show the locus of all

directions from which incident waves are arriving and reflected waves are departing at each location on the ground. The arrival angle is depicted here as a function of local elevation angle while facing toward the receiver, such that incident rays have positive elevation angles and reflected rays have negative elevation angles. The arrival angle data are colored by spectral power, which indicates the magnitude of the contribution to the total received power from waves travelling in each direction. For all color contours, the color scale is relative with red indicating the highest values and blue indicating the lowest. White dots shown on the maps indicate the footprints on the ground for each traced ray that returns to the surface (not all launched rays return to Earth). The direction of the departing (reflecting) rays are also shown, to facilitate comparison with the wave-optics result.

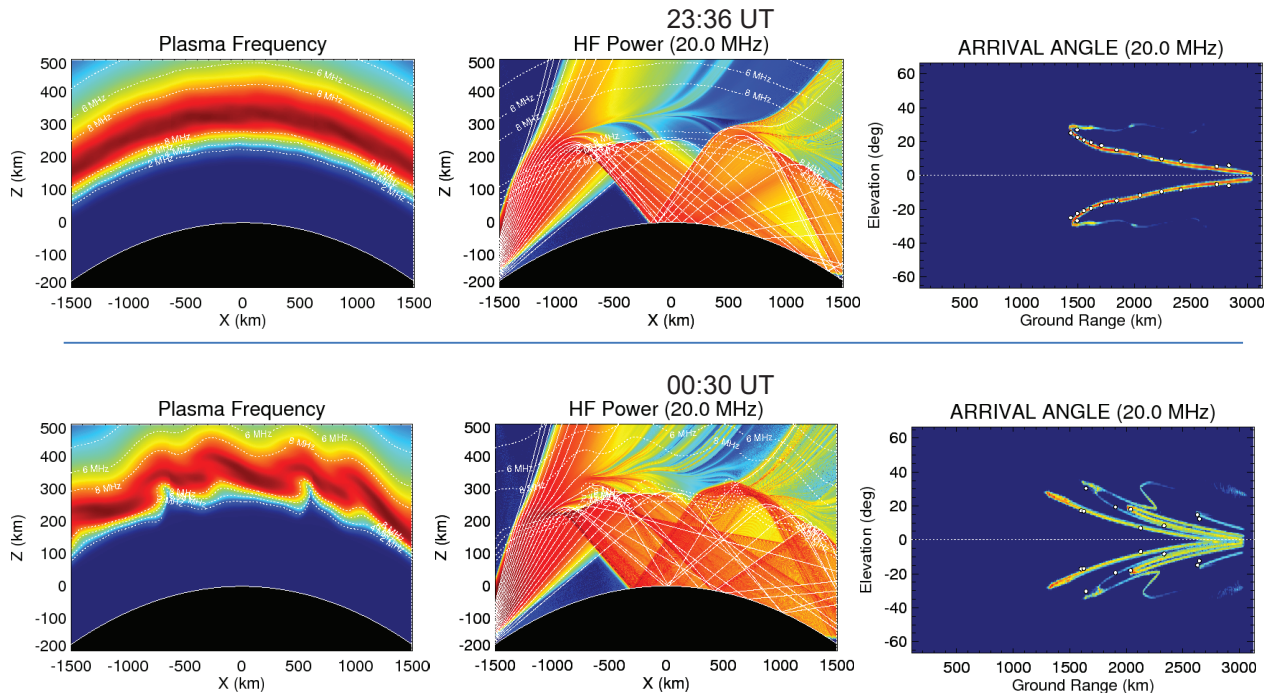


Figure 1. Plasma frequency (left), HF power (dB) (middle) and arrival angle (right) from wave-optics simulation of a 20 MHz wave propagating through a developing ionospheric disturbance

At the first time shown (24 minutes before midnight), the ionosphere is mostly quiescent with only a nascent signature of TIDs developing in response to forcing by neutral winds. The wave-optics and ray-tracing calculations both predict single-mode propagation to ranges past 2000 km, while the wave-optics calculations also reveal a region of two-mode propagation (high and low ray reflections from the F region) at shorter ranges.

At the second time shown (30 minutes past midnight), the TIDs are well-developed and exhibit a significant downward tilt in the zonal direction. Propagation at all ranges is now multi-modal, with at least four distinct modes of propagation present at ranges between 2000–2400 km. Only the full-wave solution clearly reveals the structure of all propagation modes present. The footprints of the ray-tracing results tend to lie on one of the propagation modes indicated by the wave-optics solution. Without the wave-optics result for comparison, these ray-tracing footprints would appear randomly distributed and difficult to interpret. Also note that the plumes of depleted plasma begin

to act as conduits for HF power to penetrate through the F-region and leak out into space. As a result of this power leakage less power is available to illuminate targets on the ground, thereby reducing the efficiency of the radar.

Despite the advantages of full-wave modeling, many quantities of interest to a radar operator, including group range and phase advance, require integration along specific propagation paths through the medium that connects two points. Such path integrated quantities are not provided directly by full-wave simulation, as they are with ray-tracing. Instead, they must be computed *post-facto* from the full-wave solution. From the intensity of the electric field and the direction of travel we can compute the time-averaged Poynting flux vector. Trajectories of power-flow may be found by tracing along the Poynting vector (Chaudhury and Chaturvedi, 2005), in exactly the same way a magnetic field line tracer traces along the geomagnetic field. Later in this report, we show examples tracing the time-averaged Poynting vector field to obtain power flow trajectories at angles where the angle of arrival spectrum has appreciable power (i.e. for each propagation mode that the radar is likely to detect).

## 3.0 METHODS, ASSUMPTIONS AND PROCEDURES

### 3.1 Scalar Propagation Modeling with the FPE

The spectrum of angle of arrival angle obtained by wave-optics simulation may be used to quickly and robustly identify all sky-wave propagation modes that reach the target along with their individual amplitudes. Traditionally, these propagation modes are determined by tracing rays, by searching for rays that connect transmitter and receiver. This search is generally referred to as ‘homing’ rays. The relevance to OTHR applications is that understanding how the target is illuminated is a crucial step toward modeling how energy will be reflected back to the radar for target detection and characterization.

One of our initial tasks was to test our claim that the spectrum of arrival angle provided by wave-optics correctly identifies all sky-wave propagation modes that reach a given location on the ground. Our methodology was to launch sky-wave rays from this location in the directions (arrival angles) of each propagation mode identified by wave-optics, and demonstrate that these rays indeed lead back to the transmitter. Initially, we attempted this for one of the scenarios described in Carrano et al., (2020) corresponding to highly disturbed ionospheric conditions that support many complex propagation modes. Unfortunately, we found that such traced rays did not always lead back to the receiver as we anticipated. At the time, we believed the reason for this discrepancy might be a bug in our software. We took a number of steps to understand the problem.

First, we considered a scenario corresponding to less disturbed ionospheric conditions, thinking that perhaps we would find agreement under less complex propagation conditions. When the discrepancy persisted for the less disturbed ionospheric scenario, we decided to consider a model ionospheric scenario where the propagation calculations can be solved analytically. Croft and Hoogasian (1968) presented an analytic solution for a sky-wave reflected from a single quasi-parabolic layer, and we used this to validate our codes. From this exercise, we learned that our ray tracing algorithm is consistent with the exact solution while our wave-optics algorithm was not entirely so.

The plots shown in Figure 2 show the results of wave-optics simulation for a 20 MHz wave propagating through a quasi-parabolic ionosphere. The left plot shows HF power in dB, while the right plot shows the arrival angle spectrum in dB. The latter indicates the direction of downward and upward moving waves at the ground as a function of local elevation angle. Color scales are relative with red indicating high values and blue indicating low values. As shown in the Figure, we obtain reasonable agreement between the wave-optics predictions, ray-trace predictions (superimposed white curves), and exact results for a quasi-periodic ionosphere (shown as red dashed curves in the arrival angle plot).

However, we noted that our wave-optics code placed the second ground hop at a somewhat farther range than the exact solution (or the predictions from the ray-tracing code). Since the range to the first hop was correct but the range to the second was slightly too far, we decided to investigate our implementation of the boundary condition at the earth surface. For these calculations we used the approach by Hocke and Igarashi (2003), which implements the reflecting boundary condition at the earth surface by imposing an empirical refractive index profile beneath the earth surface. Our

presumption was that the range to the second hop was too far because the wave penetrated the earth surface several km before the wave was turned (thereby accumulating excess range). We were able to minimize this excess range by altering the profile to make the reflection occur closer to the surface. As we shall discuss later, however, this extra range was found to be inherent to the FPE approximation itself. Hence our early attempts to ‘compensate’ for this effect via modification of the boundary conditions, while effective, were also artificial.

We also implemented a different earth reflection boundary, using a staircase approximation to earth curvature, as described in Levy (2000). In this approach, a sine transform was used to prevent any penetration through the earth surface. The results using the Rino and Kruger boundary condition are shown in Figure 3 for comparison. Clearly shown in the arrival angle plot are spurious upward traveling waves at ranges past that of the skip zone. We believe these are due to knife-edge diffraction from discrete changes in the height of the earth surface from one screen to the next. In a later section, we discuss how to replace the staircase approximation with a shift-map approach that leads to better results (Rino and Kruger, 2001). The Rino and Kruger (2001) approach can support a general impedance boundary condition which is necessary to accurately model reflection from land, sea, and littoral regions.

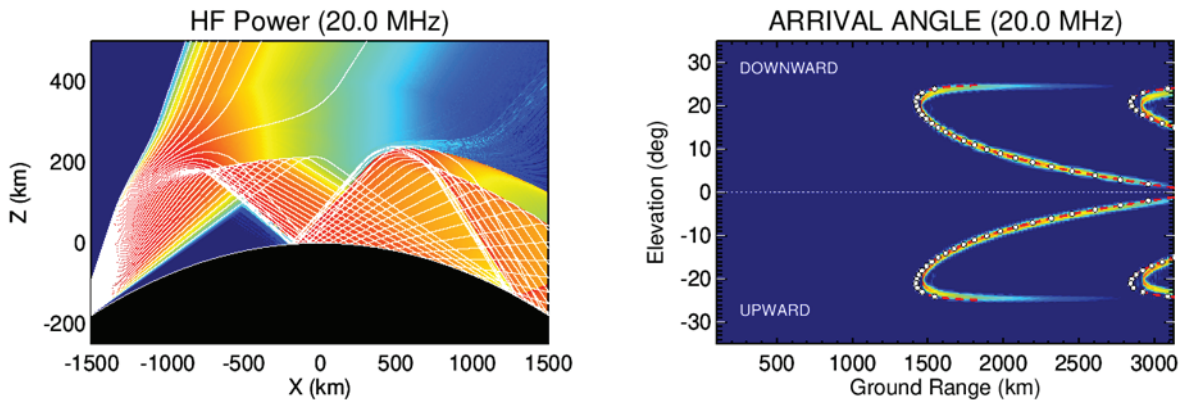


Figure 2. Wave-optics simulation of a 20 MHz wave propagating through a quasi-parabolic ionosphere; the left plot shows HF power (dB), right plot shows arrival angle spectrum

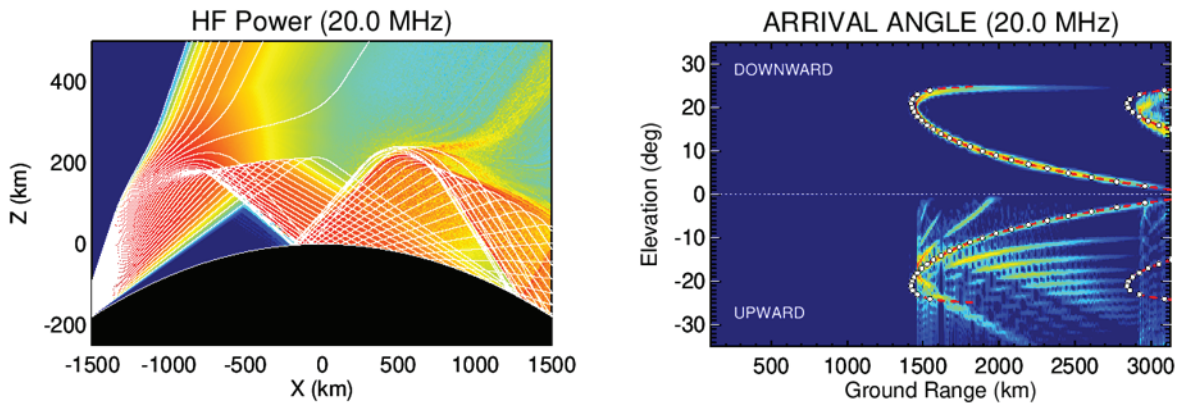


Figure 3. Same as Figure 2 but using the method staircase method to impose reflection at the earth surface

Once we verified that we had a working, partially validated, wave-optics code we explored techniques to compute path-integrated quantities from the wave-optics solution.

### 3.2 Power-flow Trajectories

Our aim is to trace power-flow trajectories through the wave-optics solution as a precursor to computing path integrated quantities such as range delay and phase advance. As explained by Chaudhury and Chaturvedi (2005), power-flow trajectories satisfy the following coupled differential equations, which we express in terms of the 2D coordinate system  $(x, z)$  employed by our wave-optics algorithm:

$$\frac{dx}{ds} = \frac{p_x}{|\mathbf{p}|}, \quad \frac{dz}{ds} = \frac{p_z}{|\mathbf{p}|} \quad (1.18)$$

where  $\mathbf{p}$  is the time-averaged Poynting flux and  $ds$  is a differential path element. For a plane wave traveling in an cold unmagnetized plasma, the Poynting flux is related to the electric field  $\mathbf{E}$  as

$$\langle \mathbf{p} \rangle = \frac{1}{2} \frac{|\mathbf{E}|^2}{\eta_0} n \hat{\mathbf{n}} \quad (1.19)$$

where  $n$  is the refractive index,  $\eta_0$  is the impedance of free-space, and  $\hat{\mathbf{n}}$  is a unit vector in the direction of the wavefront normal. The complex amplitude of the field  $u(z; x)$  is used to represent the slowly varying part of the electric field (any spatial component) with the temporal dependence removed. Along a phase screen located at  $x$ , the complex amplitude may be represented as a superposition of plane waves traveling in different directions:

$$u(z_j; x) = \frac{1}{N} \sum_{k=0}^{N-1} \hat{u} \left( \frac{2\pi k}{N\Delta z}; x \right) \exp \left( i \frac{2\pi j k}{N} \right) = \frac{1}{N} \sum_{k=0}^{N-1} \hat{u} \left( \frac{2\pi k}{N\Delta z}; x \right) \exp \left( i \frac{2\pi}{\lambda} z_j \sin \theta_k \right), \quad (1.20)$$

where  $\sin(\theta_k) = 2\pi k/N\Delta z$  is the propagation direction of the  $k^{\text{th}}$  plane wave. The time-averaged Poynting flux for the  $k^{\text{th}}$  plane wave is then

$$\langle \mathbf{p}_k(x) \rangle = \frac{n}{2\eta_0} \left| \hat{u} \left( \frac{2\pi k}{N\Delta z}; x \right) \right|^2 (\cos \theta_k, \sin \theta_k). \quad (1.21)$$

Equation (1.21) defines a single time-averaged Poynting flux for each phase screen (since it depends only on the screen location  $x$ ). To estimate the *local* Poynting flux at each grid location  $z_j$  along the phase screen, we compute the FFT implied by (1.20) using a sliding Hamming window centered at  $z_j$ , and then we sum over all plane waves  $k$ . We then trace power-flow trajectories by solving the differential equations in equation (1.18). Figure 4 shows the result. The colors indicate the magnitude of the time-averaged Poynting flux, while the white curves depict power-flow

trajectories. The left plot show arrows proportional to the magnitude and direction of the time-averaged Poynting vector, while the right plot shows arrows proportional to only the direction of the Poynting vector.

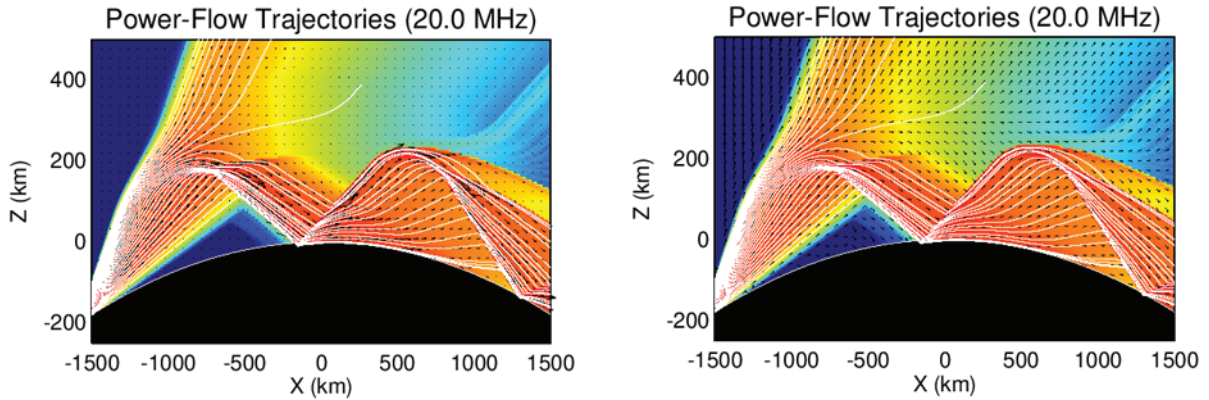


Figure 4. Magnitude of the time-averaged Poynting flux (colors) and power-flow trajectories (white curves)

These power-flow trajectories may be compared with rays traced using the theory of geometric optics (e.g. the white curves in Figures 2 and 3), which satisfy

$$\frac{d}{ds} \left( n(x, z) \frac{dx}{ds} \right) = \frac{dn}{dx}, \quad \frac{d}{ds} \left( n(x, z) \frac{dz}{ds} \right) = \frac{dn}{dz}. \quad (1.22)$$

Rays describe orthogonal trajectories to the geometrical wavefronts  $S(\mathbf{r})=\text{constant}$ , where  $S(\mathbf{r})$  is the so-called eikonal function which is proportional to phase. Average power flows in the direction of  $\nabla S(\mathbf{r})$ . Equation (1.22) follows if the magnitude of  $\nabla S(\mathbf{r})$  equals the magnitude of  $n$ , which is a fundamental assumption of geometric optics. Comparing ray-paths in Figures 2 and 3 with the power-flow trajectories in Figure 4, we see that they are roughly equivalent in regions of space characterized by waves traveling in a single dominant direction. In other regions, for example, following the skip zone where downward traveling waves and upward traveling reflected waves are both present, the rays of geometric optics cross each other while power-flow trajectories do not. This is a consequence of summing the contributions to the Poynting flux from each plane wave incoherently. These calculations were performed while neglecting the geomagnetic field, in which case the medium is isotropic. In general, the wave normal direction is orthogonal to the wave front passing through that point, whereas the ray direction is the direction of energy flow at that point. These two directions need not be the same when magnetic field effects are included, since the medium is then anisotropic.

### 3.3 Vector Propagation modeling – Brent’s Method

We discussed how we model the propagation of energy through wave-optics simulations. We also mentioned efforts to extend our wave-optics modeling capabilities to propagation in a magnetized plasma, which is an anisotropic birefringent medium. Until recently, it was our understanding that this had not been attempted previously. During a review of the literature, however, we found a paper by Brent et al. (1990) which presented a technique for modeling propagation through an anisotropic medium in the parabolic approximation. We implemented the algorithm by Brent et al. (1990) for propagation through a magnetized ionosphere, and we applied it to our problem of modeling the operation of an OTHR in sky-wave mode.

We begin by reviewing the essential elements of the Brent et al. (1990) algorithm, and then we discuss its application to our problem. These authors solve the wave equation in a cylindrical coordinate system  $(E_r, E_\theta, E_z)$ , with  $E_r$  as the range direction. Assuming that power flow is principally along the range direction, the parabolic approximation is invoked to replace the second-order wave equation with a simpler set of coupled first order differential equations. These equations are solved using the split-step technique, which advances the solution through a sequence of phase screens oriented in the  $z$ -direction using three stages. First, the field is advanced in range to the next screen as if the medium were homogeneous. Second, the interaction of the wave with the medium is accounted for by imparting a phase change to the wave along the screen. Third, magnetic coupling is accounted for by rotating the field by an amount that depends upon the external magnetic field magnitude and direction. These three stages are performed mathematically as follows to march the field from screen  $n$  to screen  $n+1$ :

$$\begin{aligned} \begin{bmatrix} E_\theta \\ E_z \end{bmatrix}^{n+1} &= M(\Delta r; z) \cdot \exp \left[ -i \left( \frac{kX(z)}{2U} \Delta r \right) \right] \cdot F^{-1} \left\{ \exp \left[ -i \frac{s^2 \Delta r}{2k} \right] F \begin{bmatrix} E_\theta \\ E_z \end{bmatrix}^n \right\} \\ &\quad \text{(stage 3)} \qquad \qquad \text{(stage 2)} \qquad \qquad \text{(stage 1)} \end{aligned} \quad (1.23)$$

In the above,  $F$  indicates a Fourier transform along the screen with spatial wavenumber  $s$ ,  $\Delta r$  is the distance between phase screens along the range direction,  $k$  is the free-space wavenumber,  $X$  is the ratio of plasma frequency to transmission frequency (squared), and  $U$  is a factor to account for electron collisions. In equation (1.23), the elements of the  $2 \times 2$  coupling matrix  $M$  are given by

$$\begin{aligned} M_{11} = M_{22} &= \frac{1}{2} \left\{ \exp \left[ i \frac{kX(z)Yl_r}{2U^2} r \right] + \exp \left[ -i \frac{kX(z)Yl_r}{2U^2} r \right] \right\} \\ M_{12} = -M_{21} &= \frac{i}{2} \left\{ \exp \left[ -i \frac{kX(z)Yl_r}{2U^2} r \right] - \exp \left[ i \frac{kX(z)Yl_r}{2U^2} r \right] \right\} \end{aligned} \quad (1.24)$$

where  $Y$  is proportional to the magnetic field strength, and  $l_r$  is the direction cosine of the magnetic field in the range direction.

The first two stages of this algorithm are nearly the same as in the wave-optics algorithm we have been using for an unmagnetized plasma (except that our propagator is slightly more general). Implementing the Brent et al., algorithm only required adding the third stage, applying magnetic

coupling, to our existing wave-optics code. Once we accomplished this we repeated the OTHR modeling simulation that we conducted previously (Figures 2 and 3), this time including magnetic field effects. The results of this simulation are shown in Figures 5 and 6. Color scales are relative with red = high and blue = low. The field was excited with a vertically polarized wave (along  $z$ ) at the location of the OTHR (lower left). The arrival angle spectrum (dB) shows the direction of downward and upward travelling waves at the ground as a function of local elevation angle.

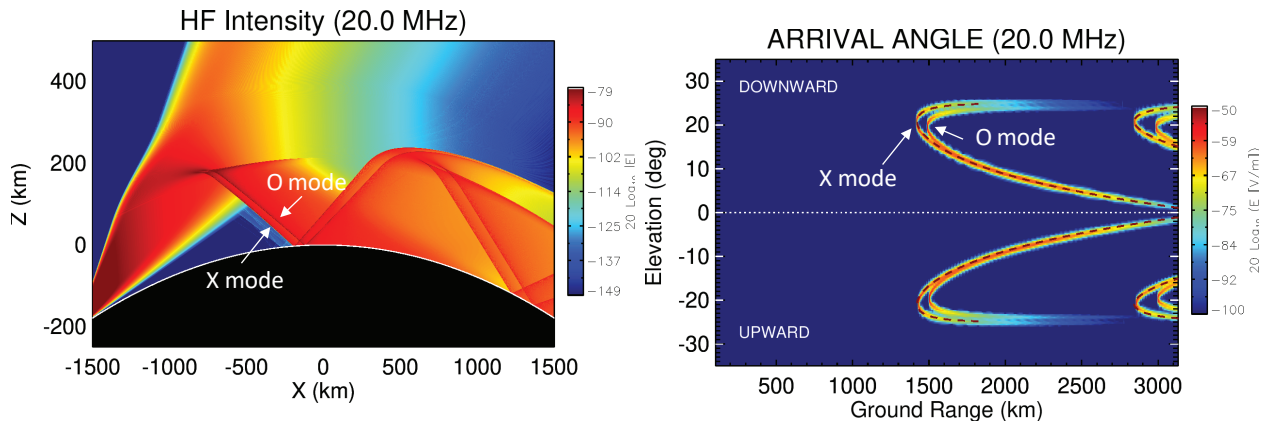


Figure 5. HF power (dB) (left) and arrival angle spectrum (right) for wave-optics simulation of a 20 MHz wave propagating through a quasi-parabolic ionosphere including magnetic field effects

The intensity of the electric field is shown in Figure 5. It is instructive to compare this figure with the intensity shown in Figure 2 and 3, before magnetic field effects were included. When magnetic field effects are included there are two distinct concentrations of field intensity following the skip zone, whereas there is only one without magnetic field effects. We postulate that these two field concentrations correspond to the ordinary and extraordinary propagation modes, which are the characteristic waves in a cold magneto-plasma. Although the solution does not identify which mode is which during the computation, we have labeled the two modes on the plots in Figure 5 on the basis of independent ray-tracing calculations which we will discuss later.

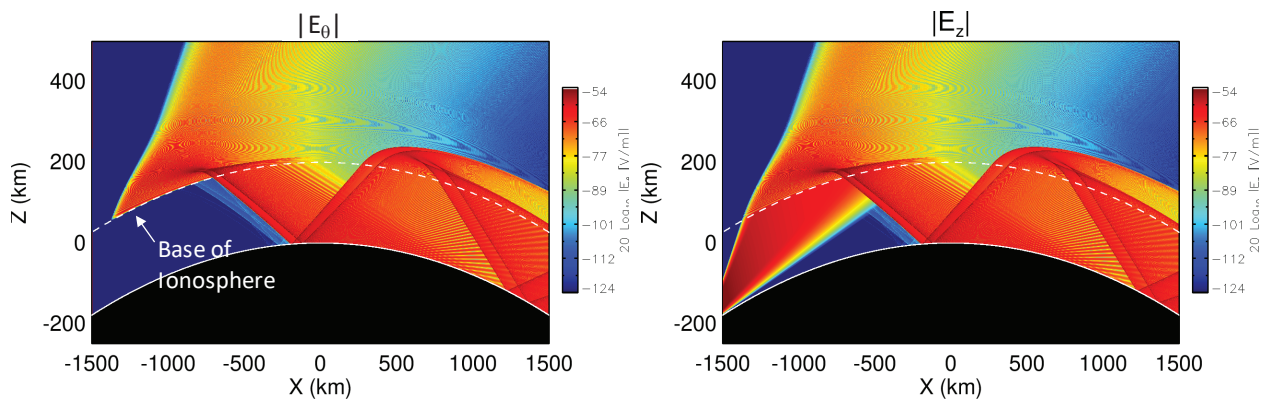


Figure 6. Azimuthal (left) and cross-range (right) components of the electric field for the same simulation as in Figure 5

Note the behavior of the field components is shown in Figure 6. Near the source, only the cross-field component is present since the source is polarized in this direction (by our construction). There is no azimuthal contribution to the field until the wave crosses the base of the ionosphere, which is a discrete boundary for a quasi-parabolic ionosphere. Once the wave enters the ionosphere, the field components rotate due to the magnetic coupling, which requires that both an external field and plasma are present. In effect, when the linearly polarized transmitted wave enters the ionosphere it splits into the two characteristic waves for a birefringent magnetized plasma. These characteristic waves each have azimuthal and cross-field contributions.

To support our interpretation of these results, we configured the magneto-ionic ray-tracer PHaRLAP (Cervera and Harris, 2014) to simulate this same OTHR propagation scenario. Figure 7 shows the results, with rays corresponding to the ordinary (O) mode shown in blue and corresponding to the extraordinary (X) mode shown in red. The ray-paths for O and X are identical until the waves reach 200 km (dashed line), which is the base of the quasi-parabolic ionosphere that we imposed. After the waves cross this ionospheric boundary, the paths of the O and X modes diverge. In particular, the X-mode rays penetrate deeper into the ionosphere (i.e. attain a higher altitude) before they are reflected back down to Earth. As a result, the X-mode rays hit the ground at shorter range than the O-mode rays. Using the ray-tracer in this way, we are able to identify the two characteristic modes in the wave-optics calculation (Figure 5). In particular, the arrival angle plot shows excellent agreement between the wave-optics and ray-trace calculations for both ordinary and extraordinary modes.

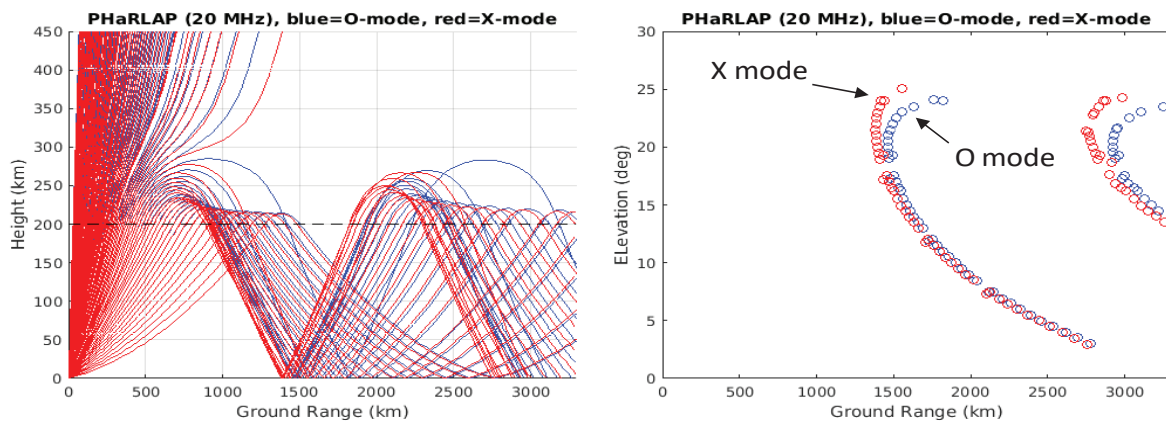


Figure 7. Rays for the ordinary (O) and extraordinary (X) modes using the magneto-ionic ray tracer PHaRLAP (left), arrival angle for the O and X rays determined via ray-tracing (right)

Despite the apparent success of Brent et al.'s algorithm for incorporating magnetic field effects into the wave-optics model, there are some shortcomings which we would like to discuss. First, these authors found it necessary to linearize the susceptibility tensor in order to derive their results. This linearization restricts the validity of the simulations to the case where  $X \ll 1$  and  $Y \ll 1$ . More specifically, the authors recommend restricting the technique to transmit frequencies  $>25\text{MHz}$  during daytime and  $>10\text{ MHz}$  during the night. Furthermore, their reliance on the parabolic

approximation restricts the range of scattering angles that can be modeled when ionospheric disturbances are present. In the next section, we describe an alternative approach, based on the vector forward-propagation equation (FPE), which can mitigate some (but not all) of these deficiencies.

Before we conclude, we would like to illustrate a weakness of the algorithm by Brent et al., namely its ability to model Faraday rotation. Faraday rotation is a fundamental property of birefringent media in which the two characteristic modes travel at different speeds, thereby accumulating a relative phase difference as they propagate. To study this effect using the Brent et al. algorithm, we simulated longitudinal propagation through a homogenous medium with a constant plasma frequency equal to 6 MHz. An 8 MHz wave that is linearly polarized wave along the  $z$ -direction was used as the excitation field. The magnetic field was oriented along the propagation direction ( $x$ ). Figure 8 shows the field components in the plane transverse to the direction of propagation. Figure 9 shows the Faraday rotation angle ( $\Omega$ ) from the numerical simulation (black line), which is given by the argument (i.e. arctangent) of the ratio  $E_y / E_z$ .

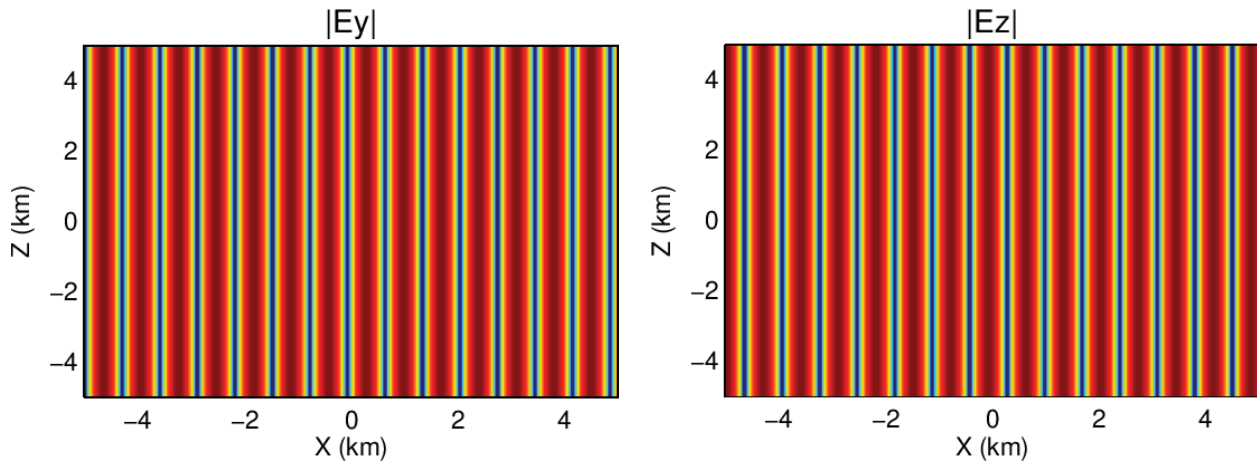


Figure 8. Simulation of longitudinal propagation for a linearly polarized wave (along  $z$ ) using the Brent et al. algorithm

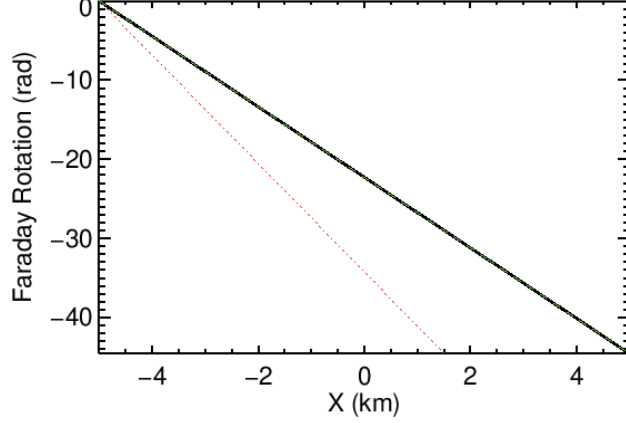


Figure 9. Faraday rotation rate for the simulation shown in Figure 4 (black line), analytic rotation rate for the Brent et al. algorithm (green dashed line), and exact result for longitudinal propagation (red dotted line)

From equations (1.23) and (1.24) it is straightforward to compute the Faraday rotation for the Brent et al. numerical algorithm in analytic form:

$$\Omega = \frac{k}{2} \frac{Xl_r Y}{U^2} (x - x_0) \quad (1.25)$$

This analytic result is shown in Figure 9 with a green dashed line, which is nearly indistinguishable from our simulation results. While it is encouraging that our simulation recovers this analytic result, neither agree with the exact result for longitudinal propagation through a cold magneto-plasma, which is given by (Yeh and Liu, 1972):

$$\Omega = \frac{k}{2} (n_L - n_R) (x - x_0) = \frac{k}{2} \left[ \sqrt{1 - \frac{X}{1+Y}} - \sqrt{1 - \frac{X}{1-Y}} \right], \quad (1.26)$$

where  $n_L$  and  $n_R$  represent the refractive indices for left and right circularly polarized waves, respectively.

### 3.4 Vector Propagation Modeling – the VFPE

The derivation of the vector forward propagation equation, which we refer to as the VFPE, draws heavily on material in Chapter 7 of *Waves and Fields in Inhomogeneous Media* (Chew, 1990).

The following time-harmonic form of Maxwell's equations characterize ionospheric propagation at frequencies above 3 MHz:

$$\nabla \times \mathbf{E} = -i\omega \mathbf{B} \quad (1.27)$$

$$\nabla \times \mathbf{H} = i\omega \mathbf{D} \quad (1.28)$$

$$\mathbf{B} = \mu_0 \mathbf{H} \quad (1.29)$$

$$\mathbf{D} = \epsilon_0 \bar{\epsilon} \cdot \mathbf{B} = 0. \quad (1.30)$$

The fields  $\mathbf{D}$  and  $\mathbf{B}$  are measured in flux units. The fields  $\mathbf{E}$  and  $\mathbf{H}$  represent electric and magnetic field intensities, respectively. The quantities  $\mu_0$  and  $\epsilon_0$  are fundamental constants such that

$$c = 1 / \sqrt{\mu_0 \epsilon_0} \quad (1.31)$$

is the vacuum velocity of light. Radio frequency and angular frequency are related as  $f = 2\pi\omega$ . The dielectric tensor,  $\bar{\epsilon}$ , is defined as

$$\bar{\epsilon} = \bar{I} + \bar{\chi} \quad (1.32)$$

where  $\bar{I}$  is the identity matrix and  $X\bar{\chi}$  is the susceptibility matrix, which is written as a product of a spatially varying scalar ( $X$ ) and a  $3 \times 3$  tensor ( $\bar{\chi}$ ). Several seminal textbooks, e.g. Budden (1985), Yeh and Liu (1972), and Davies (1996), present calculations of the susceptibility matrix for a cold, collisionless plasma. The Appendix to our publication (Rino and Carrano, 2021a) summarizes the results together with a procedure for calculating the ordinary ( $O$ ) and extraordinary ( $X$ ) characteristic modes that propagate in a uniform anisotropic ionosphere.

The vector wave equation is obtained by eliminating  $\mathbf{B}$  and  $\mathbf{H}$ :

$$\nabla \times \nabla \times \mathbf{E} - (\omega^2 / c^2) \bar{\epsilon} \mathbf{E} = 0. \quad (1.33)$$

Applying the identity

$$-\nabla \times \nabla \times \mathbf{E} = \nabla^2 \mathbf{E} - \nabla(\nabla \cdot \mathbf{E}), \quad (1.34)$$

puts the wave equation in its more familiar form

$$\nabla^2 \mathbf{E} + (\omega^2 / c^2) \bar{\epsilon} \mathbf{E} = \nabla(\nabla \cdot \mathbf{E}). \quad (1.35)$$

Whereas  $\nabla \cdot \mathbf{D} = \mathbf{0}$  and  $\nabla \cdot \mathbf{B} = \mathbf{0}$  follow from (1.27) and (1.28), the  $\nabla(\nabla \cdot \mathbf{E})$  term is finite but usually neglected on the basis that the structure does not induce steep gradients. In this development we assume that the magnetic field is uniform, whereby the variation of the dielectric tensor is confined to the scalar multiplier  $X$ . For the ionospheric medium the perturbation in refractive index is

$$X = (\omega_p / \omega)^2, \quad (1.36)$$

where  $\omega_p$  is the electron plasma frequency. For propagation calculations the vector homogeneous wave equation is written as

$$\nabla^2 \mathbf{E} - k^2 (\bar{I} + X \bar{\chi}) \mathbf{E} = 0. \quad (1.37)$$

To pursue the identification of characteristic modes, we let

$$X = X_0 + \Delta X, \quad (1.38)$$

where  $X_0$  is spatially invariant. Proceeding formally, the free-space dyadic Green function is used to convert (1.37) to the equivalent integral representation

$$\begin{aligned} \mathbf{E}(\mathbf{r}) = & \mathbf{E}_0(\mathbf{r}) + k^2 X_0 \bar{\chi} \iiint \mathbf{E}(\mathbf{r}') [\bar{I} + (1/k)^2 \nabla \nabla] G(|\mathbf{r} - \mathbf{r}'|) d\mathbf{r}' \\ & + k^2 \bar{\chi} \iiint \Delta X(\mathbf{r}') \mathbf{E}(\mathbf{r}') [\bar{I} + (1/k)^2 \nabla \nabla] G(|\mathbf{r} - \mathbf{r}'|) d\mathbf{r}' \end{aligned} \quad (1.39)$$

where  $\mathbf{E}_0(\mathbf{r})$  is a solution to the free-space wave equation, and

$$G(|\mathbf{r} - \mathbf{r}'|) = \frac{\exp(ik|\mathbf{r} - \mathbf{r}'|)}{4\pi|\mathbf{r} - \mathbf{r}'|}. \quad (1.40)$$

To identify the leading terms following the equal sign in (1.39), we make the following observation. If  $\Delta X(\mathbf{r}) = 0$ , then  $\mathbf{E}(\mathbf{r})$  must be a solution to the characteristic equation, namely a superposition of characteristic modes. It follows that

$$\mathbf{E}_c(\mathbf{r}) = \mathbf{E}_0(\mathbf{r}) + k^2 X_0 \bar{\chi} \iiint \mathbf{E}(\mathbf{r}') [\bar{I} + (1/k)^2 \nabla \nabla] G(|\mathbf{r} - \mathbf{r}'|) d\mathbf{r}'. \quad (1.41)$$

With this equivalence, the development of the vector FPE follows the development of the scalar FPE in (Rino and Kruger, 2001). The following Weyl decomposition expresses the scalar Greens function as a summation of plane waves

$$G(|\mathbf{r} - \mathbf{r}'|) = 2i \iint \frac{\exp[ikg(\kappa)|z - z'|]}{kg(\kappa)} \exp[i\mathbf{\kappa} \cdot (\boldsymbol{\eta} - \boldsymbol{\eta}')] \frac{d\boldsymbol{\kappa}'}{(2\pi)^2} \quad (1.42)$$

The free-space wave vector is defined as

$$\mathbf{k} = [\boldsymbol{\kappa}, g(\kappa)], \quad (1.43)$$

where

$$\begin{aligned} k_z &= kg(\kappa) \\ g(\kappa) &= \sqrt{1 - (\kappa/k)^2}. \end{aligned} \quad (1.44)$$

Substituting (1.41) and (1.42) into (1.39) and evaluating the Fourier integrations leads to the following spatial Fourier domain representation:

$$\hat{\mathbf{E}}(\boldsymbol{\kappa}; z) = \hat{\mathbf{E}}_c(\boldsymbol{\kappa}; z + z') + 2ik[\bar{I} - \mathbf{ss}] \cdot \int \hat{\mathbf{S}}(\boldsymbol{\kappa}; z') \frac{\exp\{ikg(\kappa)|z - z'|\}}{g(\kappa)} dz' \quad (1.45)$$

where  $\hat{\mathbf{S}}(\boldsymbol{\kappa}; z)$  is the spatial Fourier transform of the product  $\Delta X(\boldsymbol{\eta}, z)E(\boldsymbol{\eta}, z)$  and  $\mathbf{s}$  is a unit vector pointing in the direction of propagation. The forward and backward propagating components can be identified by partitioning the integral over  $z'$  to isolate the respective sources:

$$\begin{aligned} \mathbf{E}^+(\boldsymbol{\kappa}; z) &= \mathbf{E}_c(\boldsymbol{\kappa}; z + z') + 2ik[\bar{I} - \mathbf{ss}] \cdot \int_{-\infty}^z \hat{\mathbf{S}}(\boldsymbol{\kappa}; z') \frac{\exp\{ikg(\boldsymbol{\kappa})|z - z'|\}}{g(\boldsymbol{\kappa})} dz' \\ \mathbf{E}^-(\boldsymbol{\kappa}; z) &= 2ik[I - \mathbf{ss}] \cdot \int_z^{\infty} \hat{\mathbf{S}}(\boldsymbol{\kappa}; z') \frac{\exp\{ikg(\boldsymbol{\kappa})|z - z'|\}}{g(\boldsymbol{\kappa})} dz' \end{aligned} \quad (1.46)$$

Converting the incremental equations to differential form leads to the following coupled differential equations

$$\pm \frac{d\hat{\mathbf{E}}^{\pm}(\boldsymbol{\kappa}; z)}{dz} = ik\hat{\Theta}_c \hat{\mathbf{E}}^{\pm}(\boldsymbol{\kappa}; z) + 2ik[\bar{I} - \mathbf{ss}] \cdot \hat{\mathbf{S}}(\boldsymbol{\kappa}; z) / g(\boldsymbol{\kappa}). \quad (1.47)$$

The contributions of the integral terms are obtained by direct integration. The characteristic mode propagator is developed in detail in (Rino and Carrano, 2021a).

Transformation back to the spatial-domain requires evaluation of the integral

$$\begin{aligned} &\iint \frac{2ik}{g(\boldsymbol{\kappa})} [\bar{I} - \mathbf{ss}] \cdot \hat{\mathbf{S}}(\boldsymbol{\kappa}; z') \exp\{i\boldsymbol{\kappa} \cdot \boldsymbol{\eta}'\} \frac{d\boldsymbol{\kappa}'}{(2\pi)^2} \\ &= k^2 \iint \mathbf{S}(\boldsymbol{\eta} - \boldsymbol{\eta}', z) [\bar{I} + (1/k)^2 \nabla \nabla] G(|\boldsymbol{\eta} - \boldsymbol{\eta}'|) d\boldsymbol{\eta}' \end{aligned} \quad (1.48)$$

We note that

$$\iint G(|\boldsymbol{\eta} - \boldsymbol{\eta}'|) d\boldsymbol{\eta}' = i / (2k). \quad (1.49)$$

We assume that the variation of the source term  $\mathbf{S}(\boldsymbol{\eta} - \boldsymbol{\eta}', z)$  is such that it may be taken outside the integral. As in the scalar case, we make this approximation so that the resulting VFPE equation is expressible in terms of additive contributions from media interaction and free-space propagation—this is required for efficient solution of the VFPE via the split-step method. Proceeding with this assumption (1.48) can be written

$$k^2 \iint \mathbf{S}(\boldsymbol{\eta} - \boldsymbol{\eta}', z) [\bar{I} + (1/k)^2 \nabla \nabla] G(|\boldsymbol{\eta} - \boldsymbol{\eta}'|) d\boldsymbol{\eta}' \square i \frac{k}{2} \mathbf{S}(\boldsymbol{\eta} - \boldsymbol{\eta}', z). \quad (1.50)$$

In retrospect, this assumption is difficult to justify given that the solution to (1.48) is yet unknown. Therefore, we cannot hope to demonstrate that the assumption is valid in all scenarios. In section 3.9, we argue that the approximation should be justifiable when gradients are sufficiently small and when the transmit frequency is sufficiently high.

Substituting (1.50) into (1.48) gives the vector FPE, which can be written as follows:

$$\frac{d\mathbf{E}(\boldsymbol{\eta}, z)}{dz} = \Theta_c \mathbf{E}(\boldsymbol{\eta}, z) + i \frac{k}{2} \Delta X(\boldsymbol{\eta}, z) \bar{\chi} \mathbf{E}(\boldsymbol{\eta}, z). \quad (1.51)$$

where

$$\Theta_c \mathbf{E}(\boldsymbol{\eta}, z) = \iint \hat{\mathbf{E}}(\boldsymbol{\kappa}, z) \exp\{ikn_0 g(\kappa) \Delta z\} \exp\{i\boldsymbol{\kappa} \cdot \boldsymbol{\eta}\} \frac{d\boldsymbol{\kappa}}{(2\pi)^2}. \quad (1.52)$$

If  $\Delta X(\boldsymbol{\eta}, z) = 0$ , the propagation operator characterizes propagation in a homogeneous anisotropic background medium. This is the only case for which  $n_0 \neq 1$ . We argue that in a structured medium, self-consistency requires that we assign  $n_0 = 1$  in the above, in which case the  $c$  subscript may be omitted. To see this, note that with  $\Delta X(\boldsymbol{\eta}, z) = 0$ , equations (1.51)-(1.52) characterize HF propagation in a uniform medium or a medium with  $\boldsymbol{y}$  invariant structure that varies slowly with  $z$ . However, neither the field interacting with the inhomogeneous structure nor the result,  $\Delta X(\boldsymbol{\eta}, z) \bar{\chi} \mathbf{E}(\boldsymbol{\eta}, z)$ , is constrained to be a superposition of characteristic modes. It follows that the only consistent form of the FPE with  $\Delta X$  finite is

$$\frac{d\mathbf{E}(\boldsymbol{\eta}, z)}{dz} = \Theta \mathbf{E}(\boldsymbol{\eta}, z) + i \frac{k}{2} \Delta X(\boldsymbol{\eta}, z) \bar{\chi} \mathbf{E}(\boldsymbol{\eta}, z), \quad (1.53)$$

with

$$\Theta \mathbf{E}(\boldsymbol{\eta}, z) = \iint \hat{\mathbf{E}}(\boldsymbol{\kappa}, z) \exp\{ikg(\kappa) |z - z_0|\} \exp\{i\boldsymbol{\kappa} \cdot \boldsymbol{\eta}\} \frac{d\boldsymbol{\kappa}}{(2\pi)^2} \quad (1.54)$$

If the derivation had started with  $X_0 = 0$ , this result would follow. To demonstrate consistency, we consider the zero magnetic field limit,  $X = 1 - n^2$  and  $\chi = I$ . With  $n \simeq 1 - \Delta n$ , it follows that  $\Delta X/2 \simeq \Delta n$ , which shows that the scalar FPE is a special case of the vector FPE when the external magnetic field effects are negligible. The only constraint on the magnitude of  $\Delta X$  is that  $\Delta X < 1$ , which is ensured by operation above the electron plasma critical frequency.

The vector FPE is fully three-dimensional. However, the computational examples in this report will be considered in its two-dimensional form with  $\boldsymbol{\eta}$  replaced by  $y$ . Our paper (Rino and Carrano, 2021a) shows numerous applications of the VFPE for modeling HF propagation in uniform, layered, and fully inhomogeneous birefringent media.

### *Implementation via the Split-Step Method*

Accepting (1.53) and (1.54) as defining relations, the VFPE integration cycle is initiated with a computation of the interaction of the field with the structure between two defining planes separated by  $\Delta z$ . This is achieved by solving the FPE with the propagation operator neglected:

$$\frac{d\mathbf{E}(y, z)}{dz} = i \frac{k}{2} \Delta X(y, z) \bar{\chi} \mathbf{E}(y, z). \quad (1.55)$$

With the diagonal decomposition

$$\bar{\chi} = \bar{V}^{-1} \bar{D} \bar{V}, \quad (1.56)$$

which is guaranteed by the structure of  $\bar{\chi}$ , the media interaction contribution is reduced to three uncoupled equations,

$$\frac{d\bar{V}\mathbf{E}(y, z)}{dz} = i \frac{k}{2} \Delta X(y, z) \bar{D} \bar{V}\mathbf{E}(y, z). \quad (1.57)$$

The solution is

$$\mathbf{E}_\chi(y, z) = \bar{V}^{-1} \exp\left\{i \frac{k}{2} \Delta X(y, z) \bar{D} \Delta z\right\} \bar{V}\mathbf{E}(y, z). \quad (1.58)$$

The notation  $\mathbf{E}_\chi$  distinguishes the field as an intermediate result to be propagated over the distance between the defining z-planes.

### 3.5 Comparing Brent's Algorithm with the VFPE

After implementing the vector FPE algorithm described in the previous section, we compared the results with Brent's more restrictive vector algorithm (1990). Figure 10 shows the propagation of a 20 MHz signal through a quasi-parabolic ionosphere using Brent's method (left) and the vector FPE (right). The topmost plots show total field intensity. The middle and lower plots show the magnitude of the  $z$  and  $y$  components of the electric field, respectively. The illumination source was linearly polarized in the  $z$ -direction. Both algorithms predict that the downward refracted wave will split into two components as a consequence of the externally applied magnetic field. The splitting occurs because of the birefringence of the ionospheric medium, whereby the ordinary and extraordinary modes travel at different speeds and therefore experience differential refraction effects.

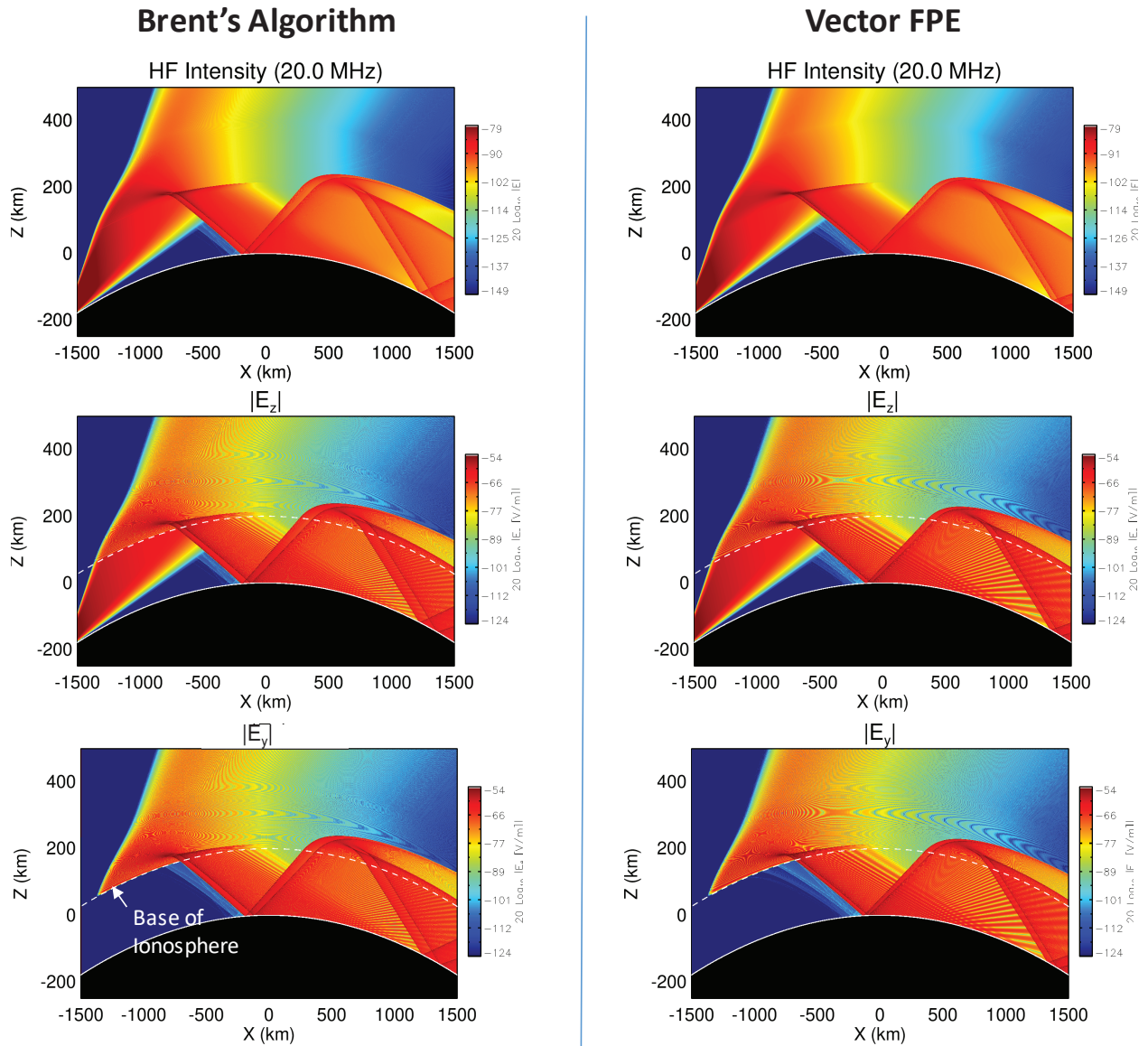


Figure 10. Propagation of a 20 MHz signal propagating through a quasi-parabolic ionosphere simulated using Brent's method (left) and the vector FPE (right)

### 3.6 Boundary Conditions for the Earth Surface

When we use the vector FPE approach to simulate the interaction of HF waves with the ionospheric plasma, we have noted that the approximations we use to impose boundary conditions at the earth surface sometimes produce an unacceptable amount of numerical ‘noise’. In this section, we describe our efforts to improve the treatment of reflecting boundary conditions, particularly when the boundary surface is curved.

With the completion to publication of the boundary-free VFPE (Rino and Carrano, 2021a) we concentrated on surface reflection issues. It is straightforward to implement reflection from a planar boundary, as in the simulation shown in Figure 11. The reflection is imposed via the method

of images (e.g. Levy, 2000), whereby the complex Fourier transform that appears in the propagator for the components of the field is replaced with a sine transform. A phase shift along the screen is imposed to translate the boundary to the bottom of the grid. The sine transform enforces the boundary condition for a perfectly conducting surface, which is zero field at the surface. A second phase shift is then applied to translate the field back up to the curved boundary.

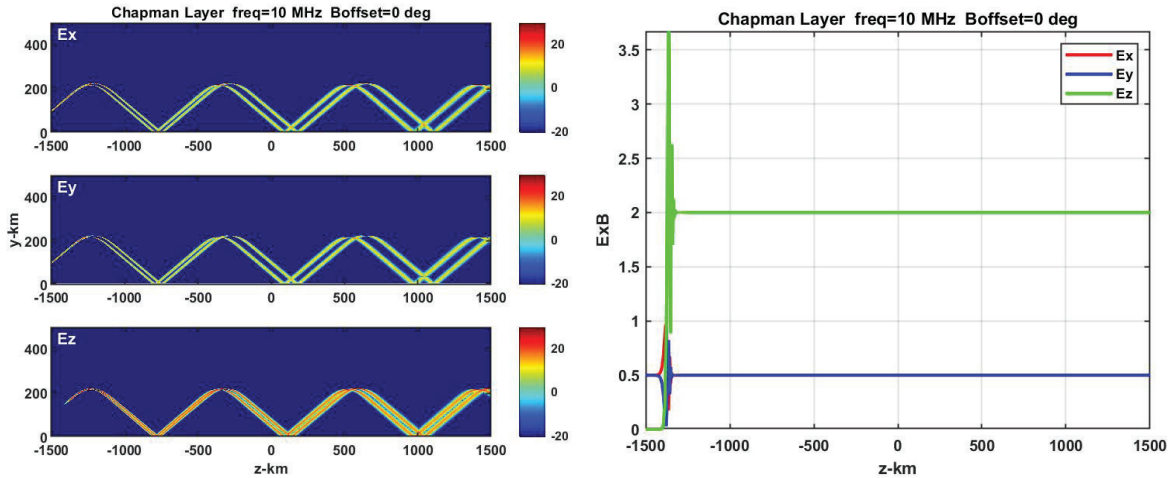


Figure 11. VFPE simulation of multi-hop propagation over a flat perfectly conducting surface

The propagating beams shown in Figure 11 do not show any evidence of spurious noise at the boundary because it is flat. Once we apply curvature to the boundary we observed the noise to problem to appear. The numerical experiments we performed suggest that the amount of noise generated is strongly dependent on the spatial sampling used to conduct the simulation.

To study this effect in closer detail, we simplified the problem by removing both the plasma and the magnetic field from the simulation. The problem we were left to model was the propagation of a thin beam launched downward through free space toward a perfectly conducting planar boundary. The results of the simulation are shown in Figure 12. The spatial separation between phase screens ( $\Delta x$ ) was chosen to be 2 km in this example, which corresponds to approximately 70 wavelengths ( $\lambda$ ) at 10 MHz. As shown in Figure 12, energy was conserved perfectly as the wave propagated, and no numerical noise was evident. In Figure 13, we repeated this simulation for a curved conducting boundary meant to represent the Earth's surface. All other parameters of the simulation were held fixed while we experimented with the spatial separation ( $\Delta x$ ) between the phase screens. The three panels from left to right show results for successively smaller spatial separations:  $\Delta x = 70\lambda$ ,  $\Delta x = 2\lambda$ , and  $\Delta x = 1\lambda$ , respectively. In each case, there was energy loss upon reflection and also numerical noise. Thankfully, both of these problems became less pronounced as the  $\Delta x$  decreases. We observed that a spatial sampling  $\Delta x \approx \lambda$ , reduces the noise to an acceptable level. A small amount of energy is still lost upon reflection, however.

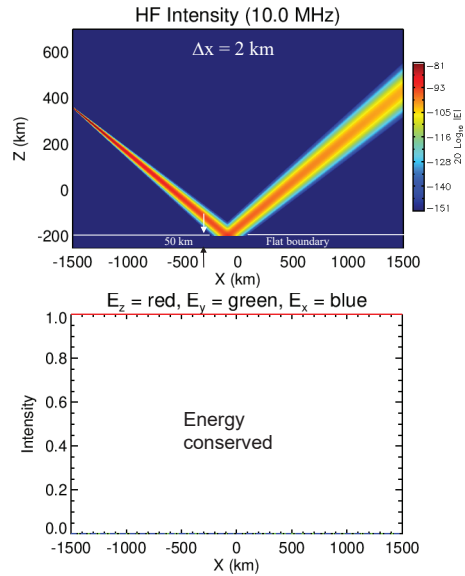


Figure 12. Reflection of a thin beam from a perfectly conducting planar boundary

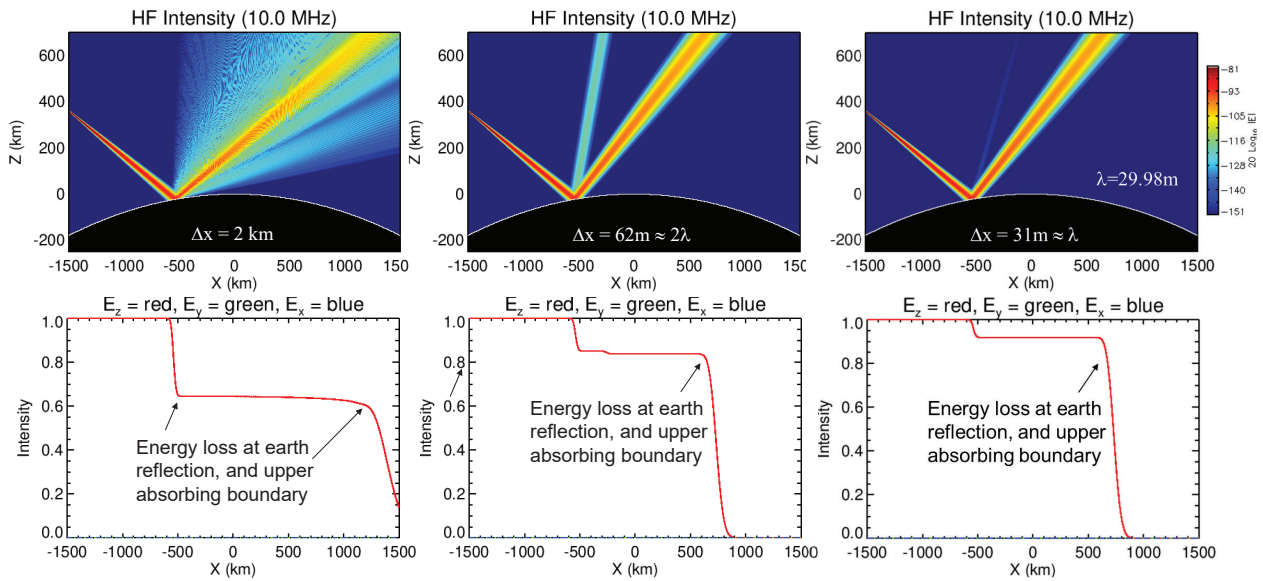


Figure 13. Reflection of a thin beam from a perfectly conducting curved boundary

While we expect the image method will still be a viable and computationally efficient approach for implementing reflecting boundary conditions within the VFPE framework, we decided it would be productive to treat the problem more generally. A boundary surface delineates a discontinuous change in the propagation medium. Surface currents must flow on the boundary to support the discontinuous change. These currents are defined by surface boundary integral equations (BIEs), which formally involve the entire surface. In our second paper published during this project (Rino and Carrano, 2021b), we show that the BIEs can be setup for forward marching solutions that are fully consistent with the VFPE.

However, a much simpler shift-mapping method was introduced by Kuttler and Dockery (1991) and Dockery and Kuttler (1996). The only change needed to accommodate a non-planar surface is the addition of a phase shift that translates the reference to the surface:

$$\exp\{ikg(\kappa_y)\Delta z\} \exp\{i\kappa_y(f(z_n) - f(z_{n-1}))\}. \quad (1.59)$$

It was shown in both Rino and Ngo (1997) and Rino and Kruger (2001) that BIE and shift-map solutions agreed very well. However, the comparisons used sub-wavelength propagation-step sampling for both the BIE and shift-map results. For accommodating smooth surface reflections in VFPE split-step solutions we find that near-wavelength sampling provides good results as indicated by total field intensity conservation through the surface reflection (Rino and Carrano, 2021b).

## 4.0 RESULTS AND DISCUSSION

Given the theoretical framework we have constructed to model the propagation of vector waves through the inhomogeneous ionosphere, we apply it to our intended application. Specifically, we are interested in how ionospheric structure affects the power, arrival angle, and polarization of HF waves and how these effects may impact the performance on an OTHR system. We begin by modeling HF propagation through traveling ionospheric disturbances which may be encountered at all geographic latitudes. Then we consider HF propagation through equatorial plasma bubbles, which are manifestations of a plasma interchange instability that occurs after sunset at low latitudes. These are the primary results of our investigation. Following this, we will discuss some shortcomings of the methodology—in particular, the fact that VFPE tends to underpredict the amount of refractive bending that occurs at HF wavelengths—and how this deficiency might be remedied.

### 4.1 Propagation of Vector Waves through Traveling Ionospheric Disturbances

Traveling ionospheric disturbances (TID) are a particular type of ionospheric structuring caused by the propagation of acoustic and gravity waves from the lower neutral atmosphere into the ionosphere, causing quasi-periodic variations in the local electron density. The presence of TIDs are known to limit the performance of HF systems used for OTHR, communications, and geolocation because the electron density perturbations can cause large variations in signal power, delay, Doppler and arrival angle (Yau et al., 2006; Bianchi et al., 2013). Wave-optics simulation is ideal for exploring the effects of TIDs on HF wave propagation since it directly provides the illumination power everywhere in space. We simulated a sinusoidal perturbation representative of a typical medium scale TID, and we modeled propagation through this structure using the vector FPE. Initially, we found the results difficult to interpret because there are several other mechanisms that can produce fading of the signal even in the absence of TIDs. These mechanisms include multipath fading, polarization fading, and terrestrial multipath. We conducted a series of numerical experiments designed to isolate each of these mechanisms so that we could study them, in turn, before re-introducing the TID into the simulation.

Figures 14-17 show the results of numerical experiments we performed to understand the sources of signal fading in the *absence* of TIDs. The arrangement of plots in each figure is the same. The plot at the upper left shows the plasma frequency used for the simulation (a quasi-parabolic ionosphere with 10 MHz critical frequency, 300 km peak height, and 100 km layer thickness). A 20 MHz signal linearly polarized along the z-axis was transmitted from the location  $x=-1600$  km (just outside the lower left corner of the image). The three panels in the middle row show color contours of total signal intensity, the intensity of left-hand circular polarization (LHCP), and the intensity of right-hand circular polarization (RHCP) throughout the computational domain. The three panels in the bottom row show line plots of total power on the ground, LHCP power on the ground, and RHCP power on the ground, respectively.

The first of these experiments (Figure 14) was configured with no magnetic field and no earth surface. By this we mean that downward traveling waves are not reflected when they reach the ground, they simply pass through it to be absorbed at the lower computational boundary. This is the simplest of the scenarios we ran, and yet the power variations on the ground are still rather

complex. There is very little power on the ground in the skip zone (also called the shadow zone), and there are notable high-frequency power fluctuations at ranges just past the skip zone. These power fluctuations are due to the superposition of low and high (Pedersen) rays which interfere constructively and destructively. This type of signal fading is referred to as multipath fading, and it is commonly observed near the skip zone in HF experiments (see section 7.7.2 of Davies, 1990). The second of these experiments (Figure 15) was configured with a magnetic field of strength  $2.7 \times 10^{-5}$  Tesla oriented along the +x axis and no earth surface. The total power at the ground resembles the previous case (with no magnetic field), with multipath fading evident at the skip zone. The two circular polarizations, on the other hand, show significant fading at all ground ranges. This type of fading is referred to as polarization fading, and it is caused by Faraday rotation of the electric field vector in response to the external magnetic field. Note that the total power, consisting of the summation of the two circular polarizations, does not exhibit fluctuations. The Faraday rotation effect rotates the field vector but does not alter its magnitude. Note that near the skip zone we have a superposition both multipath and polarization fading, which is why the fading of total power in this region differs slightly from that shown in Figure 14.

The third of these experiments (Figure 16) was configured with no magnetic field but with a perfectly conducting earth surface, which reflects waves that are incident upon it. Due to this reflection, two hops of the signal occur within the computational domain. There is a skip zone following each signal hop, and multipath fading can be observed at ranges following each skip zone. Signal fluctuations are present at all ranges in this case, as in the previous. However, in this case the fluctuations are due to terrestrial multipath (mixing of direct path and reflected signals), rather than polarization rotation (which does not occur in this case since the magnetic field is absent). The terrestrial multipath is quite pronounced in this simulation because the transmitter is effectively situated a few km above the earth's surface, due to our choice of boundary condition (Hocke et al., 2003) which allows the waves to penetrate beneath the surface before reflecting. It is interesting to note that terrestrial multipath and polarization fading look quite similar. One way to distinguish them is to note that terrestrial multipath produces fading of the total signal power, whereas polarization fading does not.

The fourth of these experiments (Figure 17) was configured with the magnetic field and perfectly conducting ground surface. The signal fades that result are a linear superposition of multipath fading (high and low rays), polarization fading, and terrestrial multipath (direct path mixing of direct path and reflected signals). Quite a complex pattern of HF signal fading at the ground is present, even without any irregular structure in the ionosphere. These results and conclusions are not new, but they are important to keep in mind when attempting to interpret results obtained under more complex ionospheric conditions. Next, we show the behavior of the signal fading once TIDs have been introduced in the simulation.

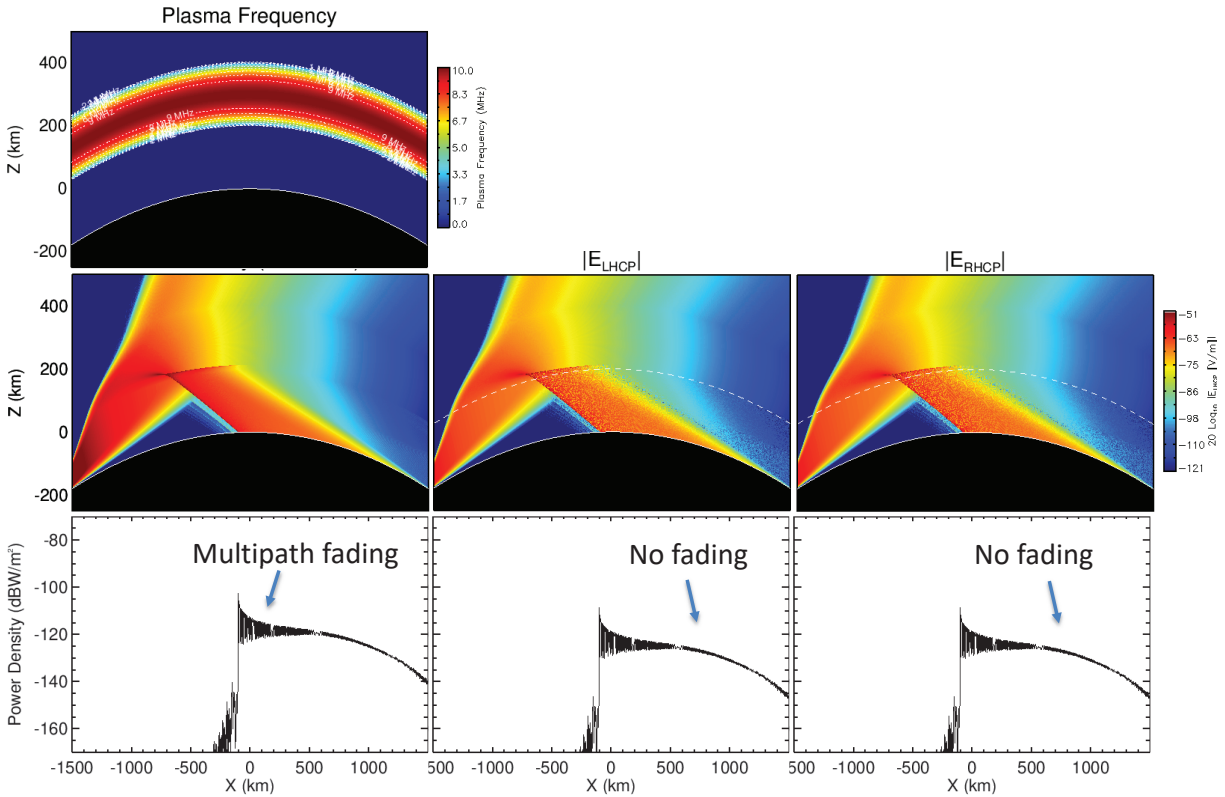


Figure 14. Vector FPE simulation with no ground and no magnetic field

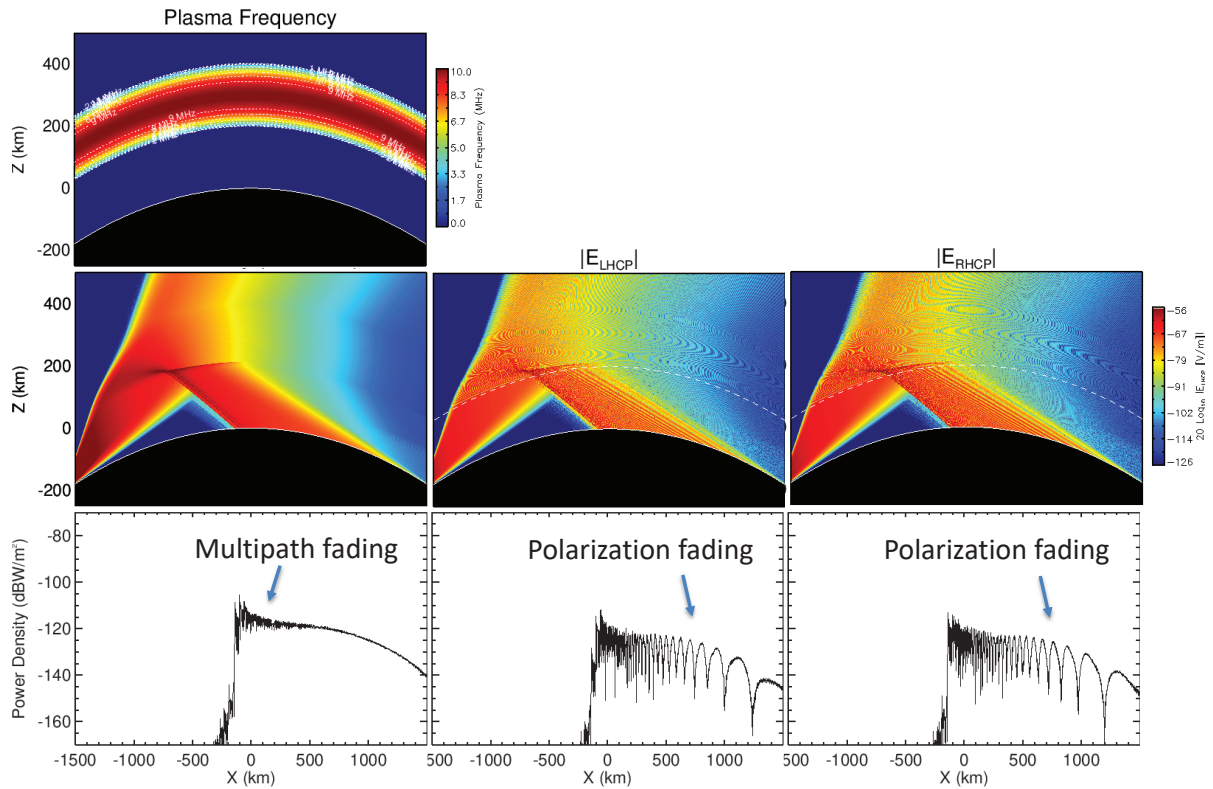


Figure 15. Vector FPE simulation with ground but no magnetic field

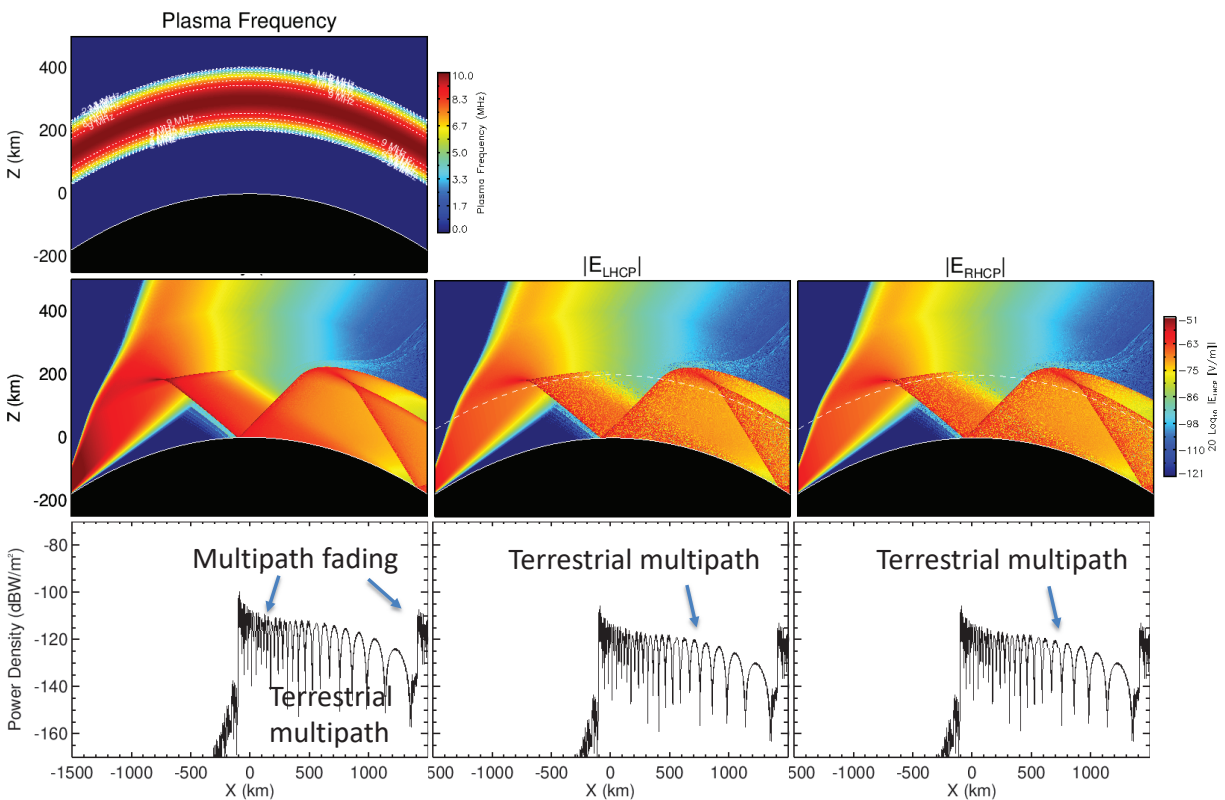


Figure 16. Vector FPE simulation with ground but no magnetic field

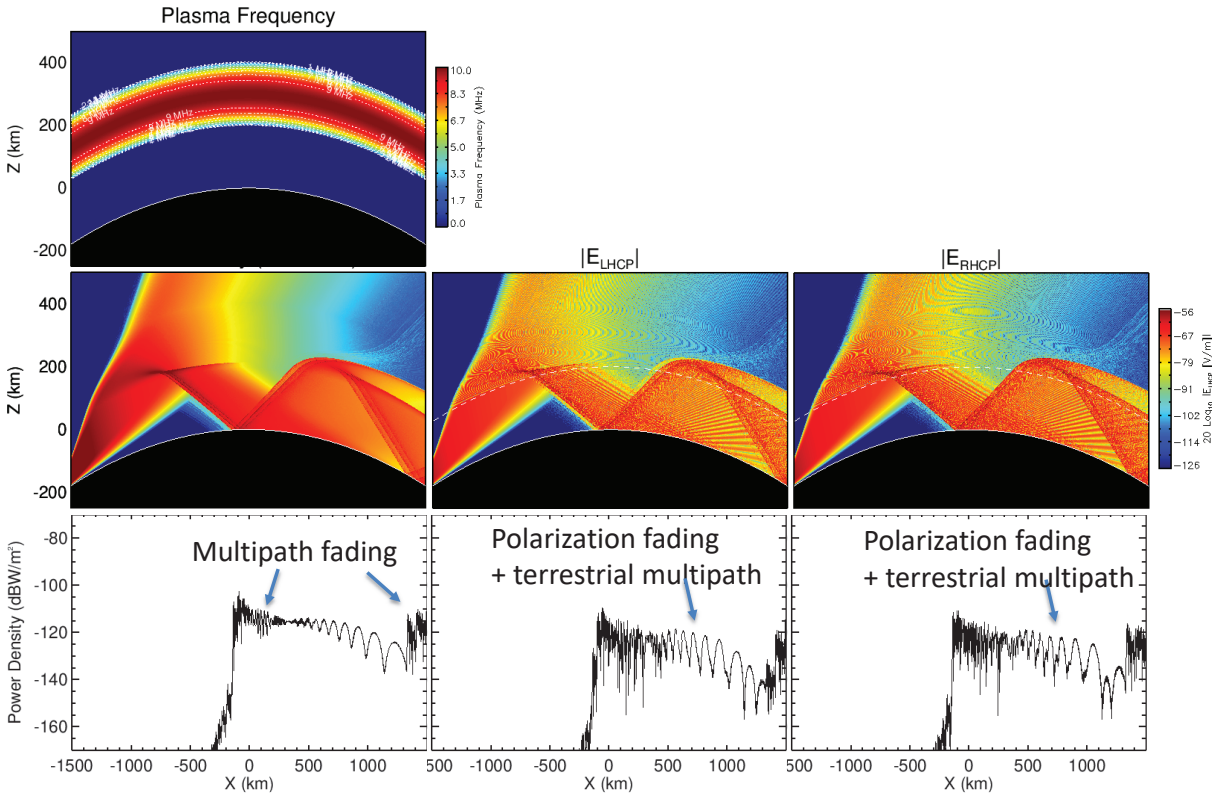


Figure 17. Vector FPE simulation with ground and magnetic field

To model the effect of TIDs on HF propagation, we modulated the background ionosphere in our simulation with a sinusoidal perturbation that is representative of a typical medium scale TID. We assumed a 500 km wavelength and 30 min period, which results in a TID velocity of 280 m/s. The perturbation is altitude dependent, with a peak at the altitude HmF2. The full details of the TID model we implemented are given as equation 7.1 in (Paznukhov, 2004). Figures 18-23 show a snapshot of the simulation results every 300 sec, which is 1/6 of the TID period.

We can infer a number of observations from the results of these simulations. First, it is rather easier to interpret the total power, rather than the power of the individual circular polarizations, since the latter are complicated by polarization fading while the total power is not. Next, it is helpful to consider ranges that are not near either skip zone in order to avoid the effects of multipath fading (interfering high and low rays). What remains at the remaining ranges is terrestrial multipath with the effects of the TID superimposed upon it. From our previous study (Figures 16-17), we know that terrestrial multipath exhibits a quasi-periodic behavior with a ‘local’ wavelength that tends to increase with range (at least for this particular geometry). The fading pattern due to terrestrial multipath is time-invariant, whereas the effects of the TIDs change with time. A sequential examination of the plots in Figures 18-23 show how the TIDs modulate the fading pattern caused by terrestrial multipath, by distorting the propagation paths of energy propagating throughout the space. We note that real TIDs are considerably more complex than the simple sinusoidal model considered here. Hence, the modulation of the propagated wavefronts will be more complex also. Wave-optics simulation is an ideal framework for studying these effects, as the wide-area context it provides is extremely helpful for identifying and interpreting the various wave propagation phenomena at work and also their interplay.

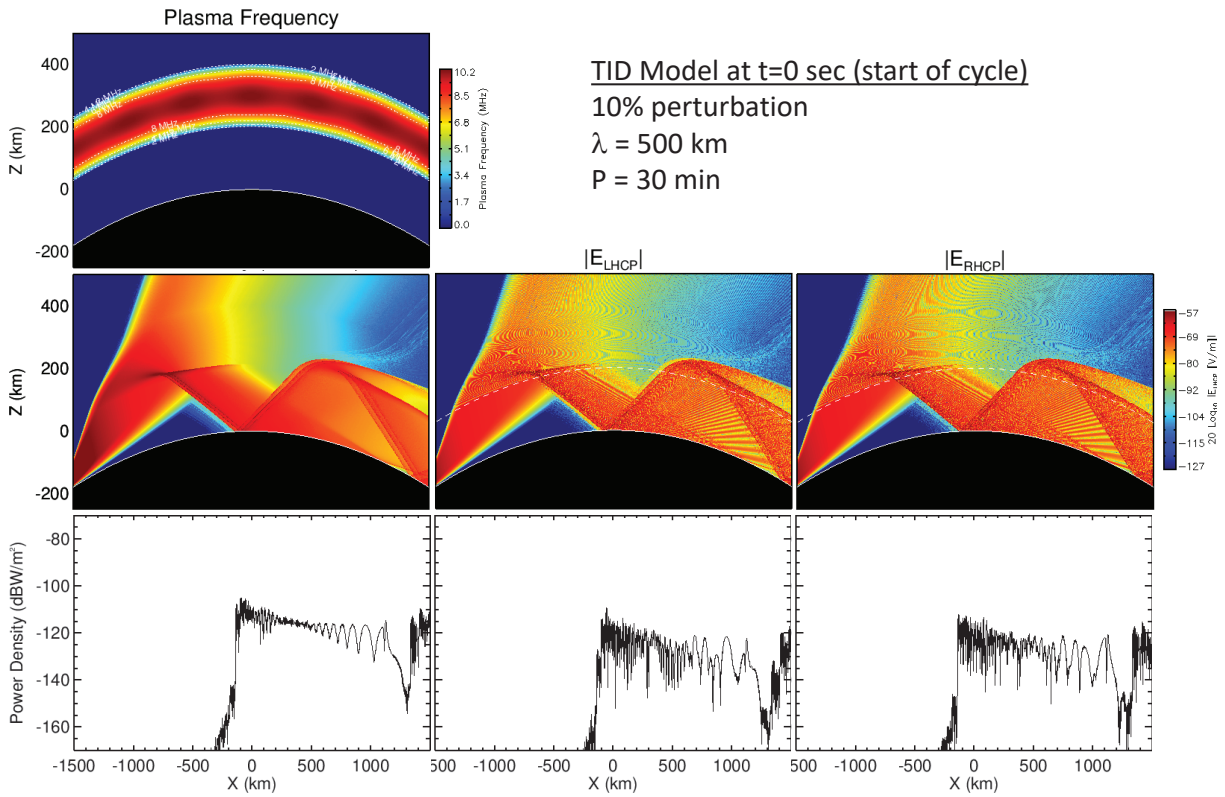


Figure 18. TID simulation at t=0 sec

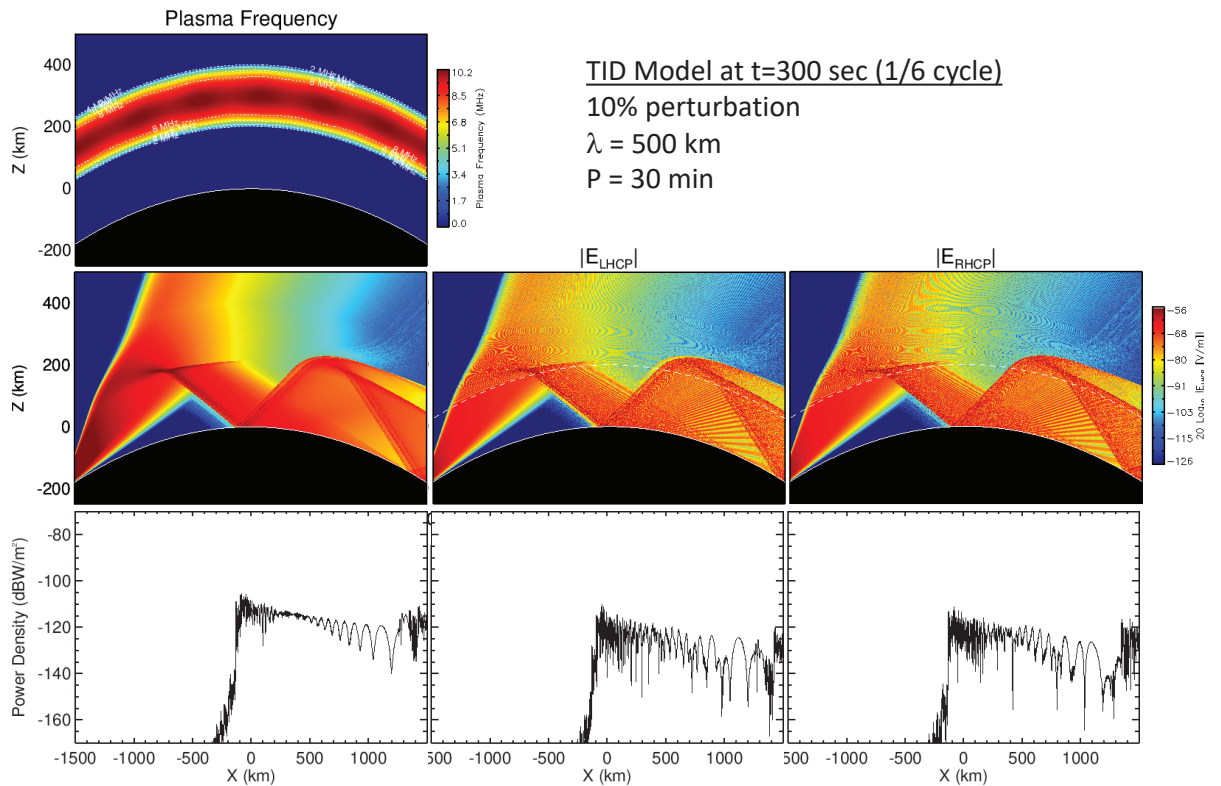


Figure 19. TID simulation at t=300 sec (1/6 cycle)

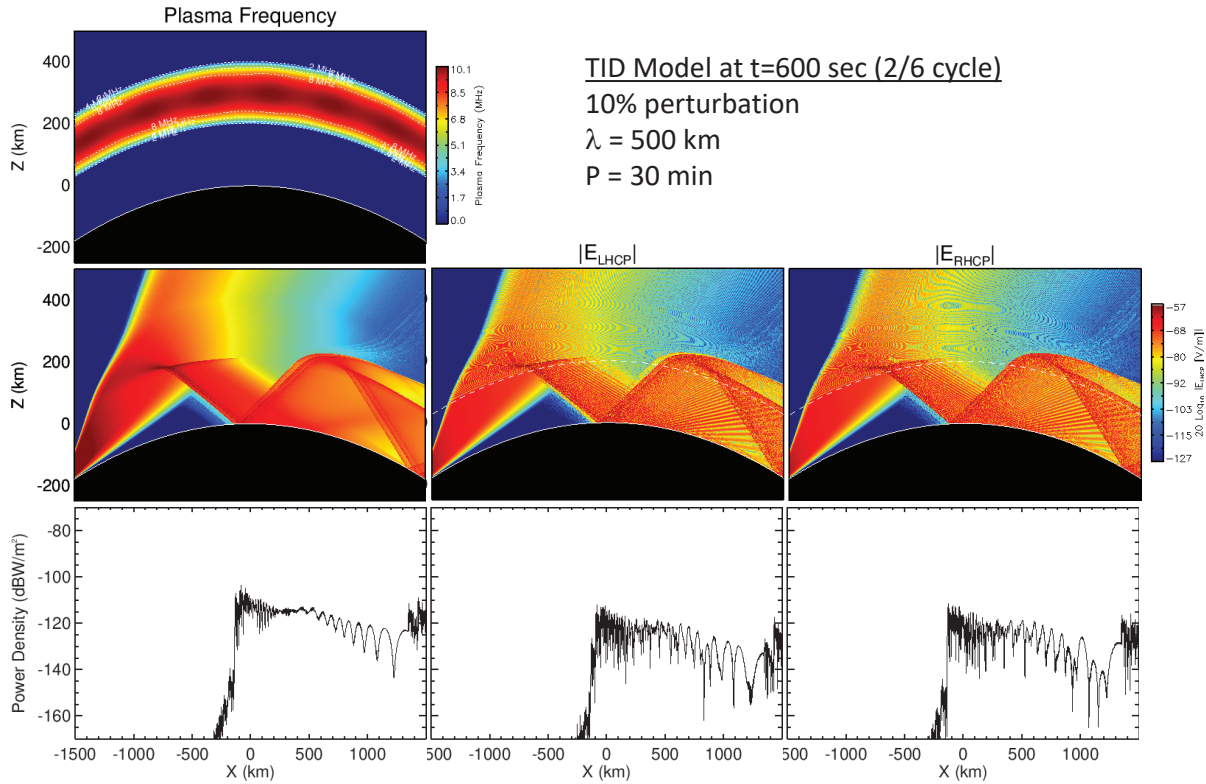


Figure 20. TID simulation at t=600 sec (2/6 cycle)

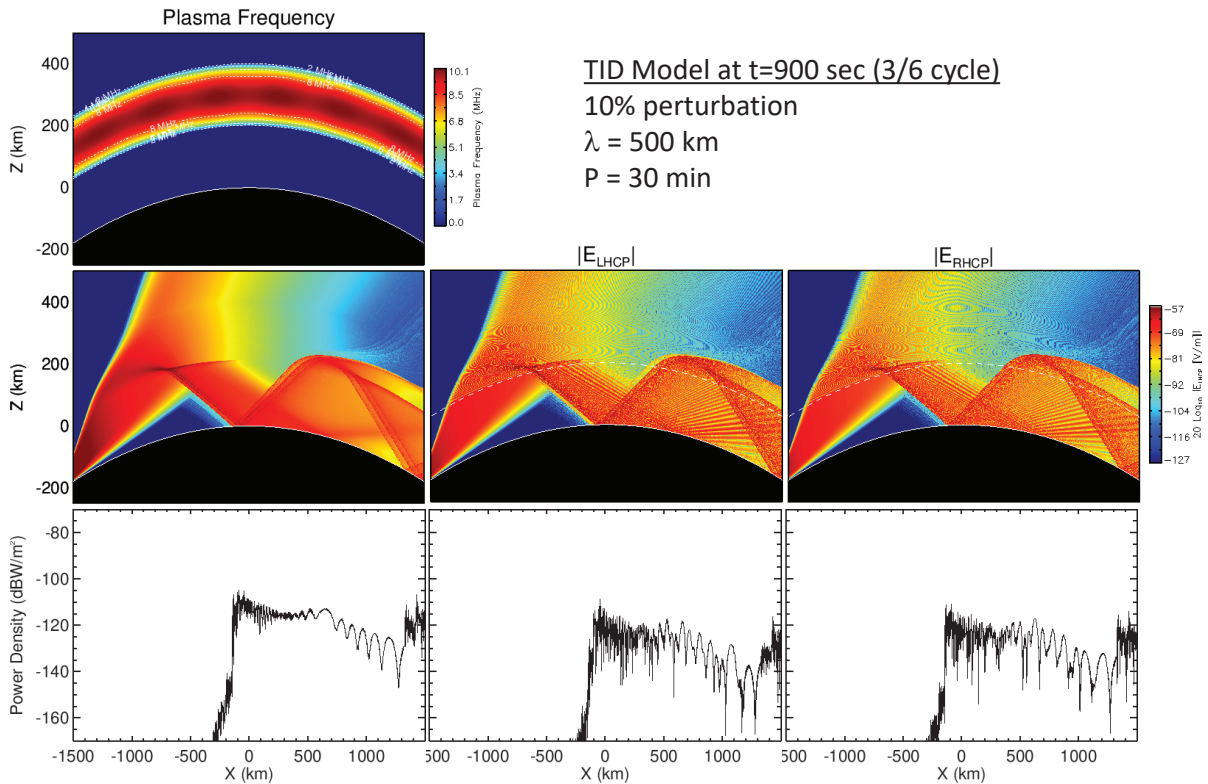


Figure 21. TID simulation at t=900 sec (3/6 cycle)

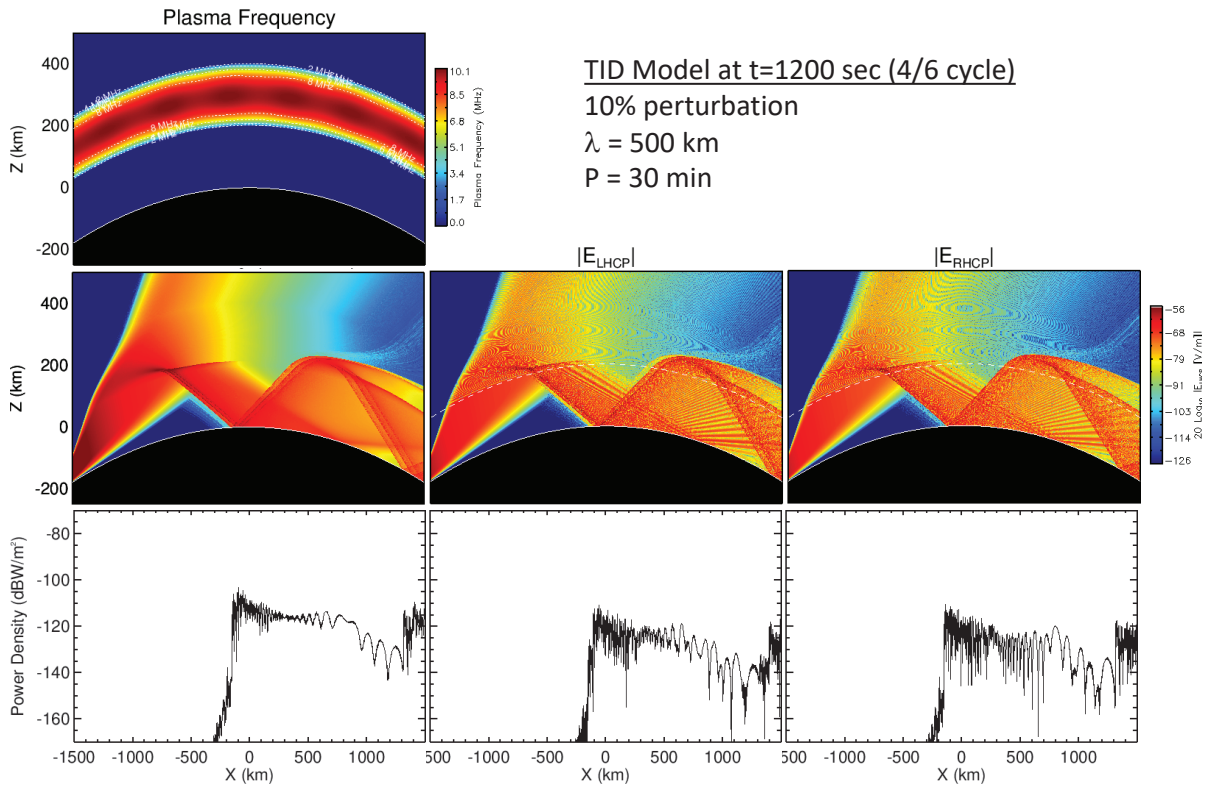


Figure 22. TID simulation at t=1200 sec (4/6 cycle)

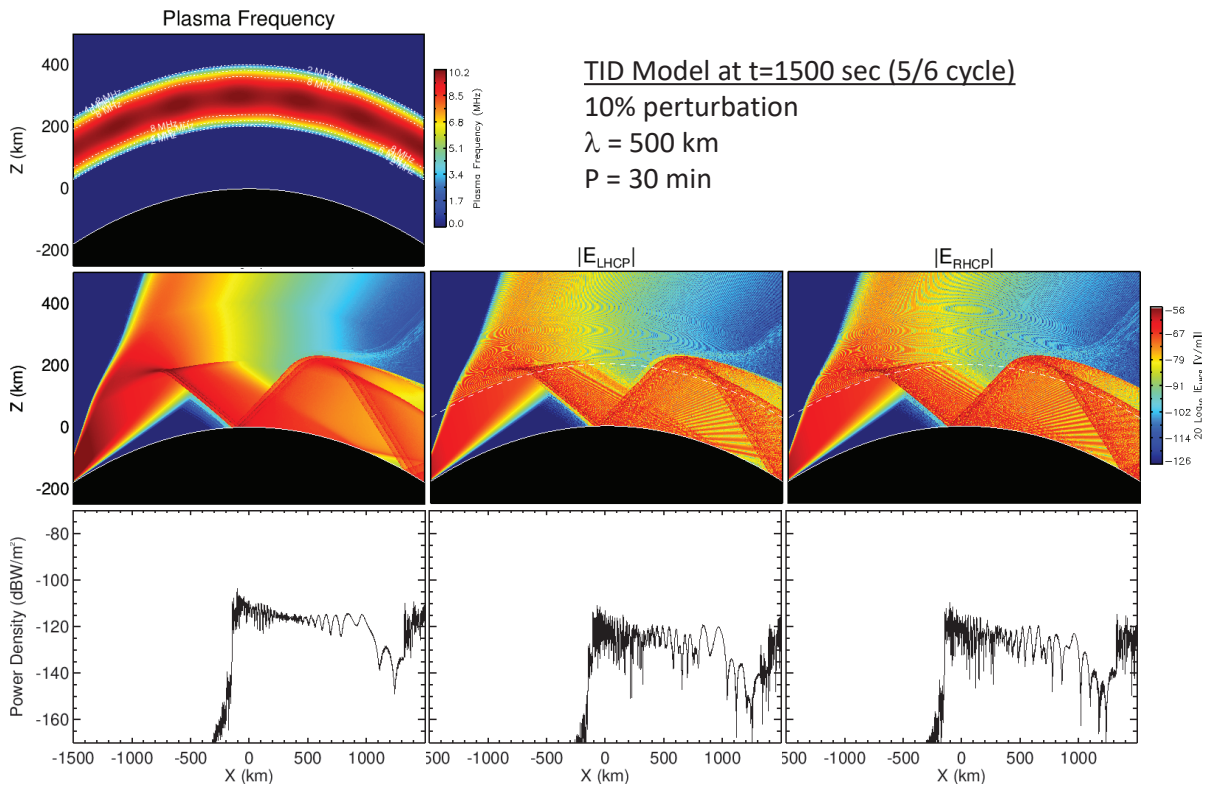


Figure 23. TID simulation at t=1500 sec (5/6 cycle)

## 4.2 Propagation of Vector Waves through Developing Spread-F

Equatorial plasma bubbles (EPB) are ionospheric structures consisting of partially depleted background plasma superimposed with turbulence consisting of irregularities with a wide range of spatial scales, from tens of km to meters or less. Equatorial plasma bubbles form in the equatorial ionosphere after sunset when recombination of the bottomside ionosphere causes sharp vertical gradients in density that are unstable to the generalized Rayleigh-Taylor mechanism (which resembles the instability that causes a less dense neutral fluid to rise through a heavy fluid that is balanced above it). The plasma turbulence embedded within EPBs produces scintillation of radio-waves that transect them, and degrade the performance of radar, communications, and global navigation satellite systems. EPBs in the low-latitude ionosphere are responsible for producing most intense natural scintillation observed anywhere in the world.

For this study we used an electron density field provided by direct numerical simulation of EPB structures provided by Yokoyama (2017). Yokoyama produced this numerical density field by evolving the continuity and steady-state momentum equations for ions and electrons and the divergence-free current condition. The details of the calculation are provided in his paper, and a snapshot of the evolving density field (in units of  $\text{cm}^{-3}$ ) is shown in Figure 24. The longitudinal extent of Yokoyama's computational domain is 3 deg (330 km), however, which is much smaller than the HF propagation circuits in which we are interested. Therefore, it was necessary to extend Yokoyama's data in some fashion for our intended purpose. Initially, we experimented with a simple periodic extension of the data in longitude, but this produced very many EPB structures with almost no region of quiescent ionosphere in between. We decided that a more physically realistic configuration could be produced by replicating a small number of structures via periodic extension (we chose three), and then embedding these structures in a background consisting of a zonal average of the data (to smooth out the disturbances). The result is shown in Figure 25, expressed in terms of plasma frequency (MHz).

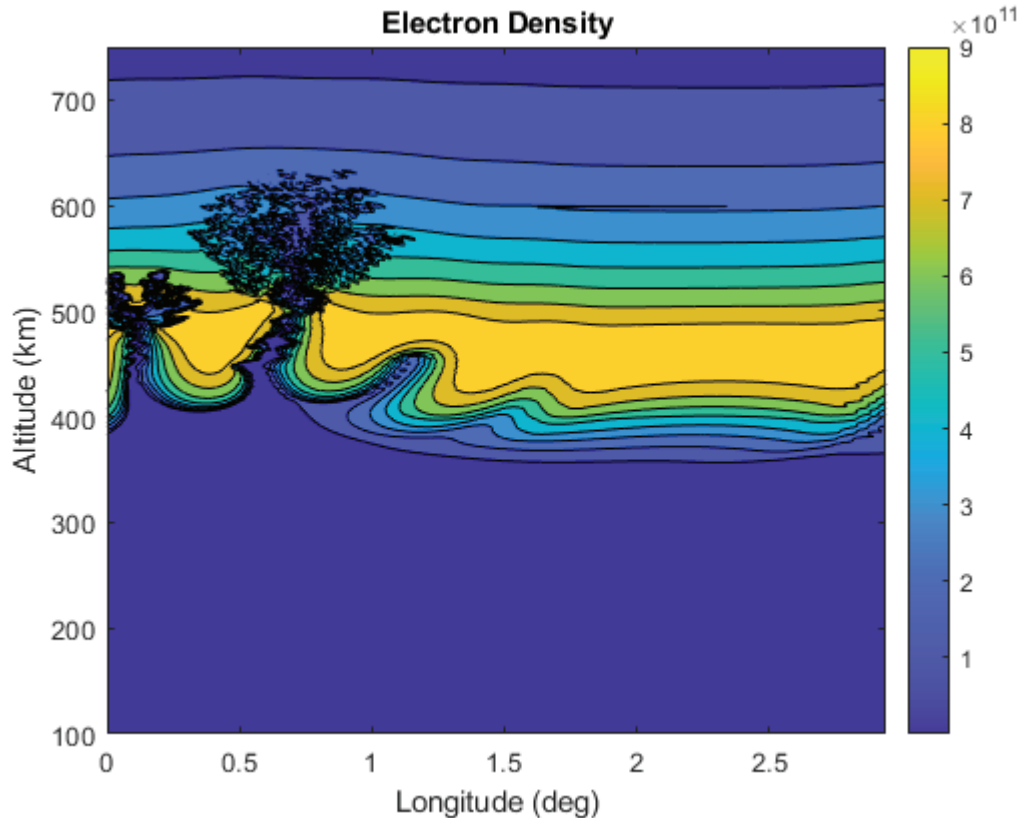


Figure 24. Electron density field containing EPBs generated by Yokoyama (2017)

Next, we performed the propagation simulation by solving the vector FPE. We assumed a 15 MHz transmitted wave with vertical polarization. We implemented a fairly wide beam with the aim of fully-illuminating the EPB structures. We used 1500 samples along the  $x$ -axis, yielding a spatial resolution of  $\Delta x = 2$  km. We used  $2^{18}$  samples along the  $z$ -axis, yielding the sub-wavelength spatial sampling  $\Delta z = 4.00$  m. We assumed a magnetic field strength of  $2.7 \times 10^{-5}$  Tesla, directed along the  $+z$ -axis. Finally, we assumed infinitely conducting boundary conditions at the Earth surface. Figures 26-29 show the results of the vector FPE simulation. We repeated this simulation using 4 times more samples along the propagation direction, and noted no substantial changes in the results (which suggests that our sampling is probably adequate).

In this simulation, by construction, the HF wave travels through a smooth ionosphere until the first EPB structure is encountered at approximately -300 km. The smooth ionosphere refracts the transmitted wave, turning some of the power enough to travel beneath the EPB structure leaving it largely unaffected by its presence. At higher altitudes, the HF wave interacts directly with the EPB structure, which causes a filamentary structure to develop in the wave intensity. Very many distinct propagation paths through the disturbed regions are evident as these filaments are refracted and multiply scattered by irregularities in the underlying turbulence. The close-up of the interaction region shown in Figure 28 highlights these filamentary structures, which are known to be associated with strong focusing effects (Martin and Flatté, 1998). Similar filamentary structure adorns the cover of Rino's book on scintillation (2011). Many of the filaments survive in-tact when the wave returns to Earth, producing strong localized enhancements in the power along the ground

(plot not shown). Interspersed between these localized enhancements are signal fades. These fades and enhancements are a manifestation of HF scintillation that would be measured by a receiver located in the illumination region on the ground (i.e. at ranges past the skip zone). Other filaments are refracted upward through the topside into space, not returning to the ground. The highly complex illumination pattern on the ground could not be predicted via tracing rays because diffraction effects are not modeled. This represents a major advantage of the wave-optics approach.

While these filaments in some ways resemble the striations of the configuration space model (Rino et al., 2018), these two phenomena are in fact unrelated. Striations are associated with magnetic lines of force, which organize the plasma into tube-like structures due to the increased mobility of electrons along the magnetic field direction. Filaments are enhancements in wave intensity caused by refractive focusing under conditions of very strong scatter.

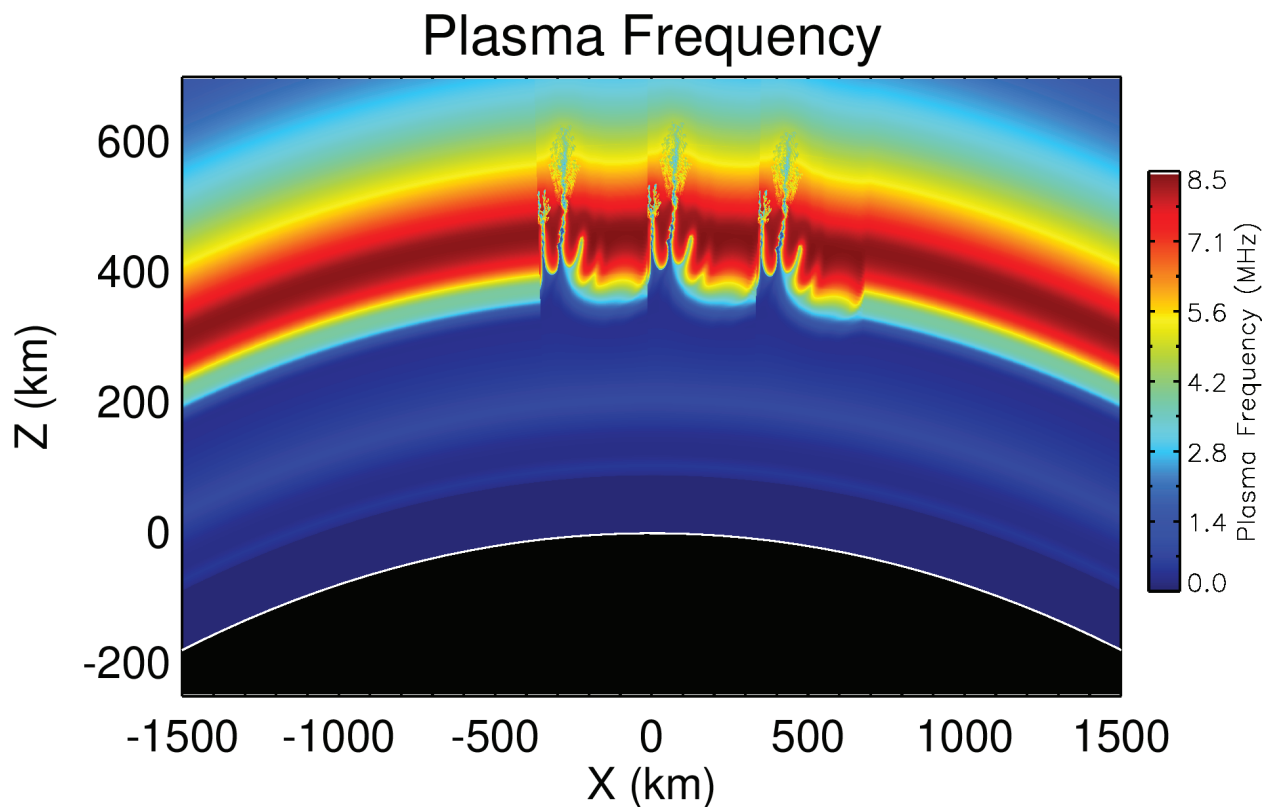


Figure 25. Plasma frequency used in our vector FPE simulations

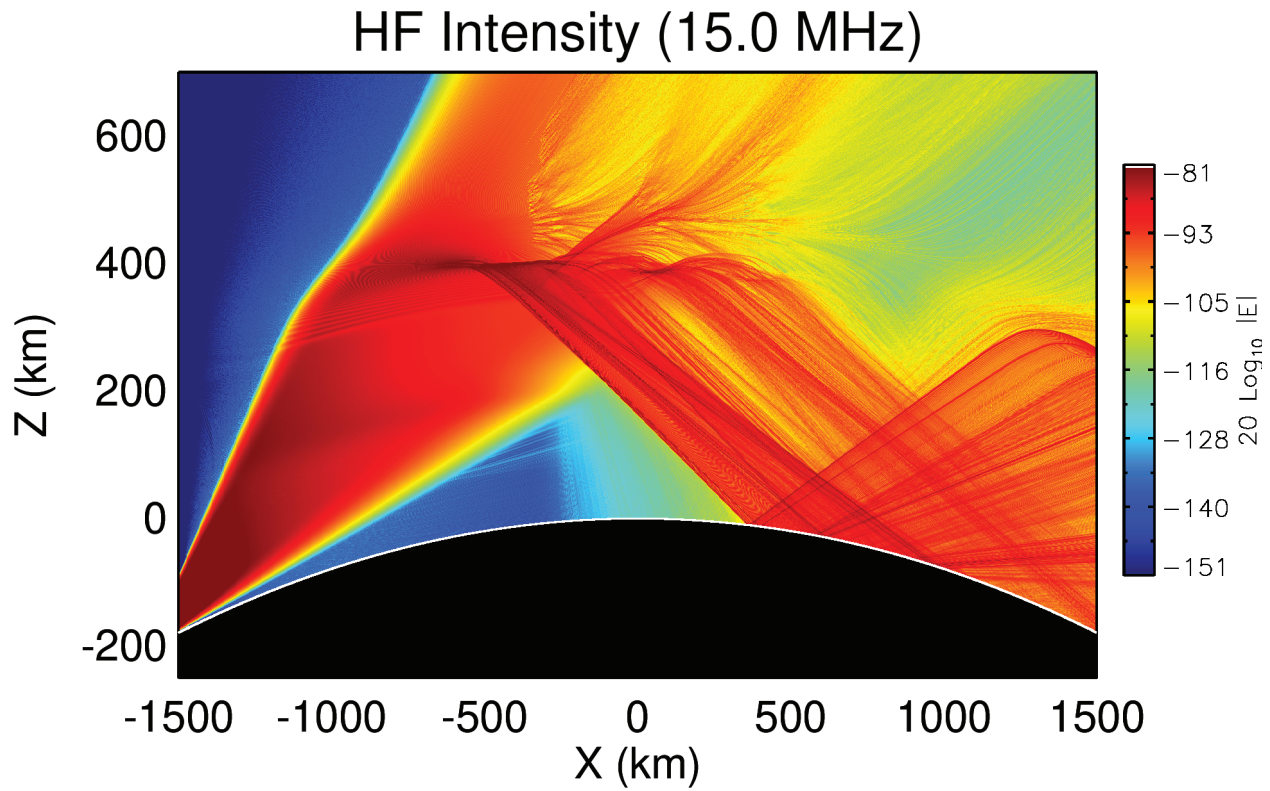


Figure 26. Total HF intensity from the vector FPE simulation

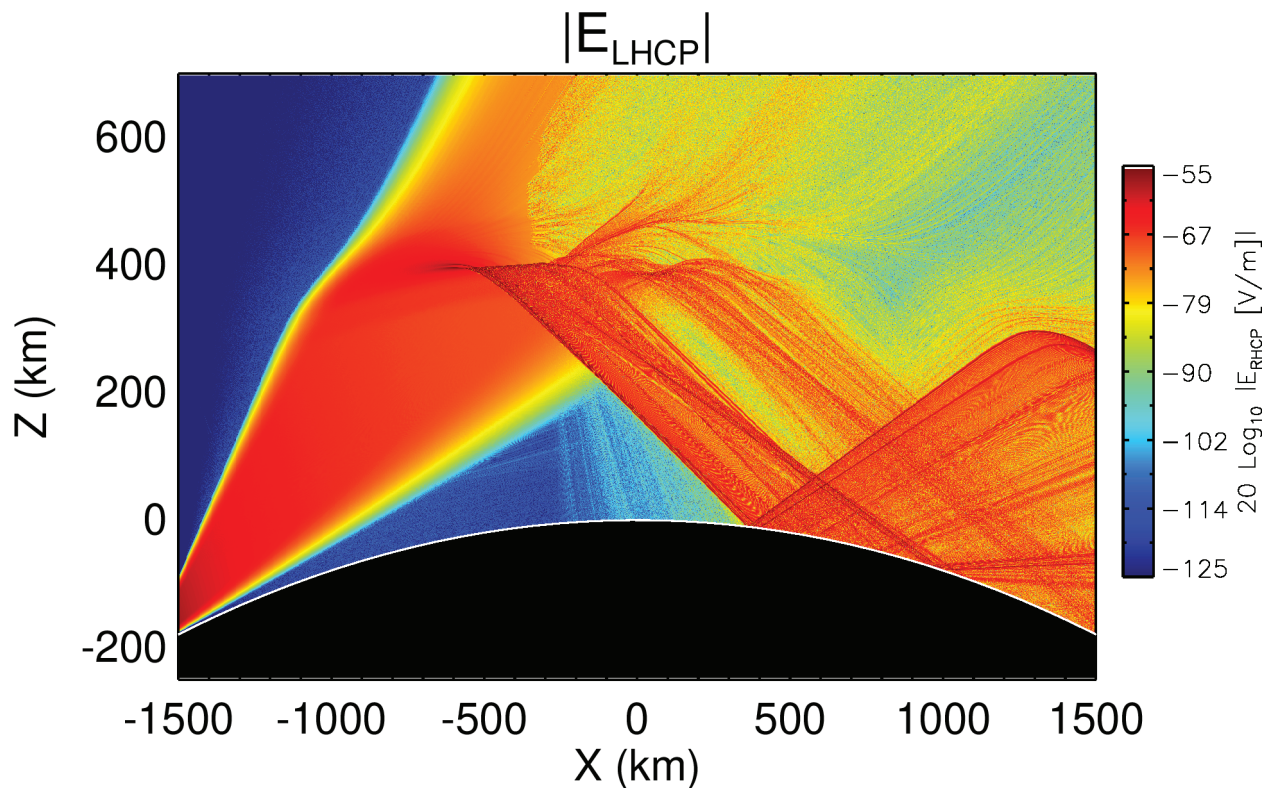


Figure 27. Left-hand circularly polarized power from the vector FPE simulation

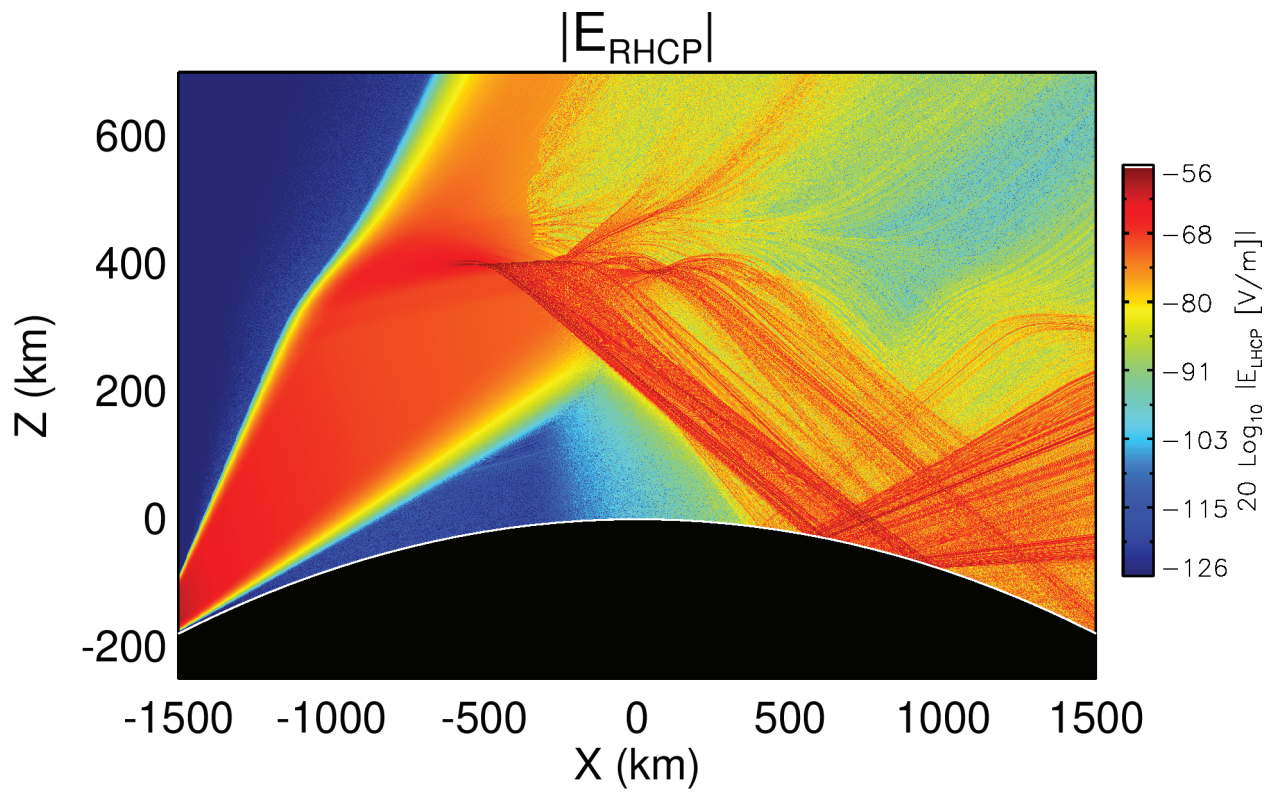


Figure 28. Right-hand circularly polarized power from the vector FPE simulation

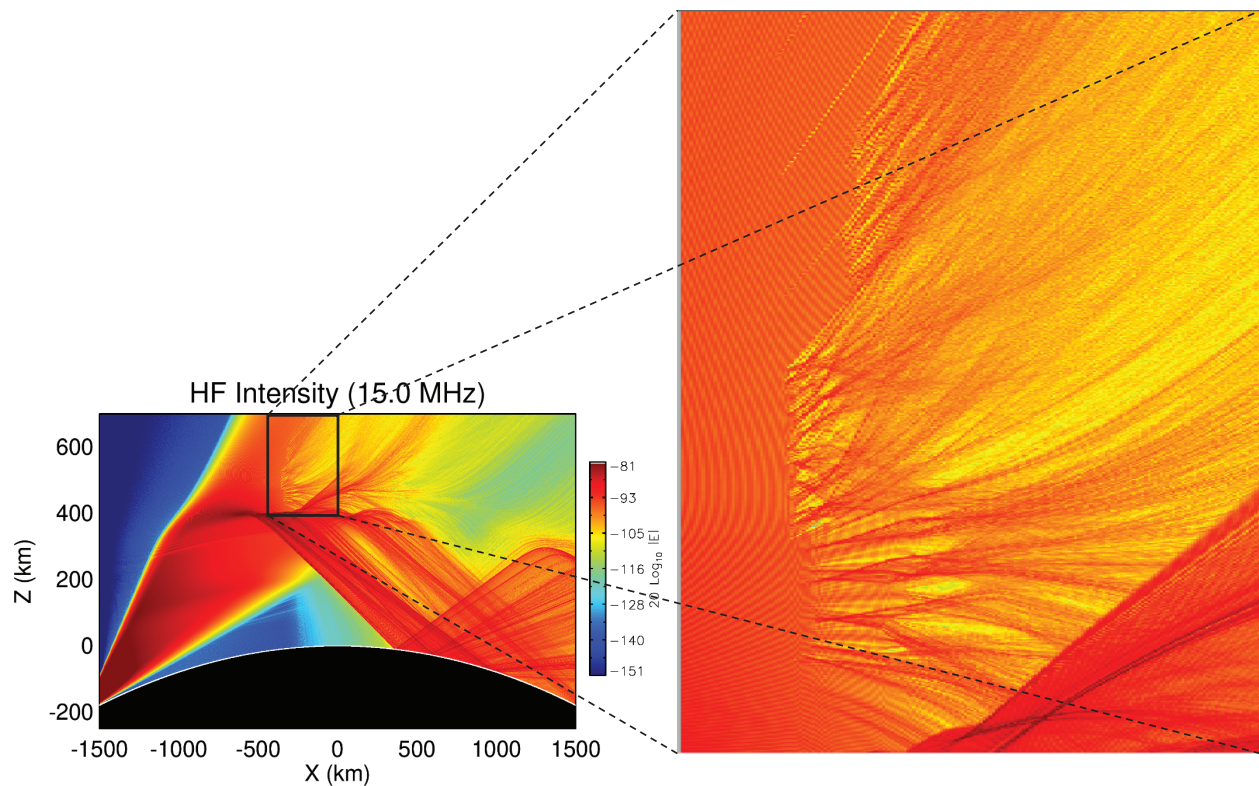


Figure 29. Close-up of the region where HF waves interact with the equatorial plasma bubbles

### 4.3 VFPE and Ray Theory

At this point, we return our attention to the consistency between VFPE and ray-trace solutions to vector propagation problems, since we noted some discrepancies that we wish to better understand.

Solutions to the wave equation and the VFPE are constrained only by the susceptibility tensor,  $\Delta\mathcal{X}(y, z)\chi$ . In particular, there is no prior identification of characteristic modes. In Rino and Carrano (2021a) we showed that in a medium with gradients confined to the propagation direction, solutions to the two-dimensional VFPE can be constructed from superpositions of O and X characteristic modes. The characteristic modes are defined by the Appleton–Hartree equations as summarized in the Appendix to (Rino and Carrano, 2021a). The more general identification of characteristic modes in inhomogeneous media comes from ray theory, which starts with the assumption that the field can be approximated locally as

$$\mathbf{E}(y, z) = \mathbf{E}_0(y, z) \exp\{i\theta(y, z)\}, \quad (1.60)$$

where  $\mathbf{E}_0(y, z)$  varies slowly compared to the eikonal,  $\theta(y, z)$ .

Surfaces of constant  $\theta(y, z)$  identify wave fronts. Rays are paths normal to the wavefronts. Rays are identified by a formal minimization procedure that constructs the shortest paths connecting two points in the medium. The connecting rays are defined by their direction angles at the point of initiation. Introducing the susceptibility matrix leads to a quadratic equation whose roots identify the characteristic modes being traced. To the extent that  $\vartheta = \mathbf{r} \cdot \mathbf{n}$  along the ray, the magnitude of  $\mathbf{n}$  defines the local refractive index. Ray theory shows as well that the fields associated with the characteristic modes have orthogonal elliptical polarizations.

Regarding comparisons between FPE realizations and ray theory, it has been observed that VFPE field structures respond to gradients in the propagation medium with local propagation direction changes. Spatial wavenumber intensity peaks identify local propagation directions. Lines connecting the tangent vectors are effectively ray paths. To associate ray paths with characteristic modes the VFPE  $E_x$  and  $E_y$  field components are combined to extract orthogonal elliptically polarized field components. Formally,

$$E_M = E_x \pm S \cdot E_y, \quad (1.61)$$

where  $S = i$  or  $= 1$  for linear or circular incident polarization, respectively. Anticipating the association with characteristic modes, we let  $M = O$  and  $M = X$  as tentative mode associations.

Figures 30 and 31 summarize extensions of the Chapman layer result introduced in (Rino and Carrano, 2021a), figures 9 and 10. The upper frames in Figures 30 and 31 show the intensities of the candidate mode fields constructed as described above. The lower frames show the corresponding spectral-domain intensities plotted against normalized spatial wavenumber. The  $\pm 1 \kappa_y/k$  range includes all propagating waves. The peak intensities of the extracted modes and their spectral decompositions can be associated with ray positions and directions, respectively.

Discontinuous direction reversals identify the locations of surface reflections. The extracted peak intensities and directions are shown in Figure 32.

Figure 33 shows a comparison of the VFPE O and X mode traces from the upper frame of Figure 31 with ray-trace calculations from the PHaRLAP code. The ray-trace solutions (blue) are refracted back toward the surface before the VFPE solutions (red). In effect, the VFPE media interaction is weaker than it should be. Although it is purely conjectural, if  $\Delta X(\eta)$  were the leading term in a perturbation series, the more accurate form would be  $\Delta X(\eta) + \Delta X(\eta)^2/2$ . Figure 34 shows that the VFPE-Ray trace comparison improved when the *corrected* media-interaction term,  $X \rightarrow X + X^2/2$ , was used. The PHaRLAP ray trace and the VFPE results are indistinguishable on the scale plotted. The same agreement was found when the magnetic field direction was varied and when the magnetic field was set to zero. Note that in Figures 32, 33, and 34 tracks of peak intensity are shown rather than the fields themselves.

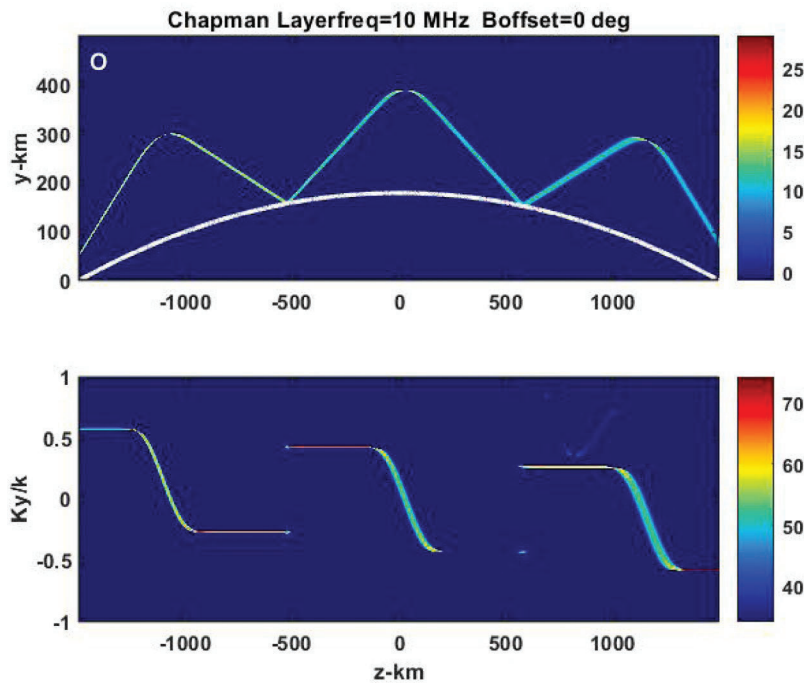


Figure 30. Upper frame shows the dB intensity of the elliptically polarized beam response identified as the O mode, lower frame is the corresponding spectral intensity normalized to the wave vector magnitude in dB units

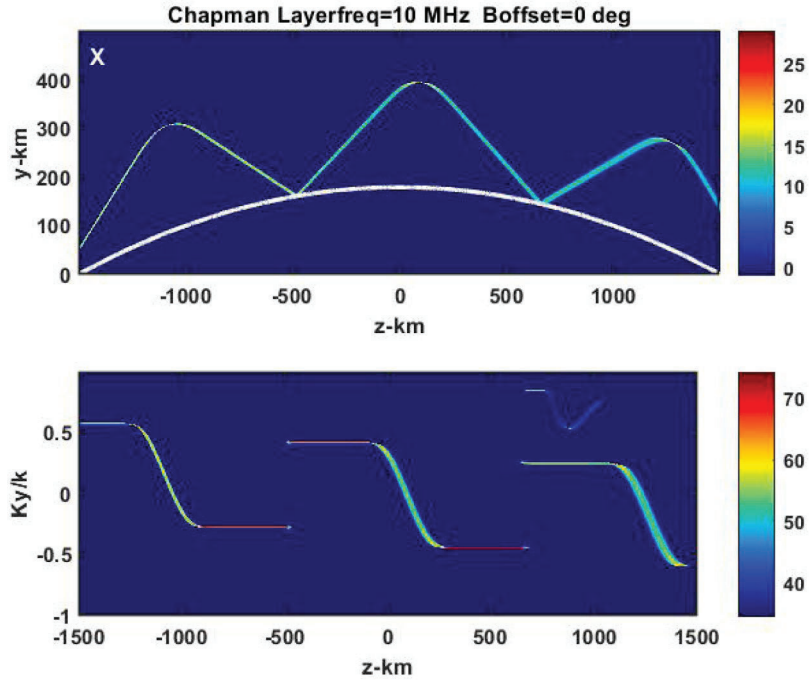


Figure 31. Upper frame is the dB intensity opposite elliptically polarized beam response identified as the X mode, lower frame is the corresponding spectral intensity normalized to the wave vector magnitude in dB units

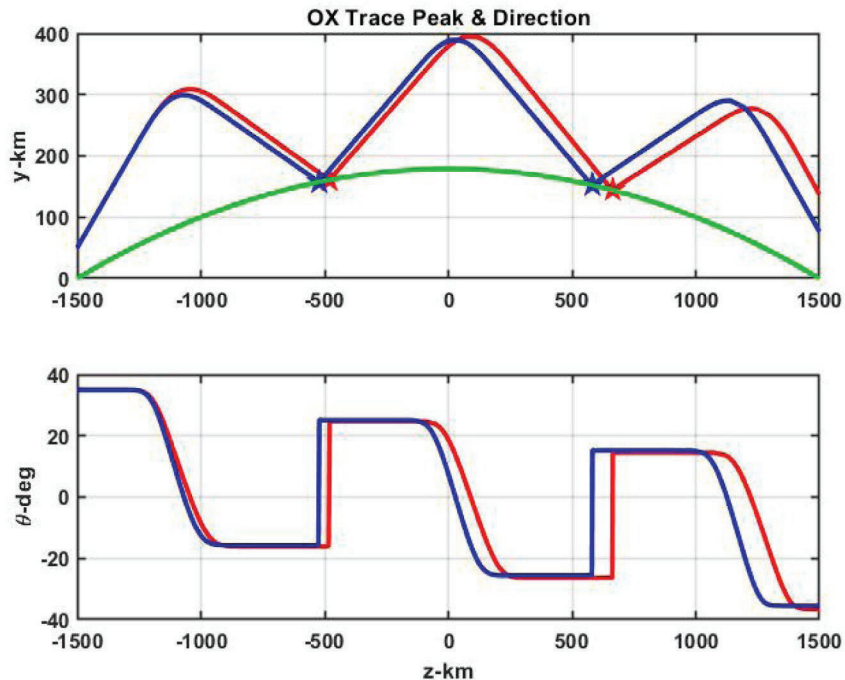


Figure 32. Upper frame shows the O mode (red) and X mode (blue) peaks, lower frame shows the corresponding spectral-domain peaks plotted against propagation direction

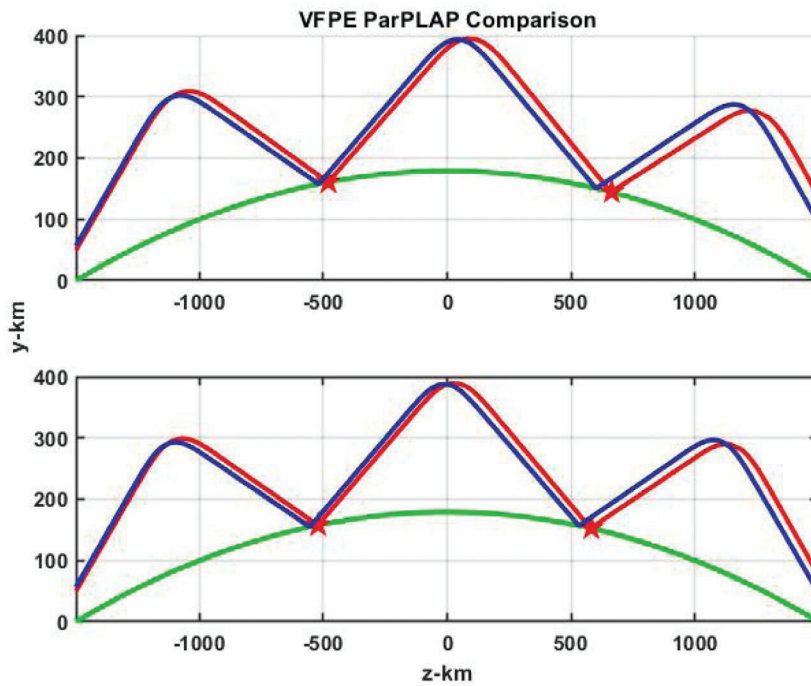


Figure 33. Upper frame compares the O-mode trace shown in the upper frame of Figure 32 (red) with the O-mode trace predicted by the PHaRLAP code (blue), lower frame shows the same comparison for the X-mode trace and the PHaRLAP code prediction

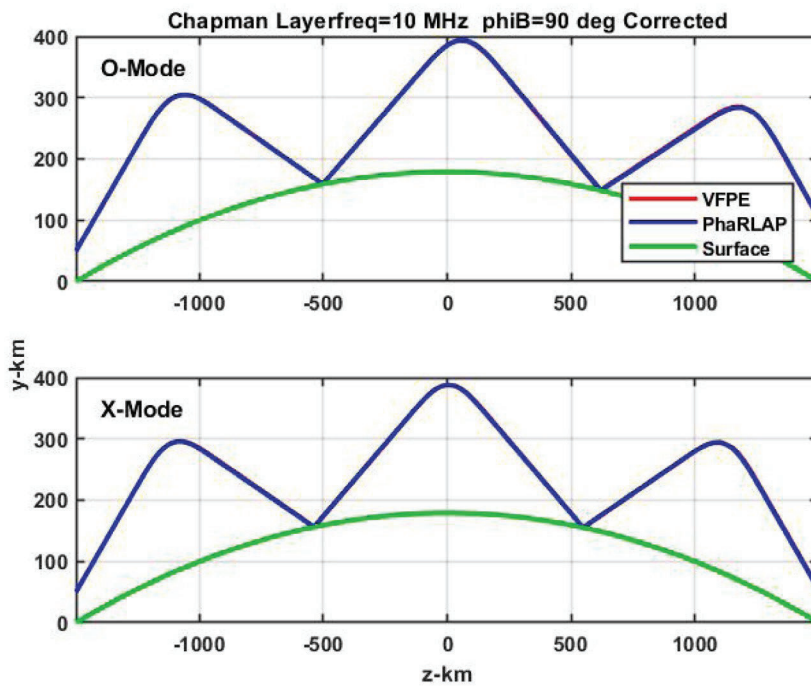


Figure 34. Recalculation of VFPE result shown in Figure 33 with VFPE correction

The results show that split-step integration of the VFPE in the HF frequency range introduces a bias. Because the bias persists in the  $B = 0$  limit, the scalar form of FPE can be used to explore possible sources of the bias. Equation (39) in (Coleman, 2008) is the  $B = 0$  limiting form of the ray equation, which is rewritten here as

$$n \frac{d^2 \mathbf{r}}{ds^2} + \frac{dn}{ds} \frac{d\mathbf{r}}{ds} = \nabla n. \quad (1.62)$$

The result is well known. Equation (3.2.1.2) in Born and Wolf (1999), which is the same ray equation, was derived directly from the scalar wave equation

$$\nabla^2 \psi(y, z) + k^2 n^2(y, z) \psi(y, z) = 0. \quad (1.63)$$

Propagation in transparent inhomogeneous media proceeds from a source to a destination. We refer to the common situation where propagation in the opposite direction is negligible as the forward approximation. Isolating forward propagation proceeds in one of two ways. The most commonly used approach starts with a formal factorization of (1.63). For example,

$$\left( \frac{d}{dz} + i(\nabla_{\perp}^2 + k^2 n^2(y, z))^{1/2} \right) \left( \frac{d}{dz} - i(\nabla_{\perp}^2 + k^2 n^2(y, z))^{1/2} \right) \psi(y, z) = 0. \quad (1.64)$$

Forward propagation is characterized by

$$\left( \frac{d}{dz} + i(\nabla_{\perp}^2 + k^2 n^2(y, z))^{1/2} \right) \psi(y, z) = 0. \quad (1.65)$$

Alternatively, the definition

$$n^2(y, z) = 1 - X(y, z) \quad (1.66)$$

can be used to identify structure-induced sources. Following the same development that was used to derive equation (24) in (Rino and Carrano, 2021a), we find that

$$\begin{aligned} \frac{d\psi(y, z)}{dz} &= \Theta \psi(y, z) + k^2 \int [H_0^{(1)}(k |y - y'|) / (4i)] X(y', z) \psi(y', z) dy' \\ &\approx \Theta \psi(y, z) + i \frac{k}{2} X(y, z) \psi(y, z) \end{aligned} \quad (1.67)$$

The structure interaction approximation above, which extracts the  $y=y'$  contribution from the integral, is at least partly responsible for the discrepancy between VFPE and ray-tracing that we have observed. Consider, for example, a plane wave (with uniform phase) that interacts with a

sinusoidally varying medium such that  $\psi(y)=1$ ,  $X(y)=A \sin(\kappa y)$  with  $|A| \ll 1$ . The restriction on  $A$  limits this analysis to very weak perturbations such that the propagation very nearly follows straight lines. In that case,

$$\int \left[ H_0^{(1)}(k|y-y'|) / (4i) \right] X(y',z) \psi(y',z) dy' = i \frac{k}{2} A \sin(\kappa y) \left\{ \frac{1}{\sqrt{1-(\kappa/k)^2}} \right\} \quad (1.68)$$

This is precisely the approximate result  $i(k/2)X(y,z)\psi(y,z)$  times the correction factor that appears in curly braces above. The correction factor converges to unity in the high-frequency limit, in which case the second line of (1.67) becomes exact. Apparently, the same is true if the wavenumber of the sinusoid ( $\kappa$ ) becomes very small. In short, *the correction factor is significant only when the spatial scale of the sinusoid becomes comparable to the wavelength*. Figure 35 shows the relative error as a function of the ratio  $\kappa/k$ .

Since the structure interaction approximation (1.67) is justifiable for any harmonic with  $\kappa > k$  (within the confines of our rather restrictive assumptions), we can construct more complicated media via linear superposition, provided we exclude structure with scale sizes close to the transmit wavelength. While admittedly crude, this analysis provides a rough handle on the error we can expect to incur from this approximation.

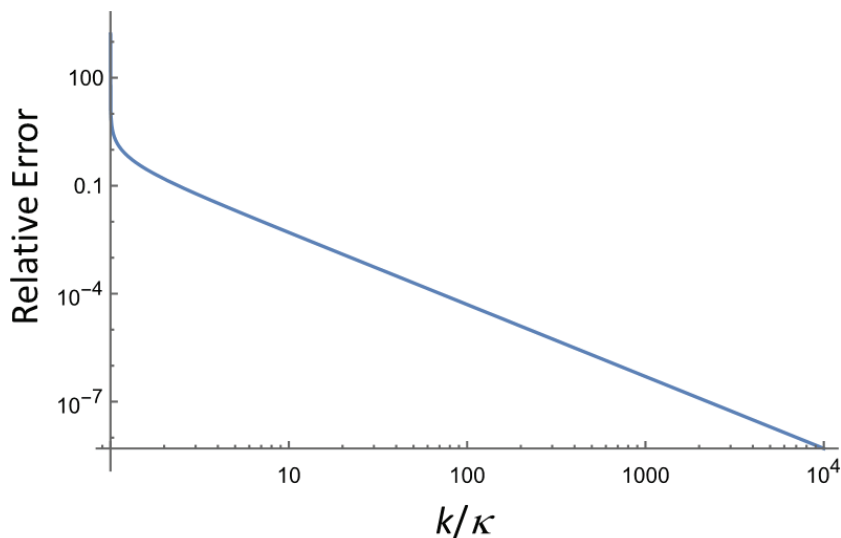


Figure 35. Relative error in the structure interaction approximation as a function of  $\kappa/k$

To put these results in perspective, at 10 MHz the signal wavelength is about 30m. The scale height of a typical Chapman ionosphere is about 60 km, or roughly 2000 wavelengths. The relative error in this case is about  $1 \times 10^{-7}$ , which is quite small. However, a typical 1500 km propagation path is roughly 50,000 wavelengths long, so may well be possible for this small error to accumulate and produce a measurable deflection in the path when the wave travels long distances.

In summary, the FPE equation method (and also the standard PWE method), marches the field forward via separate media-interaction and propagation contributions. This invites split-step integration, which applies the media-interaction and propagation terms sequentially. The cost of this separation is a decrease in accuracy when variations in the medium approach the wavelength scale. By way of comparison, the ray equation (1.62) mixes the effects of refractive index variation and redirection of evolving rays. It is well known that ray theory also breaks down when variations in the structure approach the wavelength scale, but for different reasons. Apparently, the FPE begins to degrade in accuracy sooner (i.e. when structure variations are larger) than the ray-theory because the media-interaction and propagation terms are treated separately.

#### 4.4 Locally Homogeneous Wavefield Extrapolation

In the previous section, we investigated possible reasons for the discrepancy we have noted between the VFPE and ray-theory. We proposed an empirical correction that can improve the agreement under certain circumstances. In this section we present an alternative approach that appears to correct the problem, at least for the propagation scenarios that we considered.

Two papers were presented at the URSI General assembly in a session organized by the sponsor of this project. Our second paper (Rino and Carrano, 2021b), just recently published, attracted the attention of Prof. Lewis Fishman, a mathematician who has worked extensively with the Helmholtz equation and propagation in transparent media. A fruitful collaboration has begun, in which Prof Fishman has carefully reviewed our analysis while we have shared numerical solutions of our problems of interest using his proposed forward propagation algorithms for solving the Helmholtz equation.

Recall that the scalar forward propagation equation (FPE) is given by

$$\frac{\partial}{\partial z} \psi^+(\mathbf{\eta}, z) = \Theta \psi^+(\mathbf{\eta}, z) + i \frac{k}{2} X(\mathbf{\eta}, z) \psi^+(\mathbf{\eta}, z) \quad (1.69)$$

where the free-space propagation operation  $\Theta \psi^+(\mathbf{\eta}, z)$  advances the forward-propagating field along the reference direction ( $z$ ):

$$\psi^+(\mathbf{\eta}, z + \Delta z) = \iint \hat{\psi}^+(\mathbf{\kappa}, z) \exp[ikg(\kappa)\Delta z] \exp[i\mathbf{\kappa} \cdot \mathbf{\eta}] \frac{d\mathbf{\kappa}}{(2\pi)^2}. \quad (1.70)$$

The FPE was derived from the Helmholtz equation by treating the interaction of the wave with the medium as an induced source. Fishman et al. (1984) proposed an alternative forward propagation equation based on a field-splitting approach:

$$\frac{\partial}{\partial z} \psi^+(\mathbf{\eta}, z) - i \left[ \nabla_{\perp}^2 + k^2 n^2(\mathbf{\eta}) \right]^{1/2} \psi^+(\mathbf{\eta}, z) = 0, \quad (1.71)$$

where  $n^2=1-X$  is the refractive index. Equation (1.71) is apparently exact for the case of a range-independent medium. Fishman et al. explain in their papers (1984; 1987) that the square root in the second term does not define the propagation operator. Taylor and operator series expansions of this so-called “square root operator” are both non-uniform and singular. Fishman et al. (1984; 1987) spend a great deal of effort developing various approximations for the square-root operator and investigating the implications.

In particular, Fishman (1987) evaluates the asymptotic symbol limits for the case of arbitrary angle, weak inhomogeneity, and arbitrary frequency (gradient), along with the subsequent limit of high frequency. In both of these parameter regimes, the lead term is the symbol for the free space (homogeneous medium) propagator. Fishman (1987) proposes the following high-frequency approximate marching algorithm for a locally homogeneous medium where the refractive index variation is independent of range:

$$\psi^+(\boldsymbol{\eta}, z + \Delta z) \approx \iint \hat{\psi}^+(\boldsymbol{\kappa}, z) \exp[i(k\sqrt{n(\boldsymbol{\eta})^2 - (\boldsymbol{\kappa}/k)^2} \Delta z + \boldsymbol{\kappa} \cdot \boldsymbol{\eta})] \frac{d\boldsymbol{\kappa}}{(2\pi)^2} \quad (1.72)$$

Note that if the refractive index were actually constant, the solution to (1.71) would be simply

$$\psi^+(\boldsymbol{\eta}, z + \Delta z) = \iint \hat{\psi}^+(\boldsymbol{\kappa}, z) \exp[i(k\sqrt{n^2 - (\boldsymbol{\kappa}/k)^2} \Delta z + \boldsymbol{\kappa} \cdot \boldsymbol{\eta})] \frac{d\boldsymbol{\kappa}}{(2\pi)^2}. \quad (1.73)$$

In this sense, Fishman’s high-frequency asymptotic marching algorithm may be viewed as an extrapolation of the above from a homogeneous (constant) medium to a locally homogeneous medium. For this reason, (1.72) is often referred to locally homogeneous wavefield extrapolation (LHWE). Our description here is solely intended to help interpret how the method works from a physical point of view—it is not a derivation. For a rigorous derivation of the LHWE technique, see (Fishman, 1987).

In our problems of interest, the medium is not range-independent but changes sufficiently slowly in the marching direction relative to the wavelength that (1.72) is still able to accurately advance the field, as we show using numerical examples. Note that (1.72) advances the field while simultaneously interacting with the refractive index structure. There are no separate media interaction and free-space propagation operations, as there are in split-step solutions to equations (1.69) and (1.70). We have long suspected that our use of the free-space propagator to advance the field provides an inadequate approximation at HF wavelengths, resulting in the discrepancy we have noted with geometric optics (ray-tracing).

We note that the discrete approximation of (1.72) using the trapezoid rule for quadrature requires one FFT and one large matrix multiplication to be carried out for each marching step. This is significantly more computationally expensive than the split-step solution of our FPE which requires two FFTs per marching step. However, we can accelerate the matrix multiplication calculation in several ways. Firstly, we can filter the field to reduce its bandwidth as suggested by Fishman et al. (1987), and secondly, we can implement this more-costly scheme to advance the field only where it is evolving rapidly, using the cheaper split-step algorithm to advance the field in other regions. The important point is that the off-diagonal, directional, terms in (1.72) make an important contribution to the field at HF, and we will show how their inclusion can resolve the

discrepancy between the VFPE and geometric optics. First, however, we show the results of a numerical experiment performed using Fishman’s algorithm applied to a simple model problem in order to test that our implementation is correct.

The model problem considered is a beam propagating past a dielectric cylinder with uniform material properties. Figure 36 compares solutions to this problem using the standard split-step solution to our FPE and Fishman’s algorithm. The left plots show the standard split-step solution to the FPE. The middle plots show the solution using Fishman’s forward propagation algorithm. The right plots show cross-sections from both solutions at a fixed propagation distance along the range direction. The top and bottom rows show results for values of  $\Delta X = -0.05$  and  $\Delta X = -0.15$ , respectively. The solutions appear to be quite similar, at least visually. For a more quantitative comparison we also show the intensity along a transverse cross-section at a fixed propagation distance. We find that when the dielectric cylinder represents a small absolute perturbation ( $X = -0.05$ ) of the background medium, the two solutions are indistinguishable, which suggests that our numerical implementation is correct. When the absolute perturbation is larger ( $X = -0.15$ ), however, differences between the two solutions become apparent. We believe that in this regime some of the approximations used to derive the FPE begin to break down. While an exact solution to this model problem does exist, and could be used to determine which numerical solution is the more accurate, it is cumbersome to compute. Therefore, we will return to our problem of interest (reflection of a beam of HF frequency from the ionosphere) before making additional comparisons of the algorithms.

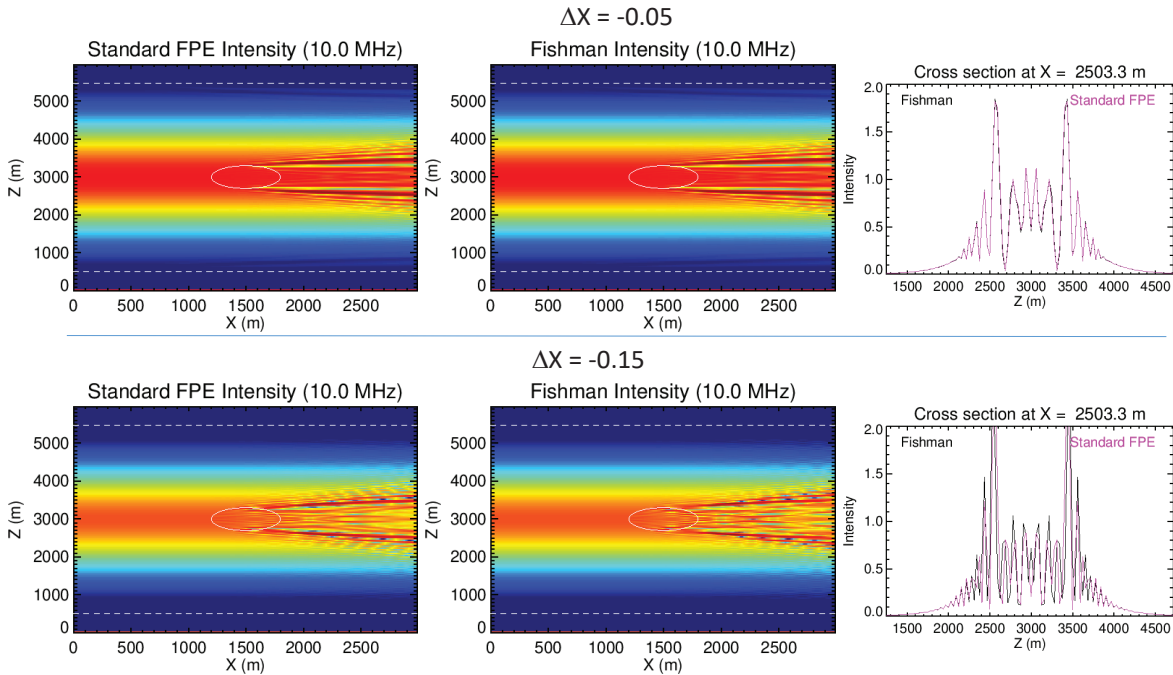


Figure 36. Plasma frequency for a Chapman ionosphere (peak = 9 MHz) and geometric optics (ray-trace) solution for an HF beam (15 MHz) reflecting from the ionosphere

We return to the problem of a beam reflecting from the ionosphere. Figure 37 shows a color-plot of plasma frequency in the ionosphere, which we have taken to be a Chapman profile with a peak of 9 MHz. When we launch a narrow beam of HF power (15 MHz in this example) upwards toward the ionosphere, it is refracted back downward to the ground. The white lines in Figure 37 show the

geometric optics solution for a small fan of rays (three separate rays) within the beam which follow the path of the signal to the location where it would intersect a curved Earth surface. While we normally use a curved earth surface to represent the lower boundary in our propagation simulations, we use a flat boundary in this example for the sake of simplicity. We use an absorbing layer at the upper boundary to implement the outbound radiation condition.

Figure 38 shows the intensity of the field obtained via standard split-step numerical solution of our FPE. Notice how the beam ‘overshoots’ the correct reflection point and returns to earth farther downrange from the transmitter than it should. This is the discrepancy with geometric optics we have been trying to resolve. This simulation used 24000 points along the x-direction (6 samples per wavelength) and  $2^{16} = 65536$  points along the z-direction (0.44 samples per wavelength).

Next, we repeated the FPE numerical solution but using much cruder sampling in range (500 points along the x-direction). These results are shown in Figure 39. Low resolution was used in this case to facilitate a fair comparison with Fishman’s algorithm which is more expensive to compute. When taking fewer range steps, the beam is less well-resolved but still clearly ‘overshoots’ the geometric optics solution, as before.

Figure 40 shows the solution using the marching algorithm proposed in Fishman et al. (1987), specifically his equations (16)-(17) with the high-frequency approximation of the operator symbol (his equation 25). Notice how the beam is now well-centered on the geometric optics solution (the discrepancy is gone). Apparently, the accurate solution for this model problem requires the inclusion of off-diagonal terms in (1.72) which Fishman et al. (1987) suggested may be interpreted as local reflection operators. This calculation required 15 hours to perform using the same sampling as the split-step FPE result shown in Figure 38 which required just a few minutes to compute (thanks to the efficiency of FFT). To produce these results, we followed a very simple procedure to speed up the calculation; we invoked Fishman’s algorithm wherever the  $\Delta X$  was nonzero, and solved the FPE elsewhere. It is possible to improve the efficiency of the algorithm by filtering the field in the Fourier domain, parallelizing the time-consuming matrix multiplication, and restricting the application of Fishman algorithm to regions with large refractive index gradients.

The upshot of this analysis is that we believe we have finally resolved the discrepancy between the FPE and geometric optics. Apparently, the discrepancy was caused by making approximations during the induced source derivation of the FPE that are not valid in the HF regime except when the perturbation  $|\Delta X|$  is very small. Fishman’s algorithm provides more accurate results when the perturbation is representative of propagation problems of practical interest at HF wavelengths. A combination of the two algorithms should provide a viable means of solving these problems. We should note that LHWE does not strictly conserve energy, however (Fishman, 1987). We observed a power enhancement at the turning point that we believe to be, at least partly, spurious (not shown).

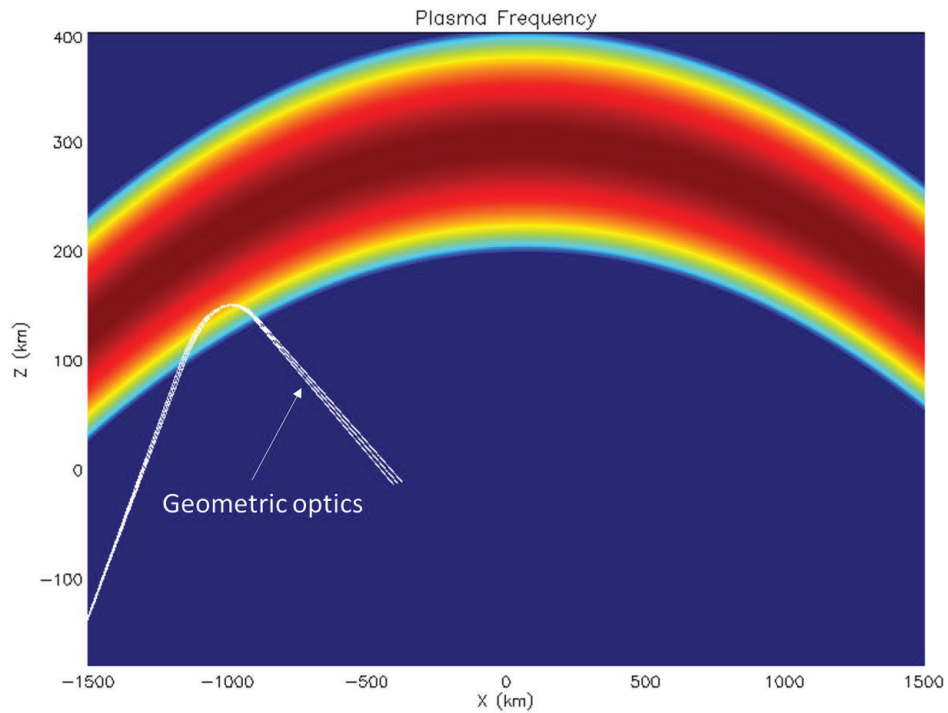


Figure 37. Plasma frequency for a Chapman ionosphere (peak = 9 MHz) and geometric optics (ray-trace) solution for an HF beam (15 MHz) reflecting from the ionosphere

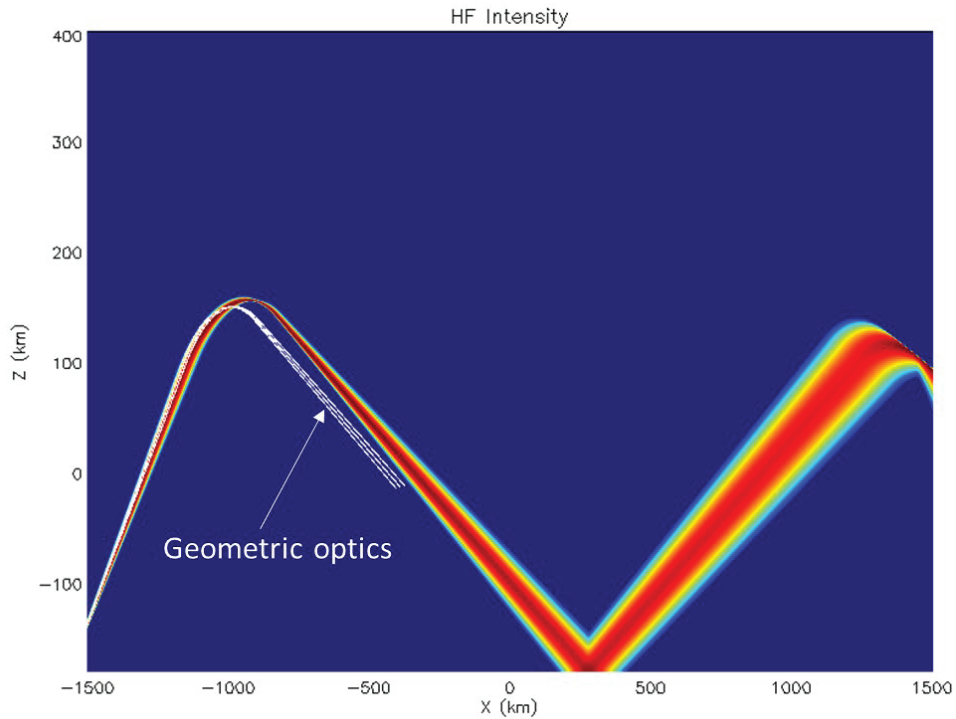


Figure 38. Adequately sampled FPE solution (colors) and geometric optics (white)

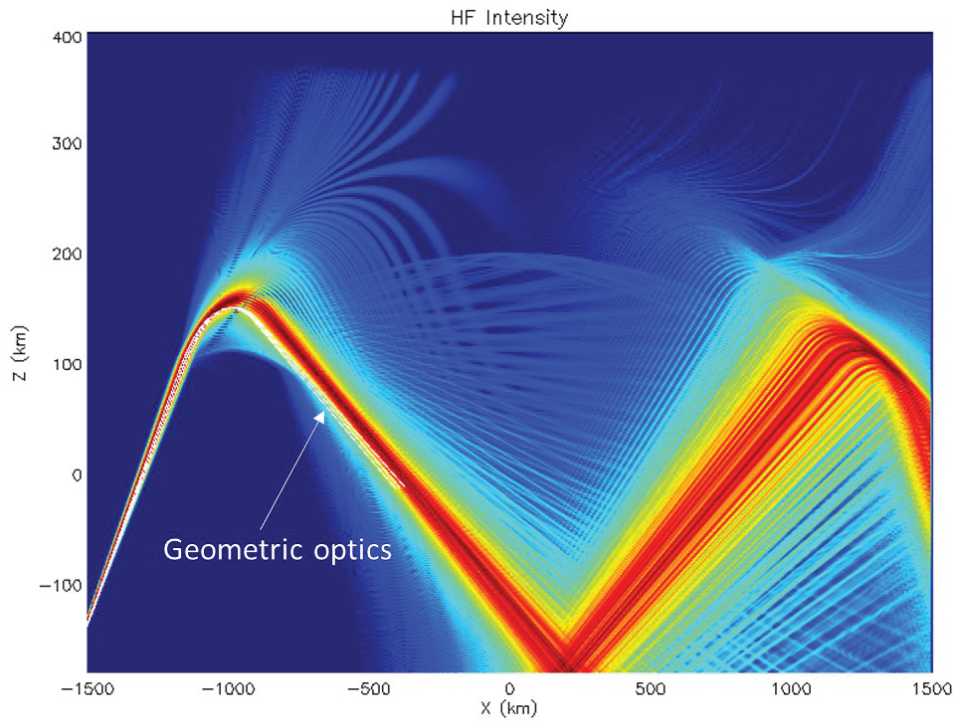


Figure 39. Coarsely sampled FPE solution (colors) and geometric optics (white)

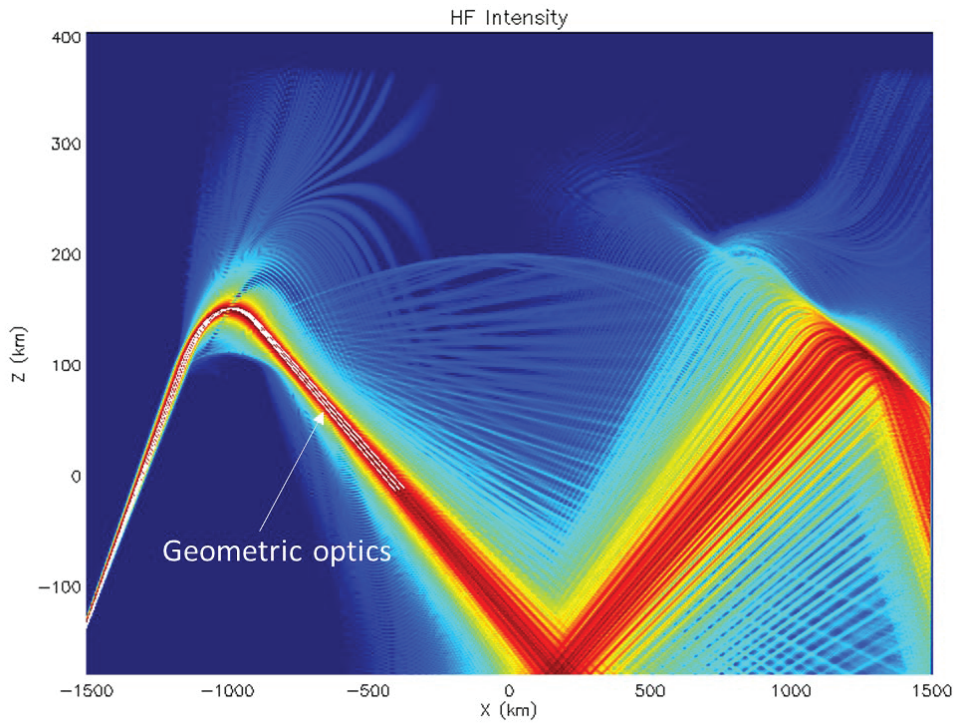


Figure 40. Coarsely sampled solution using Fishman's algorithm and geometric optics (white)

## 4.5 Corrected FPE vs Locally Homogeneous Wavefield Extrapolation

Throughout this project we have noted that small but systematic errors can accumulate when advancing the wavefield using the VFPE at HF wavelengths. Moreover, it is relatively easy to inadvertently ‘compensate’ for these small errors by making additional errors (e.g. altering boundary conditions to make AoA maps consistent with ray-tracing, or altering the effective speed of waves in the medium to increase refraction effects).

In this section, we purposely chose a geophysical environment for which even very small propagation errors would be clearly accentuated. We compare the accuracy of uncorrected FPE, corrected FPE, and LHWE methods with an independent ray-trace solution. For our test problem, we chose to transmit a 12 MHz signal at  $32^\circ$  elevation through a Chapman ionosphere with peak electron density  $NmF2=10^{12} \text{ m}^{-3}$ , peak height  $hmF2=250 \text{ km}$ , and scale height  $Hs=50 \text{ km}$  without magnetic field effects. We assumed a flat earth and applied perfectly conducting boundary conditions. To insure the discretely sampled numerical solution had converged in each case, we doubled the resolution in both altitude and range and repeated the simulation several times until the result no longer changed. We restrict our attention in this section to scalar problems, since if that cannot be not solved correctly then neither can the vector problem.

The numerical solution of this model problem using uncorrected FPE required 3 minutes of computation time. The results are shown in Figure 41. An independent ray-trace is shown in white, for reference. We found that the uncorrected FPE result does not converge to the true result (ray-trace) in the limit of infinitely fine spatial sampling  $\Delta x \rightarrow 0, \Delta z \rightarrow 0$ . Instead, the FPE predictions remain under-refracted in comparison with ray-trace result, and the errors accumulate to unacceptable levels as the wave progresses downrange. For the sake of completeness, we repeated this simulation using the standard parabolic equation (PWE) and found the errors to be considerably larger (not shown). Hence uncorrected FPE is an improvement over the standard PWE, but the errors remain unacceptably large for this problem.

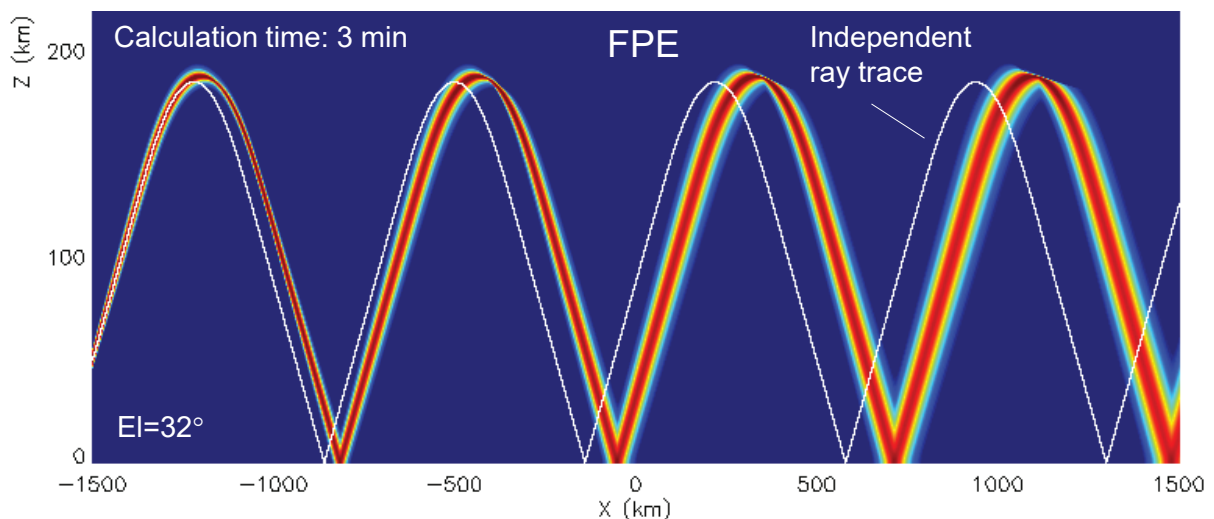


Figure 41. Propagation of a narrow beam at 12 MHz predicted by the uncorrected FPE method

In Rino and Carrano (2021b) we proposed an empirical correction for the FPE that is intended to adjust the phase speed of waves in the medium. The correction is achieved by replacing  $X$  in the FPE with  $X + X^2/2$ . The numerical solution to our model problem using corrected FPE is shown in Figure 42. Note that the FPE result is now in very good agreement with the ray-trace. The computation time is unchanged by the correction.

Empirical correction works very well for propagation in a Chapman ionosphere, and effectively preserves the computational efficiency of split-step Fourier methods. Hence, it does provide a viable solution to our problem. However, careful scrutiny of the result reveals a small error in the reflection height, and a slight shift in footprint locations from their true locations. More importantly, we have noted significant inaccuracies with this approach when solving problems involving stronger refraction. It is entirely possible that this simple correction may not be helpful for solving propagation problems in generally inhomogeneous media. In any case, theoretical justification of the correction is tenuous at best, so it should be used only with careful discretion.

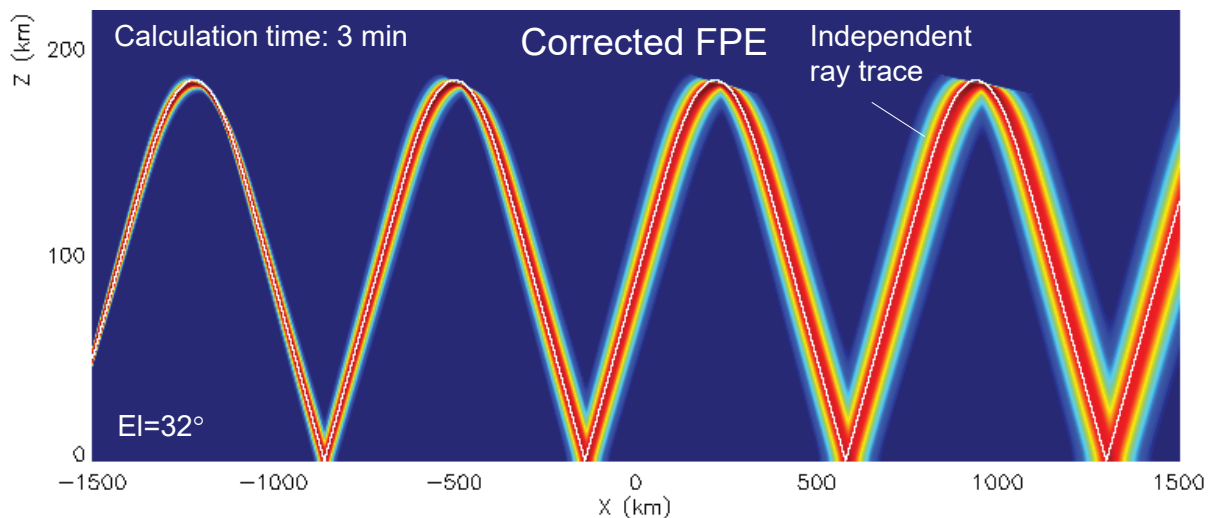


Figure 42. Propagation of a narrow beam at 12 MHz predicted by the corrected FPE method

Finally, we solve the model problem using locally homogeneous wavefield extrapolation (LHWE). The results are in excellent agreement with the ray-trace result. The numerical calculation required 108 hours, however, which is a significant increase compared to the other methods. A substantial reduction in computation time can be achieved by filtering high-frequency components of the solution, but this can result in spurious artifacts and a reduction in dynamic range. No spectral filtering was used to produce the result shown in Figure 43.

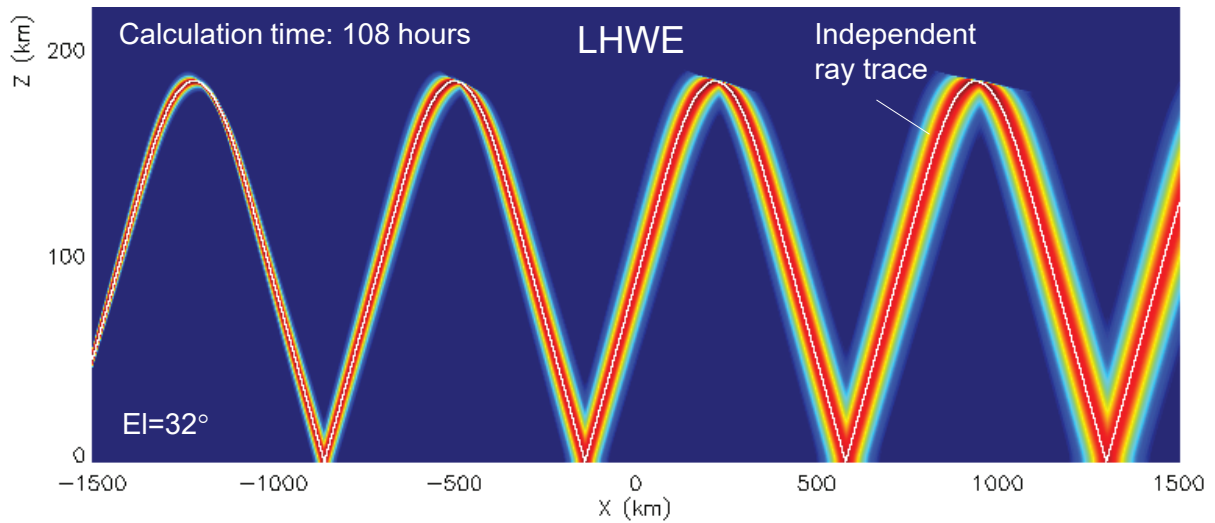


Figure 43. Propagation of a narrow beam at 12 MHz predicted by the locally homogeneous wavefield extrapolation method

At the 2022 Beacon Satellite Symposium in August, we also presented a numerical solution for this model problem using the so-called Split-Step Padé (SSP) method by Collins (1993). We found that this method produced results as accurate as LHWE method while requiring only 1.3 hours of computation time. Hence, the method is nearly as efficient as the FPE while providing better accuracy, and without the need for empirical correction factors. For additional details, we refer the interested reader to our Beacon Satellite Symposium presentation.

## 5.0 CONCLUSIONS

Over the past decade the forward propagation equation (FPE) has been used to characterize the propagation of electromagnetic (EM) waves in randomly irregular media. Following published papers that extended the scalar FPE to lower frequencies, we developed a vector FPE that accommodated polarization effects. The ionospheric constitutive relation for HF propagation is a  $3 \times 3$  tensor. An eigenvector decomposition was applied to transform the vector FPE equation into 3 independent scalar equations, which were integrated separately. The updated transformed components were then transformed back to the defining vector field components. The results, which were published in (Rino and Carrano, 2021a), seemed to capture all the expected HF characteristics. For example, with no prior identification of characteristic modes the constructed vector fields produced oppositely polarized fields, which exhibited Faraday rotation. Results published in (Rino and Carrano, 2021b) extended the development to accommodate more realistic (dielectric) boundary surfaces.

A disparity was observed between the trajectory of the FPE beam peak intensity and the calculated path of a ray launched in the direction of the initiating beam field. There was also a discrepancy in the predicted Faraday rotation rate. These disparities appeared to be a progressive bias, which suggested an underestimate of the effective perturbation strength. We found that adding a quadratic correction to the linear media interaction term brought the FPE results into agreement with the ray trace for the case of a Chapman ionosphere, as shown in (Rino and Carrano, 2021b), figure 8. Further exploration showed that the quadratic correction did not work in all cases, however. It ultimately became clear that FPE split-step integration cannot be extended to the HF frequency range with accepting a considerable error when the perturbation is large.

This led to an exploration of alternative procedures, particularly parabolic wave differential equation (PDE) methods, which have been used successfully for acoustic propagation in the ocean and seismic propagation below the earth's surface. In its simplest form, the standard parabolic wave equation is intrinsically restricted to a narrow range of propagation angles. When Fourier domain split-step integration is used, the propagation operator is implemented in a form that restricts the range of supported propagation angles. The FPE uses an exact free-space propagator, which extends the range of propagation angles in a way that does not immediately suggest the departure from ray-trace results.

This discovery was frustrating because a Chapman layer bounded by a reflecting spherical earth is an exceptionally benign environment for geometrical optics, with or without the effects of the earth's magnetic field. Whereas the exact propagation of a focused beam in a homogeneous environment is easily achieved, correctly accommodating a small refractive index gradient is theoretically and computationally demanding. Progress is being made, but we cannot be certain whether an entirely satisfactory solution has emerged. The LHWE method appears to be very accurate, but it does not strictly conserve energy. It is orders of magnitude slower than the VFPE in terms of computation time. None of the methods we explored as potential alternatives to the VFPE have been systematically tested for generally inhomogeneous birefringent ionospheric media at HF wavelengths. We proceed from this point by reviewing the limitations of the FPE method with a more detailed comparison between beam propagation and ray optics. Our hope is

that through the study of the relationship between these two we might discover a viable way to correct the FPE results while maintaining energy conservation and fast execution time.

The FPE is usually written as a first-order differential equation. The following two-dimensional form of the scalar FPE is sufficient for illustration:

$$\frac{d\psi(x,y)}{dx} = \Theta_{\Delta x}\psi(x,y) + i\frac{k}{2}X(x,y)\psi(x,y), \quad (1.74)$$

where  $\psi(x,y)$  is the scalar wavefield and  $X(x,y)$  is a constitutive parameter that defines the interaction of  $\psi(x,y)$  with the structured propagation medium. The refractive index is defined as

$$n(x,y) = \sqrt{1 - X(x,y)}. \quad (1.75)$$

For the ionosphere  $X(x,y) = (\omega_p/\omega)^2$ , where  $\omega_p$  is the plasma frequency in radians ( $\omega = 2\pi f$ ), which lies in the HF frequency range ( $1 < f < 30$  MHz) The term  $\Theta_{\Delta x}\psi(x,y)$  denotes the free-space propagation operator:

$$\Theta_{\Delta x}\psi(x,y) = \int \hat{\psi}(\kappa,y) \exp\{\pm ik_x(\kappa)\Delta x\} \exp\{i\kappa y\} \frac{d\kappa}{2\pi}, \quad (1.76)$$

where  $k = 2\pi f/c$ ,

$$k_x(\kappa) = (k^2 - \kappa^2)^{1/2}, \quad (1.77)$$

and

$$\hat{\psi}(\kappa,y) = \int \psi(x,y) \exp\{-i\kappa y\} dy. \quad (1.78)$$

is the spatial (transverse) Fourier decomposition of  $\psi(x,y)$ .

It is important to note that the  $\Delta x$  propagation steps must be small enough to resolve  $2\pi$  phase changes over the critical  $\kappa$  range ( $|\kappa| < k$ ). Moreover, attempts to integrate the FPE with additive phase-quadrature increments do not conserve total intensity. Alternative integration procedures must be used to generate numerically stable results. The split-step form

$$\psi(x + \Delta x, y) = \theta_{\Delta x}\psi(x,y) \exp\{i\frac{k}{2}X(x,y)\Delta x\}, \quad (1.79)$$

which conserves total intensity, was used for all of our results except those generated via locally homogeneous wavefield extrapolation. For FPE and narrow-angle PDE applications (such as the standard parabolic wave equation method), a region of non-zero  $X(x,y)$  is defined within a larger propagation space. An initiating field is defined at  $x = 0$ . The field is propagated incrementally. The structure within each slab is applied as a phase perturbation. This multiple-phase-screen procedure has been and continues to be a guiding principle for characterizing propagation in

structured ionospheric media. The low-frequency limitation is explicit in the narrow-angle PDE methods.

### *Propagation in Inhomogeneous Media at Low Frequencies*

The defining two-dimensional scalar wave equation

$$\nabla^2\psi(x, y) + k^2 n^2\psi(x, y) = 0 \quad (1.80)$$

can be written with the structure term on the right-hand side,

$$\nabla^2\psi(x, y) + k^2\psi(x, y) = k^2 X(x, y)\psi(x, y), \quad (1.81)$$

where equation (1.75) has been used. This equation can be expressed as an integrodifferential equation

$$\psi(x, y) = \Theta_x\psi(x, y) + k^2 \iint X(x', y')\psi(x', y')H_0^{(1)}[k\sqrt{(x-x')^2 + (y-y')^2}] / (4i)dx'dy', \quad (1.82)$$

where  $H_0^{(1)}$  is the zero order Hankel function of the first kind. The integral equation (1.82) shows explicitly that every structure element in the propagation space is an induced source that potentially interacts with every other structure element, including a usually dominant singular contribution from the element at the field location.

A complete solution must accommodate fields propagating in the forward and backward direction with respect to the  $x$  axis as a reference. The problem is simplified significantly if propagation directed back toward the source is neglected. The forward approximation is implemented by limiting the  $x'$  integration to  $0 \leq x' < \infty$ .

### *Integral Equation Methods*

Under the forward approximation the field beyond  $x$  is completely defined by the field at  $x$  and the structure beyond  $x$ . This implies that a *forward marching* FPE-type solution can be constructed. The FPE itself can be extracted from the incremental form of (1.82) by taking the  $X(x', y')\psi(x', y')$  term outside the integration over  $x'$ . The remaining singular integral is  $-2i/k$ . A variant of this procedure was used to derive the FPE in (Rino and Carrano, 2021a) and (Rino and Carrano, 2021b). In effect, only the singular contribution is retained. In and (Rino and Carrano, 2021b) the surface reflection was calculated by converting the boundary integral equations to a discrete system of triangular (forward) Ricatti equations that can be solved directly.

The possibility of using the same procedure over a continuous region was explored. It was found that, unlike the surface-scatter implementation, no discrete sampling could be constructed for stable recursive evaluation. Theoretical formulations lead to the same conclusion. Geometrical

optics, as reviewed in the next section, provides some insight into why obtaining a tractable theoretical solution has been so difficult.

### *Operator Methods and Geometric Optics*

The development starts with the operator form of (1.80), which is interpreted as a functional relation involving formal operators defined by the *operator symbols*  $\mathbf{x}$  and  $i\nabla$

$$D(\mathbf{x}, i\nabla) \Leftrightarrow [\nabla^2 + k^2 n(x)]. \quad (1.83)$$

The identification of the operator symbols anticipates the continuously varying position and direction of a beam interacting with a smoothly varying medium. Solutions can be constructed by minimizing the field operation

$$\Lambda(\psi, \psi^*) = \int \psi^*(\mathbf{x}) D(\mathbf{x}, i\nabla) \psi(\mathbf{x}) d^2 \mathbf{x}. \quad (1.84)$$

The minimization solution follows from the fact that if  $\Lambda(\psi, \psi^*)$  is evaluated for a field,  $\psi$ , which solves the wave equation, then  $\Lambda(\psi, \psi) = 0$  (Tracy et al., 2014). However, with the assumption that the field has the form

$$\psi = A \exp(i\theta), \quad (1.85)$$

a minimization procedure can be applied directly to the derivative form of the operator. The result is the eikonal equation

$$\nabla \theta^2 = n^2. \quad (1.86)$$

The eikonal equation is solved by constructing rays that satisfy the ray-equation form of the eikonal equation

$$\frac{d}{ds} \left( n \frac{dy}{ds} \right) = \nabla n, \quad (1.87)$$

where  $s$  denotes the distance along the ray and  $\tau = dy/ds$  denotes the ray direction.

Although geometrical optics does not require formal operators for its development that leads to an algorithmic solution, the connection emphasizes that agreement with geometrical optics as a necessary condition. Moreover, no problem-specific constraints should be required.

The construction of geometric optics rays requires specification only of the refractive index and its gradient. Moreover, because geometrical optics requires smoothly varying propagation media, a first-order difference gradient calculation is adequate. A ray can be initiated anywhere in the propagation space and propagated in any direction. No matter how complex the medium may be, each ray retains its integrity. A ray bundle is formally an exact geometric representation of point-source excitation from anywhere in the medium. Whereas our original use of geometrical optics

compared only the peak intensity variation of a focused beam, geometrical optics also predicts the variation of a ray bundle.

Figure 44 shows the ray heights (upper frame) and tangents (lower frame) that define a bundle of rays launched from a point on the surface represented by the green curve. The angular extent of the ray bundle is 2 degrees. To confine the computation to the FPE propagation space, rays are initiated from their intercept directions and angles in the initiation plane at  $z = -1500$  km. Following our earlier convention, the ray propagation reference is the  $z$  axis with  $y$  vertical. In the ray trace  $xyz$  system,  $x = 0$ ,  $y \leq z$ , and  $z < x$ . The rays are reflected about the surface normal at the point of interception. Ray trajectories are determined entirely by the refractive index gradients encountered. Ray sampling is determined by the ray-trace algorithm. However, because of the smooth variation of the rays, interpolation to the  $z$ -sampling for propagation calculations is readily achieved. Mirror surface reflections are implemented whenever a ray intercepts the ray boundary. The highly idealized propagation environment emphasized the critical analytic challenge, namely refractive redirection of the ray bundle.

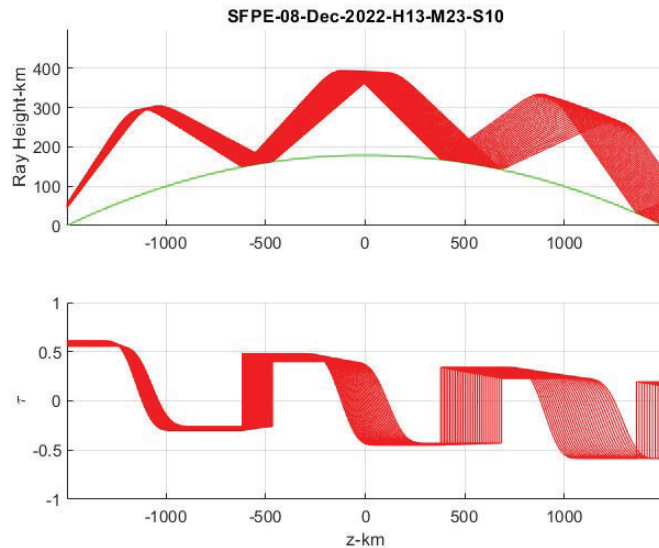


Figure 44: Upper frame shows the height of rays effectively emanating from a point outside the surface, lower frame shows the tangent of the ray angle, which is equivalent to the spatial wavenumber divided by the wavelength

Rays are defined by surfaces of constant phase, which can be recovered by mapping the optical path defined by the integral of the ray path and the refractive index. Because of the large path variation, it is convenient to display the variation of the optical path relative to the central ray defining the direction of the ray bundle. Figure 45 shows ray-bundle optical-path variations relative to the optical path variation of the central ray. The phase associated with a ray bundle is the change in the optical path across the beam. The  $y$  variation of the beam phase is very nearly linear, which suggests that eikonal surfaces are mainly steering the rays that form the ray bundle.

Now consider the problem of interest, namely propagating a focused beam into the Chapman layer. In principle the propagation calculations can be initiated with any field in the initiating plane. To match a ray bundle, the phase variation from a point source on the surface is applied in the initiation plane with a Gaussian taper about the ray intercept. The Gaussian taper defines the beam width. A phase offset is applied so that the peak intensity in the initiation plane coincides with the central ray intercept, whereby the beam intensity peak and the propagation direction determined by the spectral intensity peak are aligned with the central ray. For comparisons to geometric optics rays are launched from the beam intercept points.

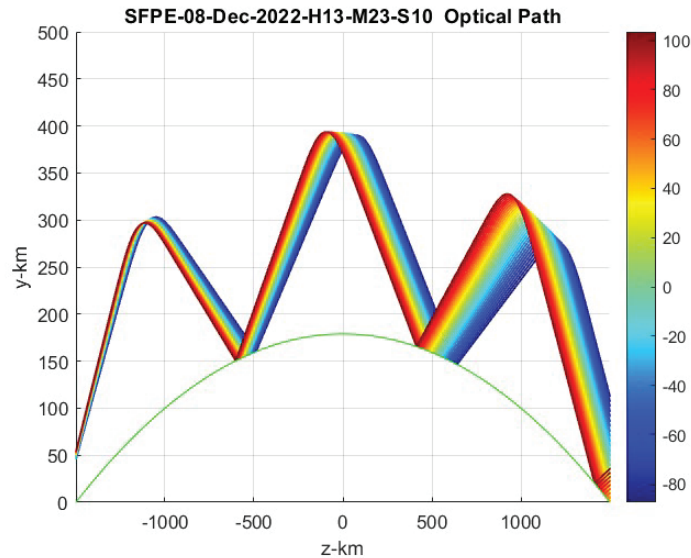


Figure 45: Optical path variation with respect to the central ray, which defines the beam direction

As suggested by the optical path variation, the beam peak intensity and the beam propagation direction can be varied incrementally by applying linear spatial wavenumber phase and linear position phase variations. Because the redirection only involves phase changes, total intensity is preserved. The upper frame of Figure 46 shows the directed-beam field intensity with the rays within the beam overlaid. The lower frame shows the spectral intensity plotted against  $\kappa/k$ . The central ray tangent that was used to steer the beam is overlaid. The only significant directed-beam and ray-bundle differences occur where the beam reversal takes place.

We know that the peak field intensity or path loss, varies inversely with the beam width. In free space the variation is proportional to the optical path distance along the central ray. However, where the beam direction is reversed the beam width is zero. The bounding upward and downward rays cross. The beam intensity variation must accommodate the singularity. However, the region that captures the singularity, appears to be small, which suggests the possibility of truncating the minimum beam width.

Figure 47 shows the result. The beam-width estimate is corrected for the propagation direction of the beam with respect to the  $y$  axis. In the same way that the direction and position of a propagating beam can be incrementally changed, the peak intensity of the beam can be modulated in such way that total intensity is preserved. Implementing the scaling requires an interpolation of the beam.

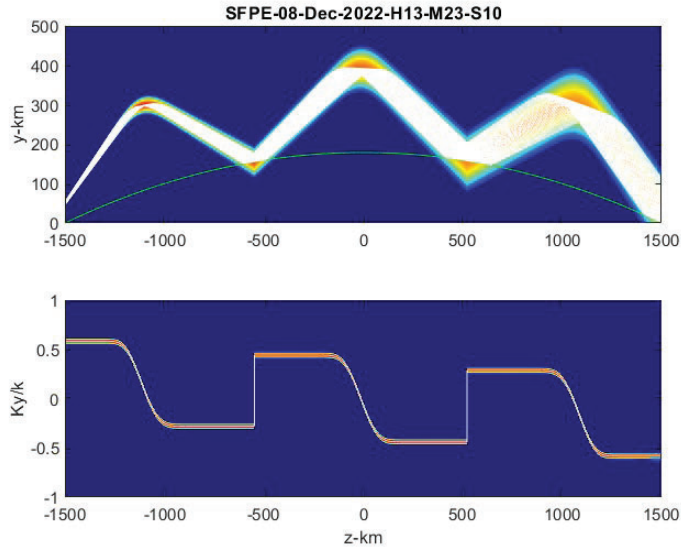


Figure 46: Upper frame shows the field intensity of a beam constrained to follow the height and direction of the central ray in the bundle

Figure 48 shows the directed-beam propagating with scaling proportional to the beam width variation from its central ray propagation expansion. Total intensity is conserved exactly. The result is certainly not exact, but it could be improved calculation of the beam path loss, which is likely to be provided by a ray-trace code such as PHaRLAP. The fact that refractive redirection of a propagating beam involves a singularity may be indicative of complexity. However, the fact that deviations from central ray steering are small imply that the most demanding computation can be confined to small segments of the propagation space.

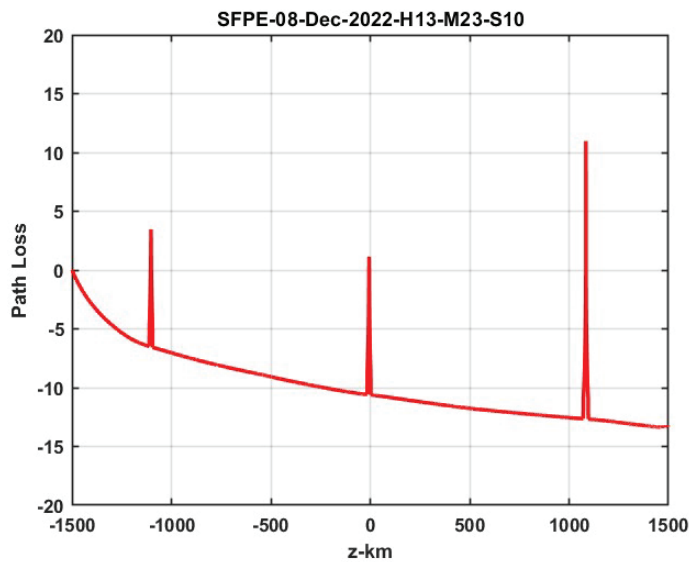


Figure 47: Path loss variation derived from geometric optics beam width estimate

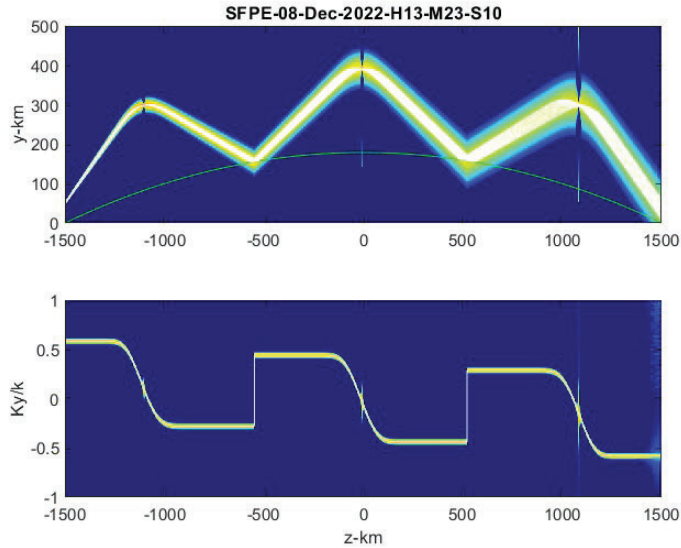


Figure 48: Scaled directed beam computation for comparison to Figure 46

### *Concluding Remarks*

High frequency (HF) sky-wave systems used for over-the-horizon-radar (OTHR), communication, and signal geolocation must contend with ionospheric structuring, which affects propagation and can adversely impact the primary mission of these sensors. Ionospheric structuring results from a variety of geophysical mechanisms that operate at low-, mid-, and high-latitudes and manifest as sporadic-E, traveling ionospheric disturbances (TIDs), mid-latitude spread-F, equatorial plasma bubbles, auroral arcs, and polar cap patches. Propagation modeling at HF wavelengths is traditionally performed via numerical ray-tracing, but the results become difficult to interpret when ionospheric structure creates highly multi-modal propagation (Carrano et al., 2020). Full-wave techniques offer the advantage of providing the electric and magnetic fields throughout the region. The improved spatial context is useful as HF waves often interact with irregularities over very long distances (hundreds or thousands of km).

While a full treatment of Maxwell's equations via finite-difference time domain (FDTD) methods should be possible, at least in principle, the computational requirements for solving large-scale HF propagation problems of practical interest remain prohibitive. Previous forward marching propagation modeling techniques, such as parabolic wave equation (PWE) methods, provide an efficient solution to large-scale problems, but have been under-utilized for ionospheric applications partly because of their inability to model the effects of an external magnetic field. The Earth's magnetic field causes significant polarization effects at HF wavelengths that must be modeled to assess the performance of modern polarization-aware HF systems. To remedy this situation, we developed a vector forward propagation equation (VFPE) method for modeling the interaction of vector waves through a structured ionosphere in the presence of an external magnetic field (Rino and Carrano, 2021a). Interaction of the waves with a perfectly conducting curved earth surface is implemented using the method of images. The ordinary (O) and extraordinary (X) propagation modes are extracted from the full-wave solution (vector electric field) post-facto.

Traces of intensity peaks in the extracted O and X mode solutions are compared with the results of rays traced with scalar and magnetoionic ray-tracing.

We applied the VFPE to model the propagation of vector waves through traveling ionospheric disturbances at mid-latitudes and developing equatorial spread F structures at low latitudes. Several manifestations of HF fading and polarization changes were observed as a consequence of the presence of ionospheric structure along the propagation path. These include terrestrial multipath fading, ionospheric multipath fading, and polarization fading which can occur in isolation or in concert. Additionally, diffraction causes scintillation of the HF signals when Fresnel-scale sized irregularities are encountered along the propagation path. Developing equatorial spread F structure causes strong multiple scatter of HF signals, resulting in the development of random filamentary regions with enhanced signal and signal fades caused by focusing and defocusing effects. We also observed that plumes of depleted plasma may act as conduits for HF power to leak into the topside ionosphere and out into space. When this occurs, less power is available to illuminate targets on the ground, thereby reducing the efficiency of the radar. None of these phenomena would be easily revealed with traditional ionospheric ray-tracing. Instead, ray-tracing results become difficult to interpret when ionospheric structure is present because the ray footprints on the ground appear to be distributed randomly. The wave-optics results show that while the propagation environment is complex for these scenarios, it often remains systematic, with multiple modes of propagation clearly defined for all ranges. We believe the additional information provided by wave-optics can be leveraged to improve OTHR performance.

One unanticipated difficulty we encountered during this research is that wave-optics modeling via split-step Fourier methods (which include the standard PWE and both the FPE and VFPE) can produce inaccurate modeling results at HF because of the very large scattering angles involved. During this project, we explored wide-angle algorithms that can provide accurate full-wave propagation results at HF, at the expense of increased computational cost. The first is a high-frequency operator symbol construction derived from phase space path integral methods (Fishman & McCoy, 1987), also referred to as locally homogenous wavefield extrapolation (LHWE). We found this method to be very accurate but also very computationally expensive. This approximation advances the field while simultaneously interacting with the refractive structure. There are no separate media interaction and free-space propagation operations with this method, as there are when solving the VFPE equation via the split-step method. We have long suspected that our use of the free-space propagator to advance the field provides an inadequate approximation at HF wavelengths, resulting in the discrepancy we have noted with geometric optics (ray-tracing).

We asked Prof. Louis Fishman, a mathematician who has dedicated several decades to study of the Helmholtz equation, to help us better understand why the LHWE method is more accurate than the FPE. His response was that the forward propagation equation resembles the arbitrary-angle, weak-inhomogeneity, arbitrary-frequency (gradient) asymptotic limit of the composition equation derived in (Fishman & McCoy, 1984). Further, taking the high-frequency limit, reveals a more general form of the FPE, where the “media-interaction” term now has an additional, multiplicative factor involving directional effects. The FPE results by arbitrarily setting the angular variable to zero, effectively treating this term as if it were a one-dimensional formulation. This is an ad hoc result, and it is not surprising that there is insufficient turning of the wavefront resulting from the suppression of the necessary angular effects in the “perturbation” term.

Just as the available funding for this project was running out, we briefly explored a wide-angle method called the split-step Padé (SSP) method (Collins, 1993). Our initial investigations suggest that this method is equally accurate as LHWE for HF problems but also relatively efficient (each run requires only a few hours on a standard PC). It can be shown that the LHWE and SSP propagators can be applied to vector problems using the diagonal decomposition approach described in section 3.4. With this extension to vector problems, it becomes possible to explore polarization effects due to ionospheric birefringence even for problems involving wide-angle scattering phenomena. Our recent experiments with beam steering suggest that the FPE informed by ray-trace diagnostics might also be an effective and efficient approach. In the future, we would like to explore the use of these algorithms to better understand how vector HF waves interact with ionospheric structure, including equatorial plasma bubbles, sporadic-E, traveling ionospheric disturbances (TIDs), and field-aligned irregularities at high-latitudes.

## 6.0 REFERENCES

- Bianchi, C. J.A. Baskaradas, M. Pezzopane, M. Pietrella, U. Sciacca, E. Zuccheretti (2013), Fading in the HF ionospheric channel and the role of irregularities, *Advances in Space Research* 52, 2013, 403–411.
- Born and Wolf (1999), *Principles of Optics: Electromagnetic Theory of Propagation, Interference, and Diffraction of Light*. Cambridge University Press. London.
- Brent, R., W. Siegmann, and M. Jacobson (1990), Anisotropic electromagnetic wave propagation modeling using parabolic approximations, *Radio Sci.*, 25, 6, 1121-1136.
- Budden, K.G. (1985), *The Propagation of Radio Waves*. Cambridge University Press, Cambridge.
- Carrano, C., J. Retterer, K. Groves, G. Crowley, T. Duly, and D. Hunton (2020), Wave-Optics Analysis of HF Propagation through Traveling Ionospheric Disturbances and Developing Plasma Bubbles, *URSI GASS 2020*, Rome, Italy, 29 August - 5 September 2020.
- Cervera, M. A., and T. J. Harris (2014), Modeling ionospheric disturbance features in quasi-vertically incident ionograms using 3-D magnetoionic ray tracing and atmospheric gravity waves, *J. Geophys. Res. Space Physics*, 119, 431–440, doi:10.1002/2013JA019247.
- Chaudhury, B. and S. Chaturvedi (2005), Three-Dimensional Computation of Reduction in Radar Cross Section Using Plasma Shielding, *IEEE Transactions on Plasma Science*, vol. 33, no. 6.
- Chew, W.C. (1990), *Waves and fields in inhomogeneous media*. A Van Nostrand Renhol.
- Coleman, C. (1998), A ray tracing formulation and its application to some problems in over-the-horizon radar, *Radio Sci.*, 33 (4), 1187-1197.

- Coleman C. (2008), Ionospheric ray-tracing equations and their solution, Radio Science Bulletin No 325 (June 2008).
- Collins, M. (1993), A split-step Padé solution for the parabolic equation method, J. Acoust. Soc. Am., Vol. 93, No. 4.
- Croft, T. and H. Hoogasian (1968), Exact ray calculations in a quasi-parabolic ionosphere with no magnetic field, Radio Sci., 3, 1.
- Davies, K. (1996), Ionospheric Radio Propagation. Dover Publications.
- Dockery, G. (1998), Development and use of electromagnetic parabolic equation propagation models for U.S. Navy applications, Johns Hopkins APL technical digest, vol. 19, no. 3.
- Dockery and Kuttler (1996), An improved impedance-boundary algorithm for Fourier split-step solutions of the parabolic wave equation, IEEE Transactions on Antennas and Propagation, vol. 1, no. 12.
- Fishman, L. and J. J. McCoy (1984), Derivation and application of extended parabolic wave theories. i. the factorized Helmholtz equation, Journal of Mathematical Physics, 25, 1984. doi.org/10.1063/1.526149.
- Fishman, L. and J. J. McCoy, and S. C. Wales (1987), Factorization and path integration of the Helmholtz equation: Numerical algorithms Acoustical Society of America Journal, 81, 1987. doi: 10.1121/1.394542.
- Hocke, K. and K. Igarashi (2003), Wave-optical simulation of the oblique HF radio field, Radio Sci., 38, 3, 1039, doi:10.1029/2002RS002691.
- Kuttler and Dockery (1991), Theoretical description of the parabolic approximation/Fourier split-step method of representing electromagnetic propagation in the troposphere, Radio Science, Volume 26, Number 2, Pages 381-393, March-April 1991.
- Levy, M. (2000), Parabolic equation methods for electromagnetic wave propagation, London: The Institution of Electrical Engineers, 2000.
- Martin, J. and S. Flatté (1998), Intensity images and statistics from numerical simulation of wave propagation in 3-D random media, Applied Optics, Vol. 27, No. 11.
- Paznukhov, V.V. (2004), Atmospheric Gravity Waves/Traveling Ionospheric Disturbances Study with Digisondes. Ph.D. Dissertation, University of Massachusetts Lowell, Lowell, MA, 2004.
- Rino and Ngo (1997), Forward propagation in a half-space with an irregular boundary, IEEE Transactions on Antennas and Propagation, vol. 45, no. 9.

- Rino, C. and V. Kruger (2001), a comparison of forward-boundary-integral and parabolic-wave-equation propagation models, *IEEE transactions on antennas and propagation*, 49, 4.
- Rino, C. L. (2011), *The theory of scintillation with applications in remote sensing*, John Wiley, New York.
- Rino, C., C. Carrano, K. Groves, and T. Yokoyama (2018), A configuration space model for intermediate-scale ionospheric structure, *Radio Sci.*, vol 53, no. 12.
- Rino, C., and C. Carrano (2021a), A vector theory for forward propagation in a structured ionosphere with surface reflections, *Journal of Atmospheric and Solar-Terrestrial Physics*, 223, (2021), doi.org/10.1016/j.jastp.2021.105740.
- Rino, C., and C. Carrano (2021b), A vector theory for forward propagation in a structured ionosphere, *Journal of Atmospheric and Solar-Terrestrial Physics*, Volume 215, 2021, doi.org/10.1016/j.jastp.2021.105558.
- Tracy, E., A. Brizard, A. Richardson, and A. Kaufman (2014), *Ray tracing and beyond*, Cambridge University Press.
- Wagen, J. and K. Yeh (1989), Simulation of HF propagation and angle of arrival in a turbulent ionosphere, *Radio Sci.*, 24, 196–208.
- Yau, K., Coleman, C., Cervera, M (2006), Investigation on fading of high frequency radio signals propagating in the ionosphere – results from a Jindalee radar experiment, 10th IET Int. Conf. on Ionospheric Radio Systems and Techniques, IRST 2006, July 2006, pp. 7–11.
- Yeh, K. and C. Liu (1972), *Theory of ionospheric waves*, Academic Press, New York.
- Yokoyama (2017), A review on the numerical simulation of equatorial plasma bubbles toward scintillation evaluation and forecasting, *Progress in Earth and Planetary Science*, vol. 4, no. 37.

## **APPENDIX A – Publications and Presentations**

- Carrano, C., C. L. Rino, and S. Mudaliar, Forward Propagation Modeling of High Frequency Waves through a Structured Ionosphere with Polarization Effects, Presentation given at the fall meeting of the American Geophysical Union, New Orleans, 13-16 December 2021.
- Carrano, C. S., C. L. Rino, and L. Fishman, Accurate and efficient full-wave modeling of HF propagation in the birefringent ionosphere, Presentation given at the 21<sup>st</sup> Beacon Satellite Symposium, Boston College, 1-5 Aug 2022.

Rino, C., and C. Carrano (2021a), A vector theory for forward propagation in a structured ionosphere with surface reflections, *Journal of Atmospheric and Solar-Terrestrial Physics*, 223, (2021), doi.org/10.1016/j.jastp.2021.105740.

Rino, C., and C. Carrano (2021b), A vector theory for forward propagation in a structured ionosphere, *Journal of Atmospheric and Solar-Terrestrial Physics*, Volume 215, 2021, doi.org/10.1016/j.jastp.2021.105558.

Rino, C. and C. Carrano, Propagation in transparent inhomogeneous media-a comparison of methods, Presentation for the IEEE AP-S/URSI 2022, Denver, July 10-15, 2022.

## LIST OF SYMBOLS, ABBREVIATIONS AND ACRONYMS

BIE	boundary integral equation
EM	electromagnetic
FDTD	finite-difference time domain
FPE	forward propagation equation
HF	high frequency
LHWE	locally homogeneous wavefield extrapolation
OTHR	over the horizon radar
PWE	parabolic wave equation
SSP	split-step Padé
TID	traveling ionospheric disturbance
VFPE	vector forward propagation equation
<b>B</b>	magnetic flux
<b>D</b>	displacement flux
<b>E</b>	electric field
<b>G</b>	free-space Green's function
<b>H</b>	magnetic field
$H_0^1$	Hankel function of the first kind of order zero
$\bar{I}$	identity matrix
$S(\mathbf{r})$	eikonal function
$X$	ratio of plasma frequency to signal frequency (squared)
$X\bar{\chi}$	susceptibility matrix
$U$	factor to account for electron collisions
$c$	speed of light in vacuum
$f$	signal frequency
$k$	free-space signal wavenumber
$n$	refractive index
$\hat{\mathbf{n}}$	unit vector in the direction of the wavefront normal
<b>p</b>	time-averaged Poynting flux
$\epsilon_0$	permittivity of free space
$\bar{\epsilon}$	dielectric tensor

$\eta_0$	impedance of free-space
$\theta_{\Delta x}$	free space propagation operator (marches the field a distance $\Delta x$ along the $x$ -axis)
$\psi$	a solution to the wave equation
$\psi_0$	a solution to the homogeneous wave equation (in free-space)
$\omega$	signal angular frequency
$\omega_p$	plasma frequency
$\Omega$	Faraday rotation angle